

VIBRATIONAL SPECTROSCOPY OF ASTROPHYSICAL SPECIES

By

YUN WANG

A DISSERTATION PRESENTED TO THE GRADUATE SCHOOL
OF THE UNIVERSITY OF FLORIDA IN PARTIAL FULFILLMENT
OF THE REQUIREMENTS FOR THE DEGREE OF
DOCTOR OF PHILOSOPHY

UNIVERSITY OF FLORIDA

2009

© 2009 Yun Wang

To my parents

ACKNOWLEDGMENTS

First and foremost, I would like to express my sincerest gratitude to my supervisor, Dr. Martin Vala, who has supported me throughout my graduate work at UF. He has been incredibly helpful, knowledgeable, and has been very patient allowing me to work in my own way. His attitudes to research and teaching have benefited me immensely. Were it not for his hard work and support I could never have accomplished what I have. I am really lucky and honored to be his last student.

I especially thank Dr. Jan Szczepanski for his selfless aid, patient instruction and helpful discussions. He not only guided me on many topics of science but also shared his joy of life with me. Many results presented in this dissertation are a consequence of efficient teamwork between Jan and me.

My thankfulness also goes to my Ph. D. committee members, Dr. John Eyler, Dr. So Hirata, Dr. David Powell and Dr. Charles Telesco. Your ambition for science and passion for research have intrigued my enthusiasm for scientific exploration.

I would like to thank my parents for supporting me throughout my life. They let me chase my dream, even when it led me further and further from home. Nonetheless, their support was endless and, as such, so is my gratitude. I also acknowledge all my friends, for their support, understanding and encouragement throughout the past years.

TABLE OF CONTENTS

	<u>page</u>
ACKNOWLEDGMENTS.....	4
LIST OF TABLES.....	8
LIST OF FIGURES	10
ABSTRACT	14
CHAPTER	
1 ASTROPHYSICAL BACKGROUND.....	16
The Interstellar Medium	16
Unidentified Interstellar Infrared Emission Bands	19
Diffuse Interstellar Absorption Bands	23
Metal Depletion in the ISM	25
2 MATRIX ISOLATION SPECTROSCOPY METHOD.....	27
Fundamentals of Matrix Isolation Spectroscopy.....	27
Experimental Method.....	28
Experimental Setup.....	28
Laser Ablation.....	31
Generation of PAHs.....	31
3 VIBRATIONAL SPECTROSCOPY OF NEUTRAL COMPLEXES OF IRON AND POLYCYCLIC AROMATIC HYDROCARBONS	32
Introduction	32
Computational and Experimental Details.....	34
Computational Details.....	34
Experimental Details	35
Fe(benzene) and Fe(benzene) ₂ complexes.....	36
Fe(naphthalene) complexes	44
Fe(flourene) complexes	48
Fe(pyrene) complexes.....	50
Fe(coronene) complexes.....	53
Effect of complexation on IR spectra	55
Summary.....	57

4	COPPER-CARBON CLUSTERS: STRUCTURE, INFRARED FREQUENCIES AND ISOTOPIC SCRAMBLING	59
	Introduction	59
	Computational and Experimental Details	60
	Experimental methods	60
	Computational methods	61
	Experimental Infrared Spectra	62
	Equilibrium geometries and vibrations for the $Cu_m C_n$ ($m = 1, 2, n = 1, 2, 3$) clusters	65
	The CuC Copper-Carbon Cluster	68
	The CuC_2 Copper-Carbon Cluster	68
	The Cu_2C Copper-Carbon Cluster	68
	The Cu_2C_2 Copper-Carbon Cluster	68
	The CuC_3 Copper-Carbon Cluster	69
	The Cu_2C_3 Copper-Carbon Cluster	72
	$^{12/13}C$ -Isotope Scrambling in the Near Linear CuC_3 Clusters	72
	Longer CuC_n ($n = 4 - 9$) clusters	76
	Summary	80
5	SILVER-CARBON CLUSTER: STRUCTURE AND INFRARED FREQUENCIES	82
	Introduction	82
	Computational and Experimental Details	83
	Experimental Methods	83
	Computational Methods	84
	Experimental Infrared Spectra	85
	Equilibrium Geometries and Vibrations for $Ag_m C_n$ ($m = 1, 2; n = 1-3$) Clusters	87
	The AgC Silver-Carbon Cluster	88
	The AgC_2 Silver-Carbon Cluster	89
	The AgC_3 Silver-Carbon Cluster	89
	The Ag_2C Silver-Carbon Cluster	92
	The Ag_2C_2 Silver-Carbon Cluster	92
	The Ag_2C_3 Silver-Carbon Cluster	92
	Summary	93
6	GOLD-CARBON CLUSTER: STRUCTURE AND INFRARED FREQUENCIES	94
	Introduction	94
	Computational and Experimental Details	95
	Experimental Methods	95
	Computational Methods	95
	Experimental Infrared Spectra	97
	Theoretical Calculations for Gold-Carbon AuC_3 Cluster	101
	Summary	106

7	CONCLUSIONS AND FUTURE WORK.....	108
	Iron and PAH Complexes	108
	Metal Carbon Clusters	108
	Future Work.....	110
	LIST OF REFERENCES	113
	BIOGRAPHICAL SKETCH	122

LIST OF TABLES

<u>Table</u>	<u>page</u>
1-1 List of identified interstellar molecules	18
1-2 Astrophysically abundant elements and their depletion factors. ⁴³	26
3-1 Computed properties for Fe(PAH) complexes.....	39
3-2 IR absorption spectra of Fe(C ₆ H ₆) and Fe(C ₆ D ₆) complexes.....	41
3-3 IR absorption spectra of Fe(C ₆ H ₆) ₂ and Fe(C ₆ D ₆) ₂ complexes.	41
3-4 Comparison of present work with previous IR band assignments for Fe(C ₆ H ₆) complex.....	42
3-5 Comparison of present work with previous band assignments for Fe(C ₆ H ₆) ₂ complex....	43
3-6 IR absorption spectra of Fe(C ₁₀ H ₈) and Fe(C ₁₀ D ₈) iron(naphthalene) complexes.	47
3-7 IR absorption spectra of Fe(C ₁₃ H ₁₀) iron(flourene) complex.....	48
3-8 IR absorption spectra of Fe(C ₁₆ H ₁₀) iron(pyrene) complex (isomer F from Figure 3- 1).....	52
3-9 IR absorption spectra of Fe(C ₂₄ H ₁₂) iron (coronene) complex.	55
4-1 Vibrational frequencies (cm ⁻¹) and integral intensities (km/mol) for electronic ground states of Cu _m C _n (m = 1, 2; n = 1, 2, 3) clusters (displayed in Figure 4-3), calculated using B3LYP and MPW1PW91 functionals.	66
4-2 Calculated total energies, E _{ZPE} (Hartrees), corrected for zero point vibrational energies, and estimated dissociation energies, D ₀ (eV) or isomerization energy barriers, E _{Iso} (eV) for Cu _m C _n (n = 1, 2; m = 1, 2, 3) isomers.	67
4-3 Experimental (Ar matrix, 12K) and calculated isotopomer frequencies (integral intensities) for the asymmetric and symmetric CC stretch fundamental modes of fully optimized equilibrium geometry of near-linear ⁶³ Cu ^{12/13} C (G , Figure 4-3). Proposed band assignments marked in Figure 4-2 are given in the first column.	71
4-4 Calculated (at MPW1PW91/6-311++G(3df)) harmonic vibrational frequencies and their integral intensities (in parentheses) for the CuC _n (n = 4 – 9) copper-carbon clusters (displayed in Fig. 4-5).	77
5-1 Vibrational Frequencies (cm ⁻¹) and Integral Intensities (km/mol) for Electronic Ground States of Ag _m C _n (m = 1, 2; n = 1, 2, 3) Clusters (displayed in Figure 5-3), Calculated Using MPW1PW91/SDD Functional/basis sets.....	89

5-2	Comparison of Experimental and Calculated Isotopomer Frequencies (Integral Intensities) for the Asymmetric C=C Stretch and Symmetric C=C Stretch Fundamental Modes of Near Linear $^{107}\text{Ag}^{12/13}\text{C}_3$	91
6-1	Vibrational frequencies (cm^{-1}) and integral intensities (km/mol) for electronic ground states of near-linear AuC_3 clusters (displayed in Figure 6-4), calculated using different functional/basis sets.....	102
6-2	Comparison of Experimental and Calculated (at BPW91/SDD and BPW91/LanL2DZ level) Isotopomer Frequencies (Integral Intensities) for the Asymmetric C=C Stretch and Symmetric C=C Stretch Fundamental Modes of Near Linear $^{197}\text{Au}^{12/13}\text{C}$	103
6-3	Comparison of Experimental and Calculated (at MPW1PW91/SDD, MPW1PW91/SDDAll and MPW1PW91/LanL2DZ level) Isotopomer Frequencies (Integral Intensities) for the Asymmetric C=C Stretch and Symmetric C=C Stretch Fundamental Modes of Near Linear $^{197}\text{Au}^{12/13}\text{C}$	104
6-4	Comparison of Experimental and Calculated (at MPW1PW91/6-311++G(3df)/SDD and MPW1PW91/6-311++G(3df)/LanL2DZ level) Isotopomer Frequencies (Integral Intensities) for the Asymmetric C=C Stretch and Symmetric C=C Stretch Fundamental Modes of Near Linear $^{197}\text{Au}^{12/13}\text{C}$	105
6-5	Comparison of Experimental and Calculated (at BPW91/6-311++G(3df)/SDD (pseudopotential) and B3LYP/6-311++G(3df)/LanL2DZ level) Isotopomer Frequencies (Integral Intensities) for the Asymmetric C=C Stretch and Symmetric C=C Stretch Fundamental Modes of Near Linear $^{197}\text{Au}^{12/13}\text{C}$	106

LIST OF FIGURES

<u>Figure</u>	<u>page</u>
1-1	The emission spectra of the post-AGB objects, IRAS 16279-4757, the Red Rectangle, and the planetary nebula, NGC 7027. ¹⁶ 19
1-2	Comparison of UIR bands with PAH model. Top: (a) emission spectrum from the proto-planetary nebula IRAS 22272+5435 compared with the (b) absorption spectrum produced from a mixture of neutral and cationic PAHs. Bottom: the (c) emission spectrum from the Orion ionization ridge compared with the (d) absorption spectrum produced from a mixture of fully ionized PAHs. ²⁰ 21
1-3	Plot of the electronic transition wavelength for even-numbered carbon cluster anions observed in an Ar matrix at 36 K versus the number of carbons in the cluster chain. ²¹ 23
1-4	The synthetic spectrum of the hot B0 II star BD+63° 1964. ³² 24
1-5	The elemental composition of the solar system. The abundance of hydrogen is arbitrarily set to 10^{12} so that the smallest abundance in the graph is about 1. ⁴² 25
2-1	Illustration of the principle of matrix isolation. The inert host matrix isolates guest particles from each other and prevents reaction. 28
2-2	Experimental setup for Fe-PAH experiments. 29
2-3	Experimental setup for copper-carbon experiments. 30
3-1	Lowest energy stable structures for the complexes of iron with benzene (C_6H_6)(A), bis-benzene (C_6H_6) ₂ (B), naphthalene ($C_{10}H_8$) (C), fluorene ($C_{13}H_{10}$) (D), pyrene ($C_{16}H_{10}$) (E), pyrene (second isomer, F), and coronene (G), all optimized at the MPW1PW91/6-31+G(d, p) level of theory. 36
3-2	IR absorption spectrum of benzene (C_6H_6) only (a), Fe codeposited with benzene (b), after matrix UV-visible photolysis (c) and after matrix annealing at 35 K (d), all in solid Ar at 12K. 37
3-3	Synthetic experimental and calculated infrared absorption spectra at indicated spin state multiplicities for the $Fe(C_6H_6)$ complex. 38
3-4	Synthetic experimental and calculated infrared absorption spectra for the $Fe(C_6H_6)_2$ complex. The inaccessible energy region overlapped with the absorption band of benzene is marked by the horizontal line (a). 40
3-5	IR absorption spectrum of: naphthalene ($C_{10}H_8$) only (a), Fe codeposited with naphthalene (b), after matrix UV-visible photolysis (c), all in solid Ar at 12K. The star marked band at 873.1 cm^{-1} is unassigned. 44

3-6	Calculated IR spectrum of Fe(C ₁₀ D ₈) (a), experimental IR absorption spectrum of naphthalene-d ₈ (C ₁₀ D ₈) only (b), experimental IR absorption spectrum of Fe codeposited with naphthalene-d ₈ (c), experimental IR absorption spectrum of Fe codeposited with naphthalene-d ₈ after matrix UV-visible photolysis (d), all in solid Ar at 12 K.	45
3-7	Synthetic experimental and calculated infrared absorption spectra with different spin multiplicities for the Fe(naphthalene) complex.....	46
3-8	Calculated IR spectrum of Fe(C ₁₃ H ₁₀) (a), experimental IR absorption spectrum of fluorene (C ₁₃ H ₁₀) only (b), experimental IR absorption spectrum of Fe codeposited with fluorene (c), experimental IR absorption spectrum of Fe codeposited with fluorene after matrix UV-visible photolysis (d), all in solid Ar at 12K.....	50
3-9	Calculated IR spectrum of Fe(C ₁₆ H ₁₀) (structure E) (a), calculated IR spectrum of Fe(C ₁₆ H ₁₀) (structure F) (b), experimental IR absorption spectrum of pyrene (C ₁₆ H ₁₀) only (c), experimental IR absorption spectrum of Fe codeposited with pyrene (d), experimental IR absorption spectrum of Fe codeposited with pyrene after matrix UV-visible photolysis (e), all in solid Ar at 12K plotted in two energy regions [a] and [b]. ...	51
3-10	Calculated IR spectrum of Fe(C ₂₄ H ₁₂) (a), experimental IR absorption spectrum of coronene (C ₂₄ H ₁₂) only (b), experimental IR absorption spectrum of Fe codeposited with coronene (c), experimental IR absorption spectrum of Fe codeposited with coronene after matrix UV-visible photolysis (d), all in solid Ar at 12K.	54
3-11	Comparison of summed IR absorption spectra calculated at the MPW1PW91/6-31+G(d,p) level for a 1:1:1:1 mixture of naphthalene, fluorene, pyrene and coronene (PAH panel), for their complexes with iron (Fe(PAH) panel), for similar mixture of cations (PAH ⁺ panel) and for their cationic complexes with iron (Fe(PAH) ⁺ panel). We note that the PAH, PAH ⁺ and Fe(PAH) ⁺ spectra are prepared at similar way to those of ref. 72, ⁷² but for comparison purpose include also spectra of coronene, coronene ⁺ and Fe(coronene) ⁺	56
4-1	Infrared absorption spectra of products of laser ablation of graphite (¹² C (99%) + ¹³ C (1%)) (spectrum a) and products of two-beam laser ablation of graphite and copper (spectrum b, enlarged twofold). The spectra were recorded after matrix annealing to 35 K then cooling back to 12 K. The major bands due to pure carbon clusters and their reaction products with copper at 1830 and 1250.5 cm ⁻¹ are indicated. Carbon monoxide and its product with copper are also marked.	63
4-2	Infrared spectra of reaction products from laser ablation of Cu and ¹² C (spectrum a) displayed in two energy regions. The bands at 1830.0 and 1250.5 cm ⁻¹ are due to a common carrier containing Cu and ¹² C. Spectrum b was collected from runs similar to spectrum a, but with a ¹³ C-enriched sample. The band carriers marked by vertical dashed lines are due to: C ₃ H (1824.4 cm ⁻¹), ^{100,101} C ₂ H ⁺ (1820.2 cm ⁻¹), ¹⁰² and C ₁₂ (1817.9 cm ⁻¹). ¹⁰³ The fractionations of b → d as well as of e → g isotopomers <i>via</i> the proposed ^{12/13} C isotopic scrambling in <i>nl</i> -Cu ^{12/13} C ₃ (see text) are marked.	64

4-3	Optimized equilibrium structures for the CuC, CuC ₂ , Cu ₂ C, Cu ₂ C ₂ , CuC ₃ , and Cu ₂ C ₃ clusters. The bond lengths (Å) and angles (°) calculated at B3LYP/6-311++G(3df) (italic type, top) and at MPW1PW91/6-311++G(3df) (normal type) are marked. The relative isomer energies are indicated.	65
4-4	Total energy plot for the near linear CuC ₃ (² A') and bicyclic CuC ₃ (² A' and ² A'/ ² A ₁) clusters calculated at the MPW1PW91/6-311++G(3df) level by incrementing the α (CCC) angle in the range of 77 ≤ α ≤ 180° and 71.6 ≤ α ≤ 93°, respectively. For each α the four remaining geometrical parameters were fully optimized. Note that the 63-12-12-13 cluster reactant (left) rearranges to the 63-13-12-12 lower energy isotopomer product by breaking the ¹² C-Cu bond in structure H , then passing over the TS and relaxing to the G product (right) in the forward reaction pathway.....	75
4-5	Optimized equilibrium structures for the CuC _n (n = 4 – 9) clusters. The bond lengths (Å) and angles (°) calculated at MPW1PW91/6-311++G(3df) are marked.	78
5-1	Infrared absorption spectra of products of laser ablation of graphite (spectrum a) and products of two-beam laser ablation of graphite and silver (spectrum b). The spectra were recorded after matrix annealing to 35K then cooling back to 12 K. The major bands due to pure carbon clusters and their reaction products with silver at 1827.8 and 1231.6 cm ⁻¹ are indicated.....	86
5-2	Infrared spectra of reaction products from laser ablation of Ag and ¹² C (spectrum a) and from laser ablation of Ag and ^{12/13} C (spectrum b). The bands marked by vertical dashed lines are tentatively assigned to isotopomeric partners of the 1231.6 cm ⁻¹ band. The bands marked by vertical dotted lines are due to: C ₃ H (1824.4 cm ⁻¹), ^{100,101} C ₂ H ⁺ (1820.2 cm ⁻¹), ¹⁰² C ₁₂ (1817.9 cm ⁻¹), ¹⁰³ and C ₆ (1197.2 cm ⁻¹). ¹³⁴	87
5-3	Equilibrium structures for the AgC, AgC ₂ , AgC ₃ , Ag ₂ C, Ag ₂ C ₂ , and Ag ₂ C ₃ clusters. The bond lengths (Å) and angles (°) calculated at MPW1PW91/SDD are marked. The relative isomer energies are indicated.	88
6-1	Infrared absorption spectra of products of laser ablation of graphite (spectrum a) and products of two-beam laser ablation of graphite and gold (spectrum b). The spectra were recorded after matrix annealing to 35K then cooling back to 12 K. The major bands due to pure carbon clusters and their reaction products with gold at 1845.2 and 1275.7 cm ⁻¹ are indicated.....	98
6-2	Infrared spectra of reaction products from laser ablation of Au and ¹² C (spectrum a) and from laser ablation of Au and ^{12/13} C (spectrum b). The bands marked by vertical dashed and dotted lines are tentatively assigned to isotopomeric partners of the 1275.7 cm ⁻¹ band. The bands marked by vertical dotted lines are due to: C ₃ H (1824.4 cm ⁻¹), ^{100,101} C ₁₂ (1817.9 cm ⁻¹), ¹⁰³	99
6-3	Infrared spectra of reaction products from laser ablation of Cu and ^{12/13} C (spectrum a), Ag and ^{12/13} C (spectrum b) and Au and ^{12/13} C (spectrum c) in 1750-1850 cm ⁻¹	

	region. The bands marked are assigned to isotopomeric bands for $\text{Cu}^{12/13}\text{C}_3$, $\text{Ag}^{12/13}\text{C}_3$ and $\text{Au}^{12/13}\text{C}_3$	100
6-4	Optimized equilibrium structure for the AuC_3 cluster. The bond lengths (\AA) and angles ($^\circ$) calculated at MPW1PW91/LanL2DZ (italic type, top) and at MPW1PW91/SDD (normal type) are marked.....	105
7-1	Experimental Setup for Ion Mass Selection and Trapping.....	111

Abstract of Dissertation Presented to the Graduate School
of the University of Florida in Partial Fulfillment of the
Requirements for the Degree of Doctor of Philosophy

VIBRATIONAL SPECTROSCOPY OF ASTROPHISICAL SPECIES

By

Yun Wang

May 2009

Chair: Martin Vala
Major: Chemistry

Identifications of the species responsible for the unidentified interstellar infrared (UIR) emission bands and the diffuse interstellar absorption (DIB) bands are the two of the major challenges in astrochemistry today. Polycyclic aromatic hydrocarbons (PAHs) have been proposed as the carriers of both signals. Carbon chain clusters and metals have both been detected in the interstellar medium. In this dissertation, reactions of iron with PAHs, and metals (copper, silver and gold) with carbon clusters were investigated. Matrix isolation spectroscopy coupled with density functional (DFT) calculations have been employed throughout this research.

Laser ablated iron atoms and evaporated or sublimed benzene, naphthalene, fluorene, pyrene, or coronene were trapped together in solid Ar at 12K. Neutral Fe(benzene), Fe(benzene)₂, Fe(naphthalene), Fe(fluorene), Fe(pyrene) and Fe(coronene) complexes were formed in the experiments and their infrared absorption spectra obtained. Theoretical calculations of the equilibrium geometries, stabilities, and harmonic vibrational frequencies of these complexes have been carried out using density functional theory. The calculations show that the dissociation energies (D_0) of neutral Fe(PAH) complexes are substantially smaller than their cationic counterparts, indicating that the neutral complexes are less tightly bonded.

Reactions of laser-ablated metal (copper, silver and gold) atoms with carbon clusters were investigated in excess argon matrices. Fourier transform infrared absorption spectra, with the assistance of ^{13}C -isotopic substitution experiments and comparison with theoretical calculation, have led to the identification of near-linear CuC_3 , AgC_3 and AuC_3 clusters. Photo-induced isotopic scrambling was observed in the $\text{Cu}^{1213}\text{C}_3$ clusters and explained via a computed potential energy surface (PES) of this reaction. The mechanism for the photoscrambling is shown to involve the formation of a bicyclic CuC_3 isomer. The formation of small metal-carbon clusters, Cu_mC_n and Ag_mC_n ($m=1, 2$; $n=1-3$) were also explored theoretically.

CHAPTER 1 ASTROPHYSICAL BACKGROUND

For decades, astronomers have been intrigued and puzzled by what exists in the extraterrestrial space. There has been accumulation of evidences that the molecules necessary for the evolution of life on earth were formed in the depths of space.¹ To understand the chemistry of interstellar species and ultimately, the origin of life, we must first identify the molecules found in space. Determining the chemical composition of the materials in the space, especially the interstellar medium (ISM) has therefore become an active area of research in the field of astrochemistry. The molecules found so far have been determined by either radio astronomy, infrared spectroscopy, or visible/ultraviolet spectroscopy.² Of primary interest to spectroscopists are the signals from the interstellar space, called the “unidentified” interstellar infrared emission bands (UIRs)³⁻⁵ and the diffuse interstellar absorption bands (DIBs).^{6,7} Identification of the carriers of the UIRs and DIBs is still a major challenge for spectroscopists and astrochemists despite considerable effort.

The Interstellar Medium

Outer space is not a complete vacuum. The material which occupies the space between the stars is called the interstellar medium (ISM). The ISM contains ordinary matter, cosmic rays and magnetic fields. Approximately 99% (by mass) of the interstellar medium is made up of gas and the remaining 1% is dust.⁸ The interstellar gas consists of neutral atoms and molecules as well as ions and electrons. Hydrogen and helium are the major components of interstellar gas, which constitute about 75% and 24% of the total interstellar mass. Other chemical elements, such as carbon, nitrogen, oxygen and some heavier elements (metals) make up the remaining 1%.² The density of the interstellar gas is very low, with an average density of 1 atom per cubic centimeter, which is comparable to the best vacuum that we can achieve in laboratory. Although the

interstellar medium is extremely dilute, it still accounts for 20-30% of the mass of our galaxy because the amount adds up over the vast distance between stars.¹ The interstellar medium is a dynamic system: old stars die and spew matter and energy back into the ISM. Eventually, new stars form from the recycled interstellar material.

The interstellar medium is not homogeneous. A wide range of densities and temperatures co-exist in the interstellar space. Densities, denoted by the number of hydrogen nuclei n_H , vary from 10^{-3} to 10^8 cm^{-3} ; and temperatures found in different regions can range from 10 K up to 10^7 K.⁹ The interstellar medium contains three different phases, defined by their densities and temperatures: the cold molecular clouds, warm diffuse clouds and the hot ionized gas.¹⁰ The cold molecular clouds ($T \sim 10\text{-}100$ K) are also called dark clouds because they block the lights from background stars. The densities of the molecular clouds range from 10^2 to 10^6 cm^{-3} . Therefore, the cold molecular clouds contribute roughly half of the interstellar mass although they occupy only a small portion ($\sim 1\text{-}2\%$) of the space. The diffuse clouds consist of cold atomic gas ($T \sim 100$ K) and are almost transparent to background starlight except at some specific absorption lines. They have moderate densities ($n_H \sim 10^{-1} \text{ cm}^{-3}$) and temperatures ($T \sim 10^4$ K) and therefore provide ideal sightlines for absorption measurements in the ultraviolet and visible (UV/Vis) region against background stars. The hot ionized clouds are very diluted, with densities only 10^{-3} cm^{-3} and temperatures as high as 10^6 K.¹⁰

Most molecules in the ISM have been identified via radio or microwave methods. However, this technique can only detect molecules with permanent dipole moments. Non-polar molecules, such as H_2 , C_5 and C_6H_6 , were identified using infrared, UV/Vis spectroscopy.¹¹ The first molecule that has been detected in the ISM was the methyldyne radical (CH) in 1937.¹² To date, over 140 molecules have been identified in the ISM, with number of atoms ranging from 2

to 13.¹¹ Glycine, the simplest amino acid necessary for life, was claimed to be observed in the interstellar medium in 2003,¹³ but its discovery was accompanied by some controversy.^{14,15} The molecules identified so far in the interstellar medium are listed in Table 1-1. Over 75% of these interstellar molecules are carbon-bearing species.

Table 1-1. List of identified interstellar molecules

Number of atoms	Molecular Formula
2	H ₂ , CO, CSi, CP, CS, NO, NS, SO, HCl, NaCl, KCl, AlCl, AlF, PN, SiN, SiO, SiS, NH, OH, C ₂ , CN, HF, FeO, LiH, CH, CH ⁺ , CO ⁺ , SO ⁺ , SH, O ₂ , N ₂ , CF ⁺
3	H ₂ O, H ₂ S, HCN, HNC, CO ₂ , SO ₂ , MgCN, MgNC, NaCN, N ₂ O, NH ₂ , OCS, CH ₂ , HCO, C ₃ , C ₂ H, C ₂ O, C ₂ S, AlNC, HNO, SiCN, N ₂ H ⁺ , SiNC, <i>c</i> -SiC ₂ , HCO ⁺ , HOC ⁺ , HCS ⁺ , H ₃ ⁺ , OCN ⁻ , HCP, CCP
4	NH ₃ , H ₂ CO, H ₂ CS, C ₂ H ₂ , HNCO, HNCS, H ₃ O ⁺ , SiC ₃ , C ₃ S, H ₂ CN, <i>c</i> -C ₃ H, <i>l</i> -C ₃ H, HCCN, CH ₃ , C ₂ CN, C ₃ O, HCNH ⁺ , HOCO ⁺ , C ₃ N ⁻
5	CH ₄ , SiH ₄ , CH ₂ NH, NH ₂ CN, CH ₂ CO, HCOOH, HCC-CN, HCC-NC, <i>c</i> -C ₃ H ₂ , <i>l</i> -C ₃ H ₂ , CH ₂ CN, H ₂ COH ⁺ , C ₄ Si, C ₅ , HNCCC, C ₄ H, C ₄ H ⁻ , HCOCN
6	CH ₃ OH, CH ₃ SH, C ₂ H ₄ , HC ₄ H, CH ₃ CN, CH ₃ NC, HCONH ₂ , HCC-COH, HC ₃ NH ⁺ , HC ₄ N, C ₅ N, C ₅ H, H ₂ CCCC, H ₂ CCNH, <i>c</i> -H ₂ C ₃ O
7	CH ₂ CHOH, <i>c</i> -C ₂ H ₄ O, HCOCH ₃ , H ₃ C-CC-H, CH ₃ NH ₂ , CH ₂ CHCN, HCC-CC-CN, C ₆ H, C ₆ H ⁻
8	CH ₃ COOH, HCOOCH ₃ , HOCH ₂ COH, H ₃ C-CC-CN, H ₂ C ₆ , HC ₆ H, C ₇ H, H ₂ C=CH-COH, CH ₂ CCHCN, H ₂ NCH ₂ CN
9	(CH ₃) ₂ O, CH ₃ CH ₂ CN, CH ₃ CH ₂ OH, CH ₃ C ₄ H, HCC-CC-CC-CN, C ₈ H, CH ₃ CONH ₂ , C ₈ H ⁻ , CH ₃ CHCH ₂
10	(CH ₃) ₂ CO, HOCH ₂ CH ₂ OH, H ₃ C-CH ₂ -COH, CH ₃ C ₄ CN
11	HC ₉ N, CH ₃ C ₆ H
12	C ₆ H ₆
13	HC ₁₁ N

Unidentified Interstellar Infrared Emission Bands

The unidentified interstellar infrared emission bands (UIRs) were discovered in 1973.³ They are a series of emission bands observed from a variety of objects in space, including planetary nebulae, H II regions, post-asymptotic giant branch (AGB) stars, and some regions of the Milky Way and other galaxies. All of the above regions contain interstellar matter and are full of ultraviolet radiation. Figure 1-1 shows the infrared spectra of three different objects in the interstellar medium.¹⁶

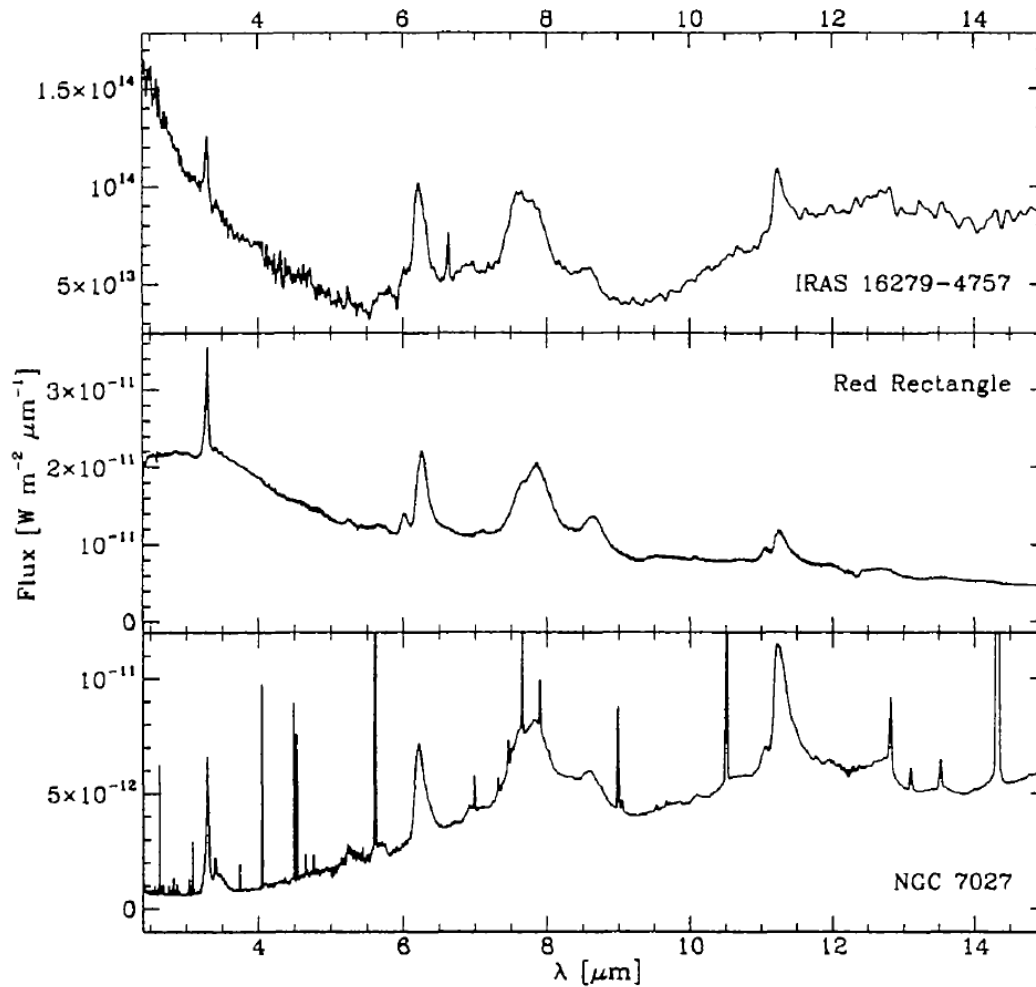


Figure 1-1. The emission spectra of the post-AGB objects, IRAS 16279-4757, the Red Rectangle, and the planetary nebula, NGC 7027.¹⁶

Although the intensity distribution of each individual bands is different for spectra from a variety of interstellar environments, the band positions are very similar; they all have dominant infrared emission features at 3.3, 6.2, 7.7, 8.7 and 11.3 μm (3030, 1610, 1280, 1150 and 890 cm^{-1}).³⁻⁵ These features could not be matched to any single or mixture of atomic lines. The identity of the carriers of these interstellar bands has become a topic of active and long-standing interest in the astrochemistry community.

Polycyclic aromatic hydrocarbons, also known as PAHs, are believed to be present in the interstellar medium and have been proposed as the carriers of the UIR bands. The proposal that the UIR bands are originated from gas-phase, neutral PAHs was first suggested by Leger and Puget in 1984.¹⁷ Shortly thereafter, Allamandola et al. argued that PAH cations could be the source of these bands.¹⁸ Later, it was proposed that the UIR bands cannot be explained solely on the basis of neutral PAH species, but that cationic PAHs are a significant component. In other words, a mixture of neutral and ionic PAHs is responsible for the interstellar bands.^{19,20} Figure 1-2 shows that the laboratory infrared spectra of a mixture of neutral and cationic PAHs match the observed UIR bands quite well.²⁰

The PAH model entails several major parts: first, the interstellar emission is due to infrared fluorescence from gas phase molecules excited by the absorption of single ultraviolet and visible photons instead of thermal emission from a solid material;¹⁷ second, the carriers are carbon-rich because the fraction of the total infrared energy that is emitted through these features is closely related to the density of carbon; third, the carriers must be stable enough to survive under the very harsh environment of the interstellar medium; also, the relative band intensities can be different but the features are correlated, which indicates that the carriers belong to a single class of chemical species, because the vibrational transitions, such as C-C or C-H stretching or

bending modes, are similar for most PAH molecules; and, last, but not least, the proposed carriers have an infrared spectrum that matches well with the UIR bands, both in positions and relative band intensities. The PAH hypothesis is now widely accepted. However, the exact mixture of PAHs and the mechanism of formation of interstellar PAHs are still unknown.

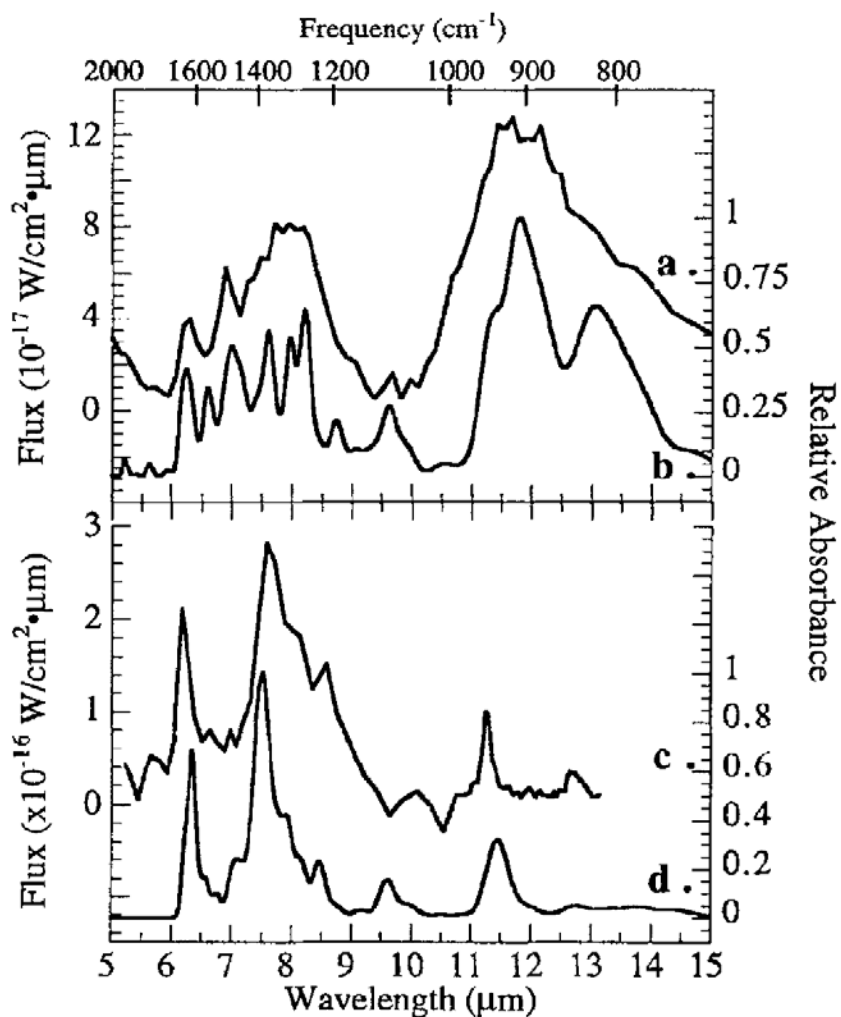


Figure 1-2. Comparison of UIR bands with PAH model. Top: (a) emission spectrum from the proto-planetary nebula IRAS 22272+5435 compared with the (b) absorption spectrum produced from a mixture of neutral and cationic PAHs. Bottom: the (c) emission spectrum from the Orion ionization ridge compared with the (d) absorption spectrum produced from a mixture of fully ionized PAHs.²⁰

Another Hypothesis is that long chain carbon clusters should also be considered as the carriers of the UIR bands.²¹ Although researchers suggests that only a millionth of the cosmically

available carbon exist in the form of carbon chains,²² small carbon clusters such as C_3 and C_5 have still been detected in the circumstellar cloud of the carbon star IRC+10216 using IR detection methods.^{23,24} The emission mechanism of the long carbon chain model is fundamentally different from the PAH model. It states that after UV or visible absorption into one of the many $\pi\pi^*$ electronic excited states, the excess energy in the carbon chain internally converts to the lowest-lying excited electronic state. Then electronic emission from this excited state to the ground state occurs. This differs from the PAH model in that the emission is electronic in nature, not vibrational. The length of the carbon chain dictates where in the infrared region the emission takes place. Figure 1-3 shows the position of the 0-0 transitions of some even C_n^- ($18 < n < 36$) carbon cluster bands coincide with some of the UIR bands.²¹ For instance, the band assigned to C_{24}^- and C_{36}^- lies at 3.2787 and 6.1 μm , respectively, which roughly fit with the broad UIR band at 3.29 and 6.2 μm . Extension of the plot in Figure 1-3 indicates that C_{24}^- and C_{52}^- could be responsible for the 7.8 and 11.3 μm UIR bands.

The long carbon chain model has been challenged on the grounds that carbon chain anions might not form and survive under the harsh conditions of the interstellar environment.^{25,26} However, the negative molecular ions C_6H^- and C_8H^- have been identified in the Galactic molecular source TMC-1 very recently.²⁷⁻²⁹ $C_{10}H^-$ was calculated and anticipated to be present at comparable abundance to C_6H^- and C_8H^- .³⁰ Even larger anions could possibly be observed because the abundance is expected to change little as the length of the carbon chain increases. Therefore, the long carbon chain model should gain more attention in the future.

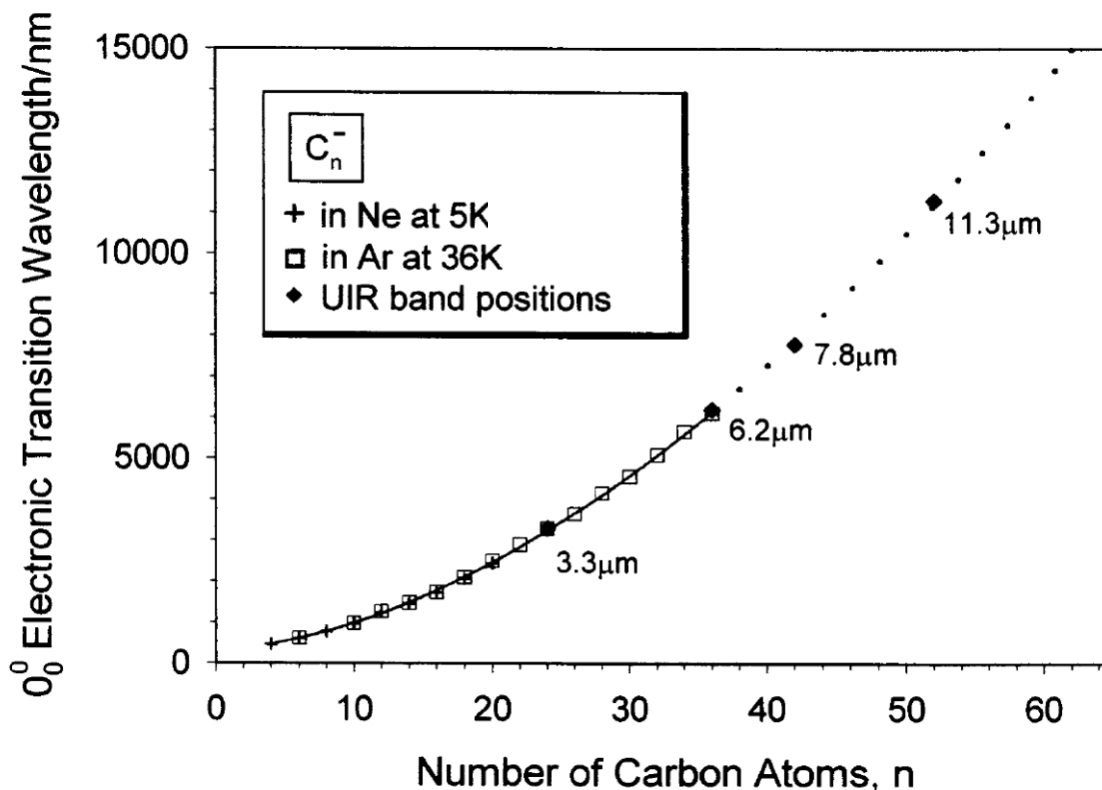


Figure 1-3. Plot of the electronic transition wavelength for even-numbered carbon cluster anions observed in an Ar matrix at 36 K versus the number of carbons in the cluster chain.²¹

Diffuse Interstellar Absorption Bands

The diffuse interstellar absorption bands (DIBs) are a series of absorption bands that are observed in the spectral range extending from the UV to the near IR (400 – 1300 nm). First discovered in 1922, the DIB bands have become one of the longest-standing astronomical spectroscopic mysteries.³¹ A synthetic spectrum of DIBs towards the hot B0 II star BD+63° 1964 is displayed in figure 1-4.³² This object is now commonly used as a reference target in the search of new DIBs. DIB bands exhibit a large diversity of band profiles: the full bandwidth at half-maximum (FWHM) range from 0.06 to 4 nm,³³ and the intensities of most DIB bands are not correlated to each other, which means there must be many carriers rather than just one carrier. To date, over 300 DIBs have been detected in the interstellar medium, but no definitive

identification of the carriers of these bands has been reported yet. Carbon clusters or chains,^{34,35} carbon rings or fullerenes,^{36,37} and PAHs have all been suggested as potential carriers for some DIB bands.^{25,38} However, some recent research indicates that PAHs having 30 or more carbon atoms, especially in their cationic forms, are the strongest candidates as DIB carriers.³⁹ Since such large PAHs are experimentally difficult to vaporize and keep in the gas phase as cations, usually solid-state spectroscopy is employed in studying the spectra of these PAH cations.^{40,41} However, only gas-phase spectroscopy can provide the information of specific molecules that are responsible for the DIB bands.

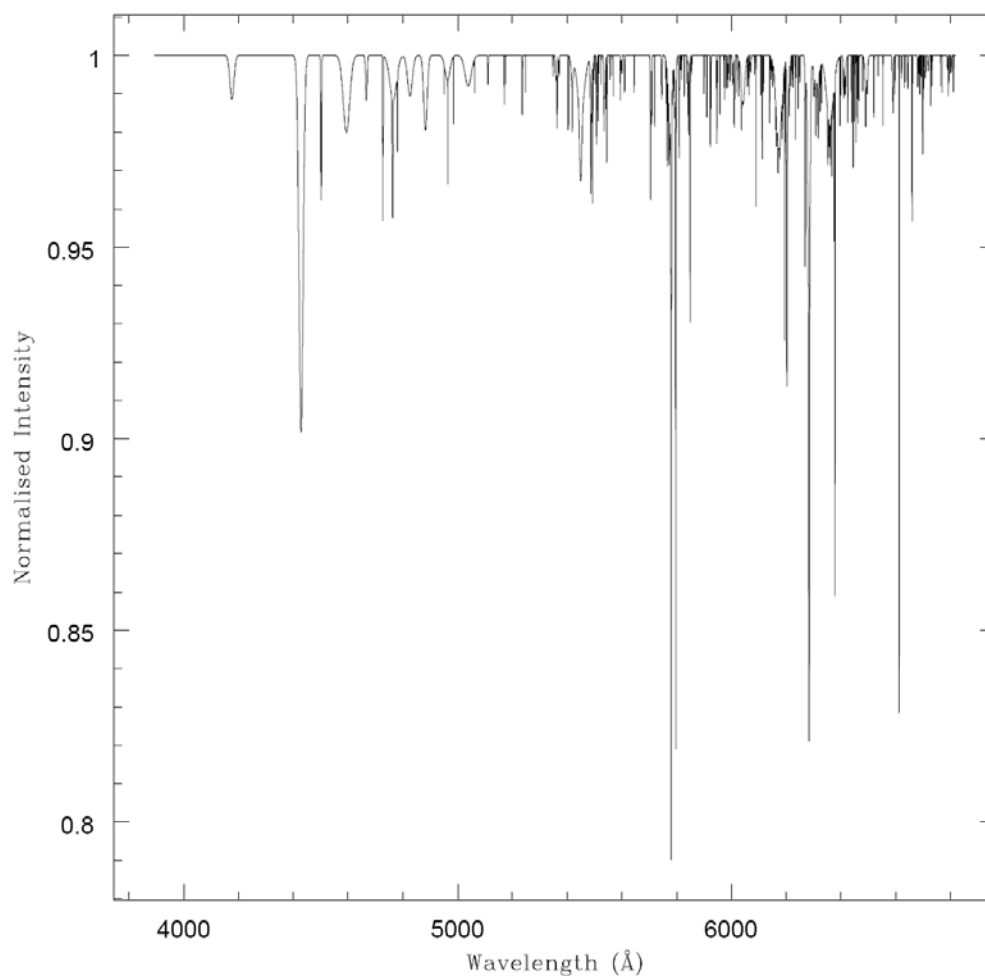


Figure 1-4. The synthetic spectrum of the hot B0 II star BD+63° 1964.³²

Metal Depletion in the ISM

Other than the most abundant elements hydrogen (H) and helium (He), there are many heavier elements present in the interstellar medium, such as carbon (C), nitrogen (N), oxygen (O), silicon (Si), iron (Fe) and copper (Cu). Figure 1-5. shows the elemental composition of our solar system.⁴² The heavier elements were produced through stellar nucleosynthesis.

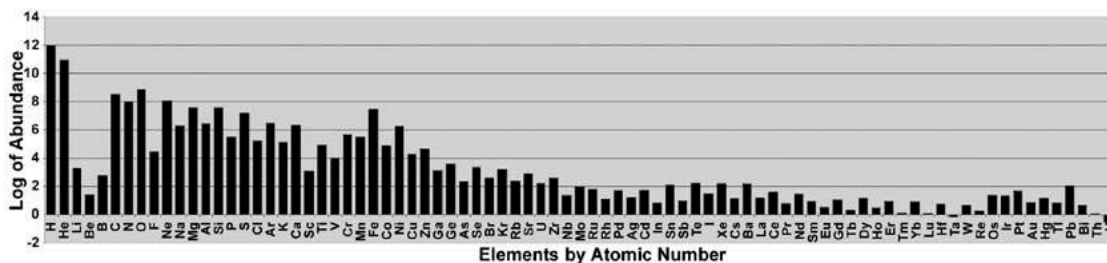


Figure 1-5. The elemental composition of the solar system. The abundance of hydrogen is arbitrarily set to 10^{12} so that the smallest abundance in the graph is about 1.⁴²

Since the interstellar medium is quite well mixed, it is expected that the abundances of these interstellar element is similar to the cosmic abundance in the Sun's atmosphere or in meteorites. However, observations of interstellar absorption lines show that a number of elements are “depleted” from the gas-phase by large factors. Table 1-2. lists the abundance and depletion factors of some interstellar elements. The depletion factor for a certain element (i) is defined relative to its “cosmic” abundances by $\delta_i \equiv [(N_i / N_H) / (N_i / N_H)_s]$, where N_i is the average number of the element, N_H is the average number of hydrogen atoms and the notation “s” refers to the numbers in our solar system.⁴³ The abundance relative to H in Table 1-2 was arbitrarily cut off at 10^{-8} . The abundances of the “heavy elements” relative to H add up to 1.60×10^{-3} .

The depletion factors vary from around 0.5 (C, O), to values around 0.1 (Cu), 0.01 (Fe), or even lower to around 0.002 (Ca, Ti). Also, depletion tends to be more severe in regions with

higher density and lower temperature.⁴⁴ It has been proposed that the high depletion of interstellar iron could be due to iron complexes with various interstellar PAHs.^{45,46}

Table 1-2. Astrophysically abundant elements and their depletion factors.⁴³

Element	Abundance	Depletion Factor	Element	Abundance	Depletion Factor
H	1.000	1.0	Cl	1.86 (-7)	0.5
He	0.0977	1.0	Ar	3.63 (-6)	1.0
C	3.63 (-4)	0.5	K	1.32 (-7)	0.5
N	1.12 (-4)	0.6	Ca	2.29 (-6)	0.003
O	8.51 (-4)	0.6	Ti	9.77 (-8)	0.002
F	3.02 (-8)	0.5	V	1.00 (-8)	?
Ne	1.23 (-4)	?	Cr	4.68 (-7)	0.03
Na	2.14 (-6)	0.25	Mn	2.45 (-7)	0.07
Mg	3.80 (-5)	0.2	Fe	4.68 (-5)	0.01
Al	2.95 (-6)	0.05	Co	8.32 (-8)	?
Si	3.55 (-5)	0.1	Ni	1.78 (-6)	0.04
P	2.82 (-7)	0.6	Cu	1.62 (-8)	0.1
S	1.62 (-5)	0.6	Zn	3.98 (-8)	0.6

CHAPTER 2 MATRIX ISOLATION SPECTROSCOPY METHOD

Matrix isolation spectroscopy and theoretical calculations are two of the most popular and powerful tools in the study of astrochemistry. In this dissertation, both two techniques were employed to study the molecules of interest. Matrix isolation spectroscopy technique involved in this work is discussed in this chapter. Details of Density Functional Theory (DFT) calculation for each project will be provided in the following chapters individually.

Fundamentals of Matrix Isolation Spectroscopy

The matrix isolation method was first reported by Whittle, Dows, and Pimentel in 1954.⁴⁷ Numerous books and articles have been published on this subject since then. The original idea of matrix isolation is to trap some free radicals and other unstable substances in a solid matrix of inert material at very low temperature (4 – 30 K), so that the matrix will inhibit diffusion of the trapped molecules, thus holding the active molecules effectively immobile in a nonreactive environment.⁴⁷ The principle of matrix isolation is illustrated in Figure 2-1. The guest particles can be generated by thermal evaporation, pyrolysis, microwave discharge, photolysis or laser ablation. The matrix materials are usually chemically inert and optically transparent from far infrared to ultraviolet. Therefore, full range of IR or electronic spectra can be recorded. For the reasons mentioned above, some noble gases are often used as matrix, such as argon, neon, xenon because they have no absorptions in the infrared range and they seldom react with other species. Nitrogen, although not rare gas, can also be chosen as matrix material.

Matrix isolation spectroscopy has become a powerful tool in the study of astrophysical species. The low temperature and high vacuum are two essential conditions for matrix isolation spectroscopy, which can simulate the interstellar environment. Matrix isolation spectroscopy is

also very efficient for studying some unstable species which may possibly exist in the interstellar medium.

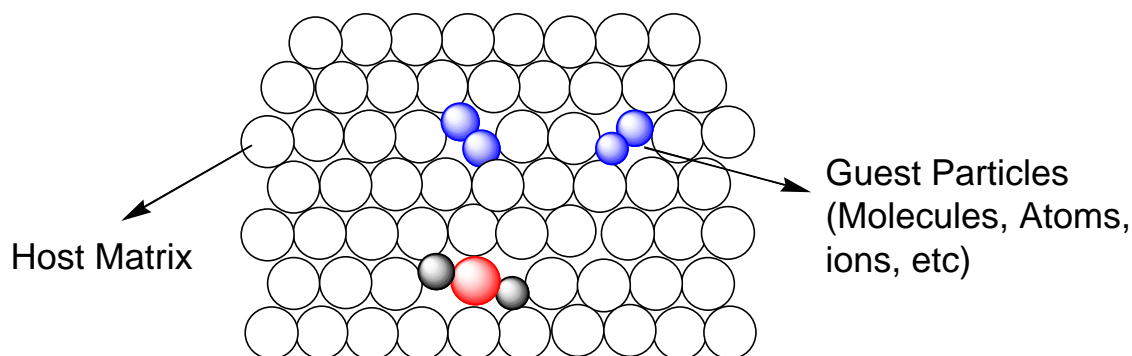


Figure 2-1. Illustration of the principle of matrix isolation. The inert host matrix isolates guest particles from each other and prevents reaction.

Experimental Method

Experimental Setup

Matrix isolation experiments were conducted in a high vacuum chamber at very low temperature. The chamber was inserted into a FT-IR spectrometer (MIDAC M2000 or NICOLET Magna 560), allowing spectra collection during or after deposition. The chamber was pumped by a diffusion pump, which was connected to a rotary pump. Before cooling down, the pressure in the chamber is on the order of 10^{-6} torr. After the system is cooled down to about 12 K, the pressure drops to around 10^{-7} torr, which is called the background pressure for the experiments. The deposition surface was a cesium iodine (CsI) window mounted in a copper holder, which is cooled down to 12 K by a closed-cycle helium cryostat (APD Cryogenics Inc.). The window temperature was monitored by a thermocouple temperature controller via an iron-gold thermocouple attached to the top of the copper holder. During deposition, the species of interest in this research was produced using different techniques, such as laser ablation and thermal evaporation. Argon gas or a mixture of argon and other gases was introduced into the chamber and directed towards the deposition window through a stainless steel tube with a needle

valve. The gas flow was controlled by adjusting the needle valve. The mixture of the reaction products and argon gas were trapped onto the CsI window cooled to 12 K. After 2 – 5 hours deposition, infrared absorption spectra in $700 - 4000 \text{ cm}^{-1}$ region were collected with $0.5 - 1.0 \text{ cm}^{-1}$ resolution. Matrix annealing to 35 K followed by recooling back to 12 K and matrix photolysis by applying UV-visible medium pressure 100W Hg lamp were also involved in most runs. A diagram of the experimental setup for the Fe(PAH) experiments is shown in Figure 2-2.

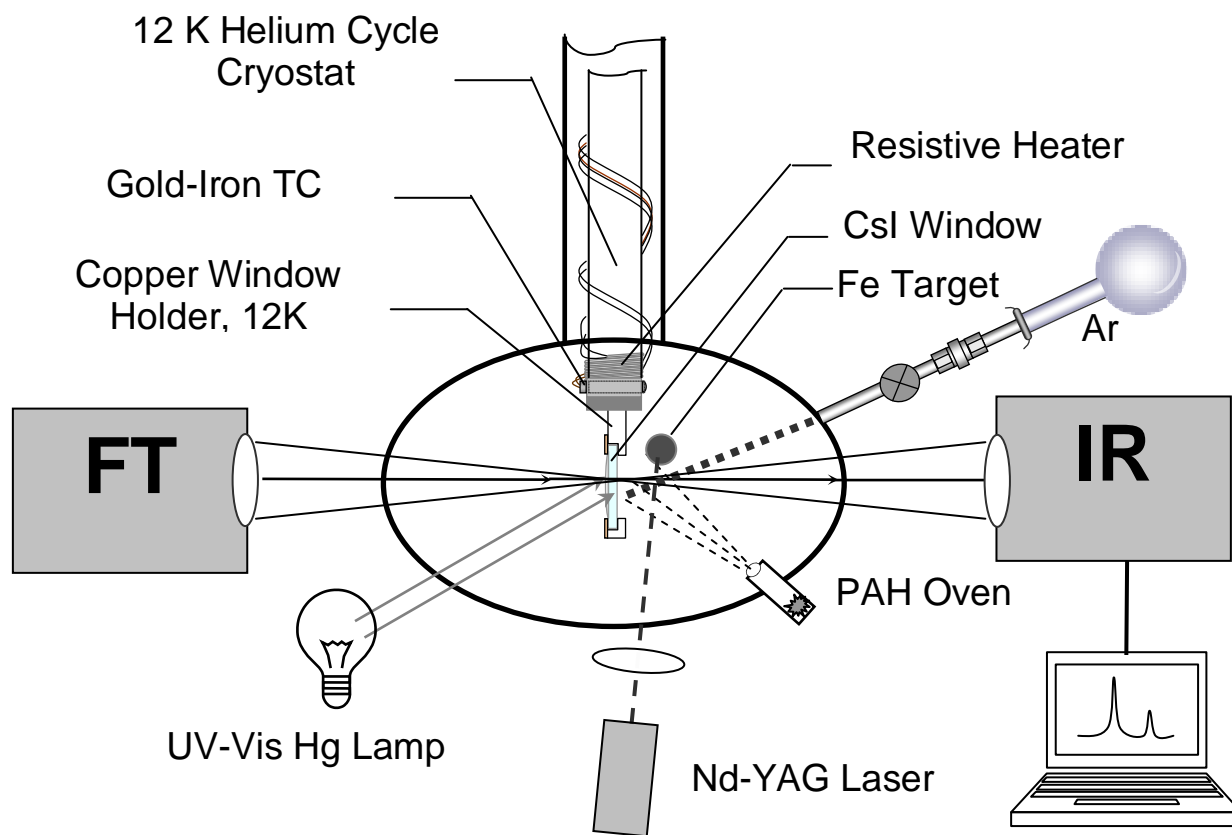


Figure 2-2. Experimental setup for Fe-PAH experiments.

For copper-carbon, silver-carbon and gold-carbon experiments, the experimental setup was basically the same as the Fe-PAH experiments but with small modification, which was displayed in Figure 2-3. The pulsed Nd-YAG laser beam was split into two beams. One beam (with intensity of approximately 60%) was directed by prism P1 and focused by lens L1 on surface of piece of Cu/Silver/Gold metal to ca. 0.5 mm spot diameter, while second beam (with intensity

approximately 40%) was focused on the pressed pellet of mixture of ^{12}C and ^{13}C powders (ISOTECH, Inc.) to spot of 2 – 3 mm diameter. The distance two spots was approximately 4 – 5 mm and they were located close to the holder of the CsI window. The beamsplitter used was an ordinary glass plate. The intensity ratio of reflected beam from surface of this plate to the intensity of transmitted beam can be change by rotating the plate (*i.e.* change the incidence angle). For such simple beamsplitter, if the incidence angle is set to about 80 degrees the intensities of reflected and transmitted beams are equal (*i.e.* 50% each) as is governed by Fresnel's formula for TE light polarization.⁴⁸ Both L1 and L2 lenses were mounted on the micrometer screw-driven tables allowed periodically to reposition the focussed laser beams over fresh regions of carbon and copper surfaces.

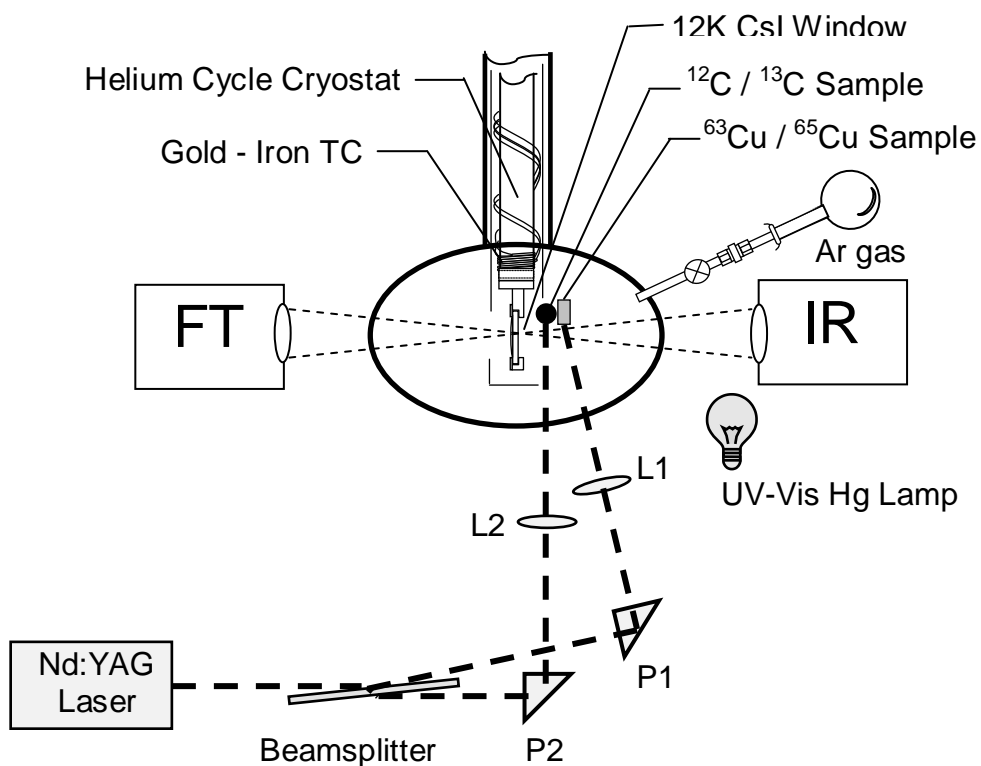


Figure 2-3. Experimental setup for copper-carbon experiments.

Laser Ablation

Laser ablation was employed to generate metal (Fe, Cu, Ag and Au) atoms and carbon clusters. A pulsed Nd:YAG laser (1064 and 532 nm, 0.2 – 0.5 W, 10 Hz) was used to vaporize metal target and pressed pellet samples which may contain ^{12}C or $^{12}\text{C}/^{13}\text{C}$ mixture. For copper-carbon, silver-carbon and gold-carbon experiments, synchronized dual-beam laser ablation of metal and carbon sample was performed while single-beam laser ablation of iron sample was used for Fe-PAH experiments. Standard carbon and metal samples were used without further purification: ^{12}C (powdered graphite, natural abundance ^{12}C (98.9%) and ^{13}C (1.1%)), ^{13}C (99%, ISOTECH), Cu (natural abundance: ^{63}Cu (69.2%) and ^{65}Cu (30.8%), SPEX), Ag (natural abundance: ^{107}Ag (51.8%) and ^{109}Ag (48.2%), SPEX), Au (^{197}Au (99.9%), Kurt J. Lesker).

Generation of PAHs

Since the vapor pressures of PAHs decrease with increasing molecular size, different methods were necessary to introduce PAHs into the cryostat chamber. Benzene vapor was mixed with argon (1% benzene) and injected through a needle valve. Naphthalene was introduced directly into the chamber through a leak valve. Fluorene was introduced similar as naphthalene but with heating. Pyrene and coronene were sublimed from a resistively-heated oven located inside the cryostat chamber, close to the iron sputter target.

CHAPTER 3 VIBRATIONAL SPECTROSCOPY OF NEUTRAL COMPLEXES OF IRON AND POLYCYCLIC AROMATIC HYDROCARBONS

Introduction

Recently polycyclic aromatic hydrocarbons (PAHs) and their ions have garnered enormous interest because of their possible involvement in interstellar chemistry. First proposed by Leger & Puget (1984) and Allamandola et al (1985) to account for the unidentified interstellar infrared (UIR) emission bands, PAHs are now believed to be present in many regions of the interstellar medium (ISM). The UIR bands have been observed from reflection and planetary nebulae, H II regions, post-AGB objects, plus some regions of the Milky Way and other galaxies.^{17,18} Though their presence is now widely accepted, specific PAHs have not yet been identified as carriers of the UIR bands, principally due to band width and frequency overlap problems.

Iron, another important component in the interstellar medium, is one of the most abundant elements.⁴⁹ Only H, He, O, C, N, S, Mg, and Si are more abundant.⁵⁰ It has been established observationally that the cosmic abundance of iron in the ISM is depleted,⁵¹⁻⁵³ but the reason for its depletion is not known. While the depletion factor, taken as the ratio of the average elemental abundance in our solar system to that in the ISM, is about 1-3 for carbon, oxygen, nitrogen and sulfur; for magnesium, silicon and iron, however, it is substantially larger: 34, 42, and 100, respectively.⁵⁰

French researchers have proposed a possible mechanism for the depletion of iron. Serra et al. proposed that since collisions between iron and PAHs probably occur frequently in the ISM, such collisions could lead to stable iron-PAH complexes. The sequestration of iron in a complexed form could then explain the unusual depletion of elemental iron.⁵⁴ In addition, Chaudret and co-workers have also proposed that *ionic* Fe(PAH)⁺ complexes could be responsible for the UIR bands.⁵⁵ This naturally raises the companion question: could *neutral*

iron-PAH complexes could also act as contributors to the UIR bands? The goal of this study was to determine whether neutral iron-PAH complexes were stable, whether they could account for the depletion of iron in the ISM, and whether they might be responsible for the UIR bands.

While some studies have been reported on Fe-PAH complexes, by far the bulk of previous studies have dealt with the Fe-benzene system. Timms was the first to study the iron-benzene system and reported a complex of unknown stoichiometry.⁵⁶ Efner et al. studied iron and benzene in argon matrices and reported the formation of the $\text{Fe}(\text{C}_6\text{H}_6)$ complex.⁵⁷ Aleksayan and Kurtikyan, and Shobert et al. studied iron and benzene in matrices as well and assigned the newly observed infrared absorption bands to the $\text{Fe}(\text{C}_6\text{H}_6)_2$ complex.^{58,59} Morand and Francis also studied the iron-benzene system and assigned new bands in the visible spectrum to a $(\eta^6\text{-C}_6\text{H}_6)(\eta^4\text{-C}_6\text{H}_6)\text{Fe}$ complex.⁶⁰ Parker and Peden co-deposited iron and benzene in krypton matrices and used Mössbauer spectroscopy to identify a number of iron-benzene complexes, including $\text{Fe}(\text{C}_6\text{H}_6)$ and $\text{Fe}(\text{C}_6\text{H}_6)_2$.⁶¹ Ball et al. studied the iron-benzene system in argon matrices by infrared spectroscopy and deduced the formation of $\text{Fe}(\text{C}_6\text{H}_6)$, $\text{Fe}(\text{C}_6\text{H}_6)_2$, and possibly $\text{Fe}_2(\text{C}_6\text{H}_6)$, complexes.⁶² However, in none of the above studies was any theoretical work reported.

Boissel and Marty et al. studied the reaction cross-sections and dissociation rates for complexes of Fe^+ and various PAHs via Fourier transform mass spectroscopy.^{63,64} Caraiman and Bohme used selected ion flow tube studies to determine the reactivity of iron complexed to coronene.⁶⁵ Using time-of-flight mass spectrometry, Duncan and coworkers studied the photodissociation dynamics of metal complexes with different ligands, including PAHs.⁶⁶⁻⁷⁰ Elustondo et al. and Morand and Francis also studied the iron-PAH system in cryogenic Ar matrices *via* infrared and UV-visible absorption spectroscopy.^{60,71} The gas-phase experimental

vibrational spectra of cationic iron complexes with benzene, naphthalene, and fluorene have been very recently reported.⁷²

In this chapter, an experimental and theoretical investigation of the vibrational spectroscopy of neutral Fe(PAH) complexes was presented. Infrared absorption spectra of neutral complexes of iron with benzene, naphthalene, fluorene, pyrene, and coronene in solid Ar at 12K have been obtained. Supporting calculations of the equilibrium geometries, stabilities, and harmonic vibrational frequencies of these complexes have been carried out using density functional theory (MPW1PW91/6-31+G(d,p) method) using a modified Perdew-Wang exchange and correlation functional/basis set.

Computational and Experimental Details

Computational Details

The geometries, energies, and harmonic vibrational frequencies of Fe(PAH) complexes were calculated using the Gaussian 03 suite of programs.⁷³ Global searches for the most stable structures of singlet, triplet and quintet ground state multiplicities for the complexes were carried out using the MPW1PW91/6-31+G(d,p) method with modified Perdew-Wang exchange and correlation functional/basis set.^{74,75} Previous work has shown that the MPW1PW91 functional is generally preferred over the frequently used B3LYP approach for equilibrium structures, harmonic frequencies and other spectroscopic parameters of metal-containing molecular systems.⁷⁶ Computed harmonic mid-IR vibrational frequencies were scaled uniformly by a factor of 0.972. This factor is the ratio of the experimental gas-phase absorption frequency (672 cm^{-1}) of the strongest CH out-of-plane mode in neutral benzene to its calculated (MPW1PW91/6-31+G(d,p)) frequency (691.3 cm^{-1}).⁷² As done previously,⁷² the scaling factors for the strongest computed CH stretching modes of Fe(benzene), Fe(benzene)₂, Fe(naphthalene), Fe(fluorene), Fe(pyrene) and Fe(coronene) were taken as 0.944, 0.944, 0.952, 0.949, 0.944 and 0.955,

respectively. These values differ substantially from previously-used mid-IR scaling factors due to the large CH stretching mode anharmonicities.⁷²

Dissociation energies, D_0 , of the Fe(PAH) complexes were determined from

$$D_0 \approx E(\text{Fe}) + E_{\text{ZPE}}(\text{PAH}) - E_{\text{ZPE}}(\text{Fe}(\text{PAH})) \quad (1)$$

where E_{ZPE} is the electronic energy corrected for the zero-point vibrational energy. Here it was assumed that Fe retains the spin multiplicity of the complex, *e.g.*, triplet for the most stable complex. Thus, the electronic energy of the $^5\text{D}_4$ quintet ground state of iron, $E(\text{Fe})$, was increased by 1.485 eV, which is the difference between the Fe atomic $^3\text{F}_4$ and $^5\text{D}_4$ states.⁷⁷ Neither the geometry nor the electronic energy of the PAH ligand in the complex was found to be modified greatly compared to uncomplexed PAH. For example, the ZPE-corrected electronic energy of Fe-complexed naphthalene, pyrene and coronene is lower than that of the ligands alone by only 0.07, 0.06 and 0.01 eV. These values increase D_0 by similar values. The small values for the correction factors validates the use of the $E_{\text{ZPE}}(\text{PAH})$ energy of the separated ligands in (1). A similar formula for D_0 was used previously in our study of cationic $\text{Fe}(\text{PAH})^+$ complexes.⁷²

Experimental Details

The experimental setup has been described in details in Chapter 2. Briefly, a pulsed Nd:YAG laser (1064 and 532 nm) was focused on a solid Fe target. The ablated iron vapor was mixed with PAH vapor and gaseous Ar and trapped on a CsI window cooled to 12 K. After 2-4 hours deposition, infrared absorption spectra were collected at 1 cm^{-1} resolution using a MIDAC M2000 FT-IR spectrometer. Most runs also involved subsequent UV-visible photolysis with a medium pressure Hg lamp, after which the IR spectra were also recorded.

Since vapor pressures of the PAHs decrease with increasing molecular size, different methods were necessary to introduce the PAHs into the cryostat chamber. Benzene vapor was mixed with argon and injected directly via a needle valve. Both naphthalene and fluorene vapors

were introduced in a similar fashion, but fluorene required some heating. Pyrene and coronene were sublimed from a resistively-heated oven located inside the cryostat chamber, close to the iron sputter target.

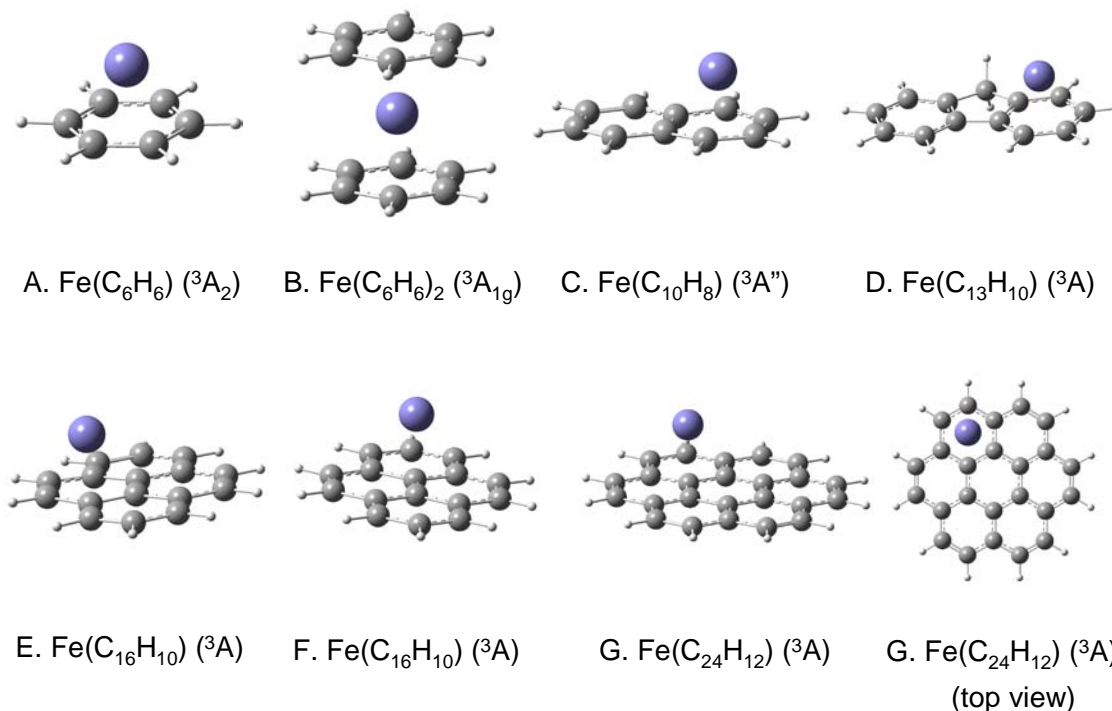


Figure 3-1. Lowest energy stable structures for the complexes of iron with benzene (C_6H_6)(**A**), bis-benzene (C_6H_6)₂ (**B**), naphthalene (C_{10}H_8) (**C**), fluorene ($\text{C}_{13}\text{H}_{10}$) (**D**), pyrene ($\text{C}_{16}\text{H}_{10}$) (**E**), pyrene (second isomer, **F**), and coronene (**G**), all optimized at the MPW1PW91/6-31+G(d, p) level of theory.

Fe(benzene) and Fe(benzene)₂ complexes

The computed equilibrium geometries for the most stable complexes are shown in Figure 3-1. Experimental infrared spectra of iron co-deposited with benzene are shown in Figure 3-2. Seven new bands (715.9, 761.3, 811.4, 952.9, 967.5, 982.8, and 1442.5 cm^{-1}) were observed after deposition. The bands at 761.3, 811.4, 952.9 and 982.8 cm^{-1} decreased after photolysis and/or annealing. They are assigned here to the Fe(benzene) complex. The other three bands (715.9, 967.5, and 1442.5 cm^{-1}) increased with matrix photolysis and annealing, and are assigned to the Fe(benzene)₂ complex. Fe(benzene)₂ bands do not decrease with photolysis probably because (1)

the radiant input energy is distributed over a larger number of modes in the bis-complex than in Fe(benzene), such that the energy is not sufficient to break the complexes' Fe – ring bond; (2) slight annealing always accompanies photolysis, with the result that benzene aggregates are preferentially produced during matrix annealing.⁷⁸ Thus the Fe(benzene) + benzene → Fe(benzene)₂ reaction is likely to be operative.

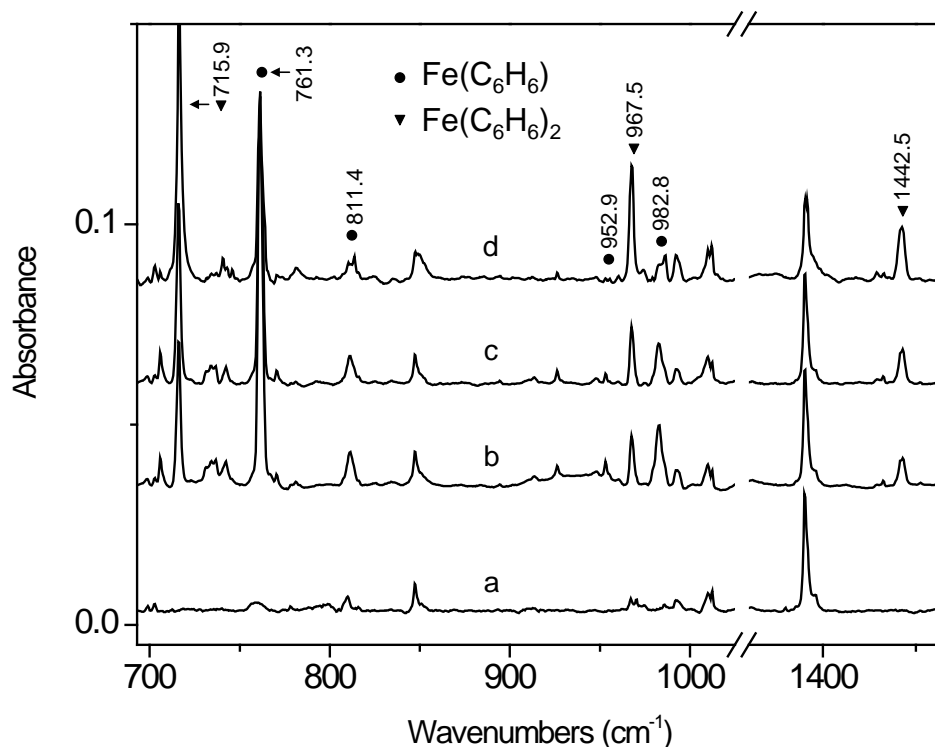


Figure 3-2. IR absorption spectrum of benzene (C₆H₆) only (a), Fe codeposited with benzene (b), after matrix UV-visible photolysis (c) and after matrix annealing at 35 K (d), all in solid Ar at 12K.

Figure 3-3 displays the synthetic experimental (experimental band positions and relative intensities with artificial 1 cm⁻¹ bandwidths) and calculated spectra for different spin multiplicities (singlet, triplet and quintet) of the Fe(benzene) complex. It can be seen that the experimental band positions and relative intensities for the triplet multiplicity matches the

calculated vibrational frequency and band intensity patterns best. Furthermore, the triplet is calculated to be the most stable of the complexes (see Table 3-1).

Our calculations also show that in the most stable mono-complex structure the iron atom is centered 1.49 Å above the benzene ring (**A** in Figure 3-1). The benzene ring is bent slightly out-of-plane (C_{2v} symmetry), as found previously for the $Fe(benzene)^+$ complex.⁷²

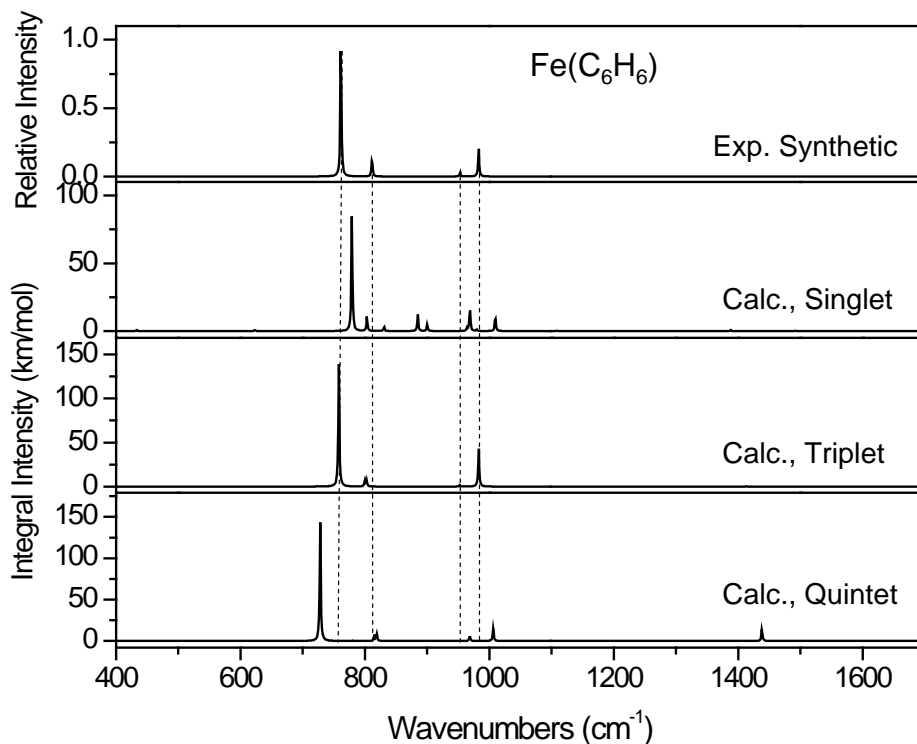


Figure 3-3. Synthetic experimental and calculated infrared absorption spectra at indicated spin state multiplicities for the $Fe(C_6H_6)$ complex.

Figure 3-4 shows the synthetic experimental and calculated spectra for the $Fe(benzene)_2$ complex. The experimental spectrum fits the calculated spectrum quite well except for the bands at 1008.7/1008.9 cm^{-1} , which are predicted but not observed. They were probably overlapped by the benzene band at 1010.9 cm^{-1} . Support of this comes from the experimental observation that

the 1010.9 cm⁻¹ band intensity increased during matrix annealing in a similar fashion to the other Fe(benzene)₂ complex bands (marked by triangles in Figure 3-2), while at the same time “pure” benzene bands (unmarked in Figure 3-2) decreased slightly. According to our calculations, the Fe(benzene)₂ complex should also be a triplet with D_{6h} symmetry and the two rings separated by 3.48 Å. Similar η⁶ – η⁶ –type coordination in the Fe(C₆H₆)₂ complexes was earlier suggested by Ball et al.⁶²

Table 3-1. Computed properties for Fe(PAH) complexes

Complex ^a	State	Sym	Do ^b kcal/mol(eV)	Rel E _{ZPE} ^c kcal/mol(eV)	r _{Fe-ring} ^d Å
A. Fe(C ₆ H ₆)	¹ A ₁	C _{2v}		42.7 (1.85)	
	³ A ₂	C _{2v}	49.1 (2.13)	0.0 (0.00)	1.49
	⁵ A ₂	C _{2v}		9.2 (0.40)	
B. Fe(C ₆ H ₆) ₂	³ A _{1g}	D _{6h}	27.2 (1.18)	0.0 (0.00)	1.74
C. Fe(C ₁₀ H ₈)	¹ A'	C _s		36.5 (1.58)	
	³ A''	C _s	44.1 (1.91)	0.0 (0.00)	1.55
	⁵ A''	C _s		1.0 (0.04)	
D. Fe(C ₁₃ H ₁₀)	¹ A	C ₁		43.4 (1.88)	
	³ A	C ₁	47.5 (2.06)	0.0 (0.00)	1.51
E. Fe(C ₁₆ H ₁₀)	³ A''	C _s	34.82 (1.51)	8.5 (0.37)	1.35
	⁵ A'	C _s		15.9 (0.69)	
F. Fe(C ₁₆ H ₁₀)	³ A	C _s	43.4 (1.88)	0.0 (0.00)	1.55
	⁵ A''	C _s		15.8 (0.69)	
G. Fe(C ₂₄ H ₁₂)	³ A	C ₁	12.0 (0.52)	0.0 (0.00)	1.53

^a The most stable complexes as optimized at MPW1PW91/6-31+G(d,p) level with equilibrium geometries shown in Figure 3-1.

^b Dissociation energies calculated using formula (1), see chapter 2.

^c Relative total electronic energy corrected for zero-point vibrational energy.

^d Iron-ring distance

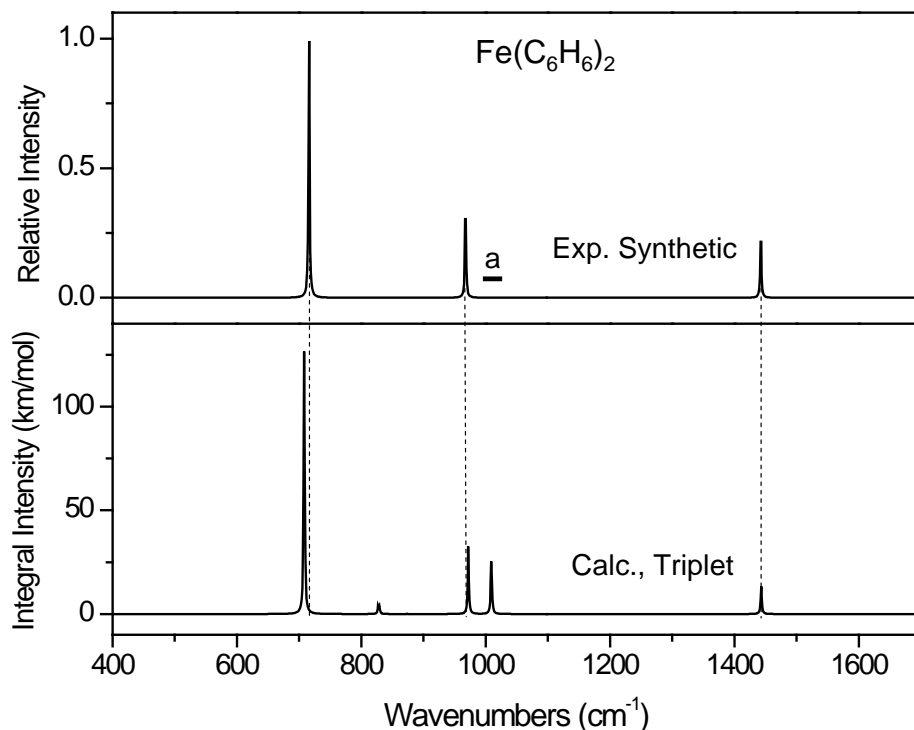


Figure 3-4. Synthetic experimental and calculated infrared absorption spectra for the $\text{Fe}(\text{C}_6\text{H}_6)_2$ complex. The inaccessible energy region overlapped with the absorption band of benzene is marked by the horizontal line (a).

Observed and calculated $\text{Fe}(\text{C}_6\text{H}_6)$, $\text{Fe}(\text{C}_6\text{D}_6)$ and $\text{Fe}(\text{C}_6\text{H}_6)_2$, $\text{Fe}(\text{C}_6\text{D}_6)_2$ frequencies and relative intensities are listed in Table 3-2 and 3-3, respectively. These results are compared to previous work in Table 3-4 and 3-5. As can be noted, our results do not agree with some previous assignments. Our band assignments are based on observation of band intensity changes after UV photolysis and matrix annealing, plus comparison with vibrational frequency calculations. The match between observed band energies and relative intensities and computed frequencies and intensities for the both mono- and bis-Fe-benzene complexes is quite good.

Table 3-2. IR absorption spectra of Fe(C₆H₆) and Fe(C₆D₆) complexes.

Mode ^a	Fe(C ₆ H ₆)		Fe(C ₆ D ₆)	
	$\nu_{\text{cal}}^{\text{b}}/\text{cm}^{-1}$	$\nu_{\text{exp}}/\text{cm}^{-1}$	$\nu_{\text{cal}}^{\text{b}}/\text{cm}^{-1}$	$\nu_{\text{exp}}/\text{cm}^{-1}$
$\varepsilon+\tau+\pi$	320.8 (0.02)		305.3 (0.03)	
$\pi+\varepsilon+\tau$	321.4 (0.02)		306.1 (0.03)	
$\pi+\varepsilon+\tau$			333.9 (0.03)	
ε	758.1 (1.00)	761.3 (1.00)	582.8 (1.00)	584.8 (1.00)
$\varepsilon+\tau$	799.9 (0.05)	811.4 (0.13)	619.4 (0.09)	631.1 (0.17)
	802.8 (0.05)		621.3 (0.09)	
$\beta+\text{R}$	982.7 (0.16)	982.8 (0.21)	779.8 (0.15)	
$\beta+\text{R}$	983.0 (0.16)		780.2 (0.15)	785.9 (0.38)
γ	952.1 (0.01)	952.9 (0.03)	909.0 (0.04)	
$\text{R}+\beta$			1255.4 (0.09)	1257.8 (0.12)
$\beta+\text{R}$			1255.6 (0.09)	
r	3048.6 (0.22)		2254.2 (0.15)	
r	3049.0 (0.22)		2254.3 (0.15)	

^a Notation used: R and r are CC and CH stretching modes, α and β are CCC and CCH in-plane bending modes, τ and ε are CCC and CCH out-of-plane vibrations, π is an iron-ring vibration, and γ is the ring breathing mode.

^b Frequencies are scaled uniformly by scaling factors of 0.972 and 0.944 for mid-IR and C-H stretching modes, respectively. The integral intensity for the 758.1 and 582.8 cm⁻¹ bands are 139.1 and 75.8 km/mol, respectively. Only modes with relative intensities equal to or larger than 0.01 are listed.

Table 3-3. IR absorption spectra of Fe(C₆H₆)₂ and Fe(C₆D₆)₂ complexes.

Mode ^a	Fe(C ₆ H ₆) ₂		Fe(C ₆ D ₆) ₂	
	$\nu_{\text{cal}}^{\text{b}}/\text{cm}^{-1}$	$\nu_{\text{exp}}/\text{cm}^{-1}$	$\nu_{\text{cal}}^{\text{b}}/\text{cm}^{-1}$	$\nu_{\text{exp}}/\text{cm}^{-1}$
$\pi+\varepsilon+\tau$	250.4 (0.71)		246.0 (1.00)	
$\varepsilon+\tau$	708.1 (1.00)	715.9 (1.00)	524.0 (0.51)	533.1 (0.51)
$\varepsilon+\tau$	826.9 (0.03)		641.5 (0.02)	
$\varepsilon+\tau$	828.9 (0.03)		642.9 (0.02)	
γ	972.0 (0.26)	967.5 (0.38)	927.1 (0.36)	922.3 (0.39)
$\beta+\text{R}$	1008.7 (0.12)	c	791.9 (0.12)	796.1 (0.31)
$\beta+\text{R}$	1008.9 (0.12)		792.2 (0.12)	
$\text{R}+\beta$	1442.8 (0.06)	1442.5 (0.27)		
	1443.4 (0.06)			
r	3057.6 (0.36)		2262.6 (0.26)	
r	3057.7 (0.36)		2262.7 (0.26)	
r	3064.8 (0.08)			

^a Notation used: R and r are CC and CH stretching modes, α and β are CCC and CCH in-plane bending modes, τ and ε are CCC and CCH out-of-plane vibrations, π is iron-ring movement, and γ is rings breathing mode (anti phase).

^bFrequencies are scaled uniformly by scaling factors of 0.972 and 0.944 for mid-IR and C-H stretching modes, respectively. The integral intensity for the 708.1 and 246.0 cm⁻¹ bands are 127.1 and 91.4 km/mol, respectively. Only the modes with relative intensities equal to or larger than 0.01 are listed.

^cThis band was not observed due to the absorption band of benzene in this region.

Table 3-4. Comparison of present work with previous IR band assignments for Fe(C₆H₆) complex.

This work		Ball et al. ⁶²		Efner et al. ⁵⁷
Mode ^a	$\nu_{\text{cal}}^{\text{b}} / \text{cm}^{-1}$	$\nu_{\text{exp}} / \text{cm}^{-1}$	$\nu_{\text{exp}} / \text{cm}^{-1}$	$\nu_{\text{exp}} / \text{cm}^{-1}$
$\varepsilon+\tau+\pi$	320.8 (0.02)			
$\pi+\varepsilon+\tau$	321.4 (0.02)			
				366
			678.1 (m)	
			746.3	
ε	758.1 (1.00)	761.3 (1.00)	760.8 (s)	762
$\varepsilon+\tau$	799.9 (0.05)	811.4 (0.13)	812.4 (m)	812
	802.8 (0.05)			
γ	952.1 (0.01)	952.9 (0.03)	952.7 (w)	953
$\beta+\text{R}$	982.7 (0.16)	982.8 (0.21)	983.6 (w)	983
	983.0 (0.16)			
				993
				1010
				1179
				1246
				1392
			1421.0 (w)	1430
r	3048.6 (0.22)			
r	3049.0 (0.22)			

^aNotation used: R and r are CC and CH stretching modes, α and β are CCC and CCH in-plane bending modes, τ and ε are CCC and CCH out-of-plane vibrations, π is iron-ring movement, and γ is ring breathing mode.

^bFrequencies are scaled uniformly by scaling factors of 0.972 and 0.944 for mid-IR and C-H stretching modes, respectively. The integral intensity for the 758.1 band is 139.1 km/mol. Only modes with relative intensities equal to or larger than 0.01 are listed.

Table 3-5. Comparison of present work with previous band assignments for Fe(C₆H₆)₂ complex.

This work		Ball et al. ⁶²		Aleksanyan et al. ⁵⁸	Skobert et al. ⁵⁹
Mode	$\nu_{\text{cal}}^{\text{b}}/\text{cm}^{-1}$	$\nu_{\text{exp}}/\text{cm}^{-1}$	$\nu_{\text{exp}}/\text{cm}^{-1}$	$\nu_{\text{exp}}/\text{cm}^{-1}$	$\nu_{\text{exp}}/\text{cm}^{-1}$
$\pi+\varepsilon+\tau$	250.4 (0.71)			609	600
			664.1 (m)	685	
$\varepsilon+\tau$	708.1 (1.00)	715.9 (1.00)	715.7 (s)	709	715
				725	
				780	775
$\varepsilon+\tau$	826.9 (0.03)				
$\varepsilon+\tau$	828.9 (0.03)			859	855
				930	
γ	972.0 (0.26)	967.5 (0.38)	967.6 (w)	968	965
				978	
				989	
$\beta+\text{R}$	1008.7 (0.12)				
$\beta+\text{R}$	1008.9 (0.12)				
				1011	
				1035	
				1148	
				1175	1175
				1310	
				1412	
$\beta+\text{R}$	1442.8 (0.06)	1442.5 (0.27)	1441.0 (w)	1438	1435
	1443.4 (0.06)			1478	
r	3057.6 (0.36)				
r	3057.7 (0.36)				
r	3064.8 (0.08)				

^aNotation used: R and r are CC and CH stretching modes, α and β are CCC and CCH in-plane bending modes, τ and ε are CCC and CCH out-of-plane vibrations, π is iron-ring movement, and γ is ring breathing mode (out-of-phase).

^bFrequencies are scaled uniformly by scaling factors of 0.972 and 0.944 for mid-IR and CH stretching modes, respectively. The integral intensity for the 708.1 cm⁻¹ band is 127.1 91.4 km/mol. Only modes with relative intensities equal to or larger than 0.02 are listed.

Fe(naphthalene) complexes

Shown in Figure 3-5, the experimental IR spectra of iron co-deposited with naphthalene exhibit bands at 625.7, 732.3, 736.7, 821.5, 982.9, 1072.2, 1350.5, 1410.7 and 1462.9 cm^{-1} , of which the 1350.5 cm^{-1} band is the strongest. These bands all decreased upon photolysis and annealing, and are assigned here to the Fe(naphthalene) complex.

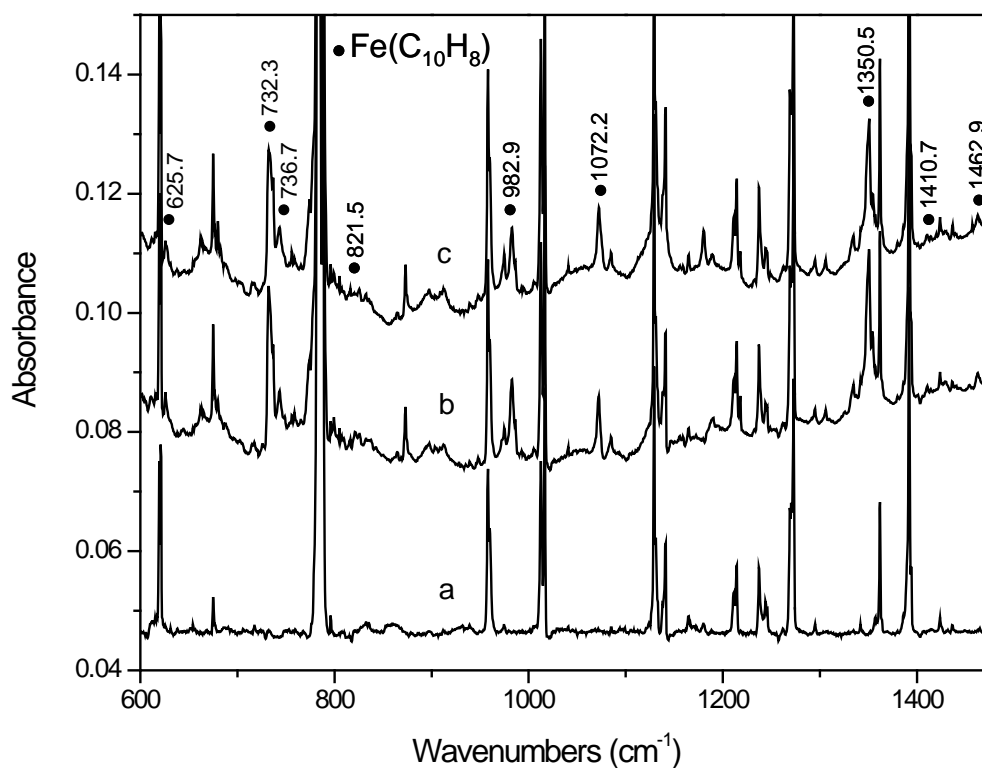


Figure 3-5. IR absorption spectrum of: naphthalene (C_{10}H_8) only (a), Fe codeposited with naphthalene (b), after matrix UV-visible photolysis (c), all in solid Ar at 12K. The star marked band at 873.1 cm^{-1} is unassigned.

Table 3-6 shows the comparison of the experimental data with calculated vibrational frequencies. Although the strongest absorption band predicted for the Fe(naphthalene) complex lies at 773.3 cm^{-1} , no band was observed here because of the strong absorption of naphthalene in

this region. The rest of the calculated bands for the triplet Fe(naphthalene) complex fit the experimental ones quite well. To confirm these assignments, isotopic substitution using naphthalene-d₈ was tried. The experimental IR spectra of iron codeposited with naphthalene-d₈ is compared to the calculated spectrum of triplet Fe(naphthalene-d₈) in Figure 3-6. The strongest band of the Fe(naphthalene-d₈) complex (at 618.5 cm⁻¹) is now observable. Its band position shows good agreement with the predicted one at 609.8 cm⁻¹.

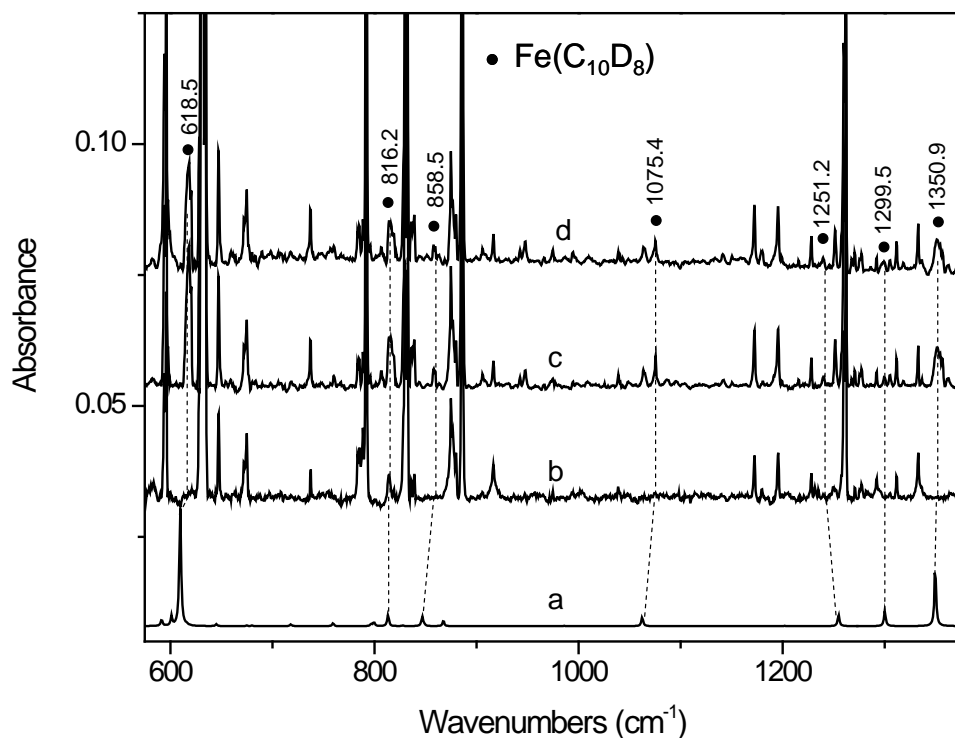


Figure 3-6. Calculated IR spectrum of Fe(C₁₀D₈) (a), experimental IR absorption spectrum of naphthalene-d₈ (C₁₀D₈) only (b), experimental IR absorption spectrum of Fe codeposited with naphthalene-d₈ (c), experimental IR absorption spectrum of Fe codeposited with naphthalene-d₈ after matrix UV-visible photolysis (d), all in solid Ar at 12 K.

In uncomplexed naphthalene, all the CH out-of-plane modes have similar energies and form a strong band at 773.3 cm⁻¹. When Fe is complexed to naphthalene, the degeneracy of those

CH out-of-plane modes is lifted and two different energy modes are observed, with an energy splitting of the 46.7 cm^{-1} (see Figure 3-7 and Table 3-6). The strongest one involves vibrations mainly on the ring closest to Fe and the second, lower energy mode involves vibrations mostly on the other ring. A similar, though higher energy, splitting of 70.3 cm^{-1} was found for similar modes in the cationic $\text{Fe}(\text{naphthalene})^+$ complex.⁷² Other modes in the mid-IR region of the $\text{Fe}(\text{naphthalene})$ spectrum have larger relative intensities compared to uncomplexed naphthalene. The intensity distribution in the CH stretching region (ca. 3050 cm^{-1}) in the $\text{Fe}(\text{naphthalene})$ spectrum is very similar to that in the naphthalene ligand, signifying little influence of the iron on these modes.

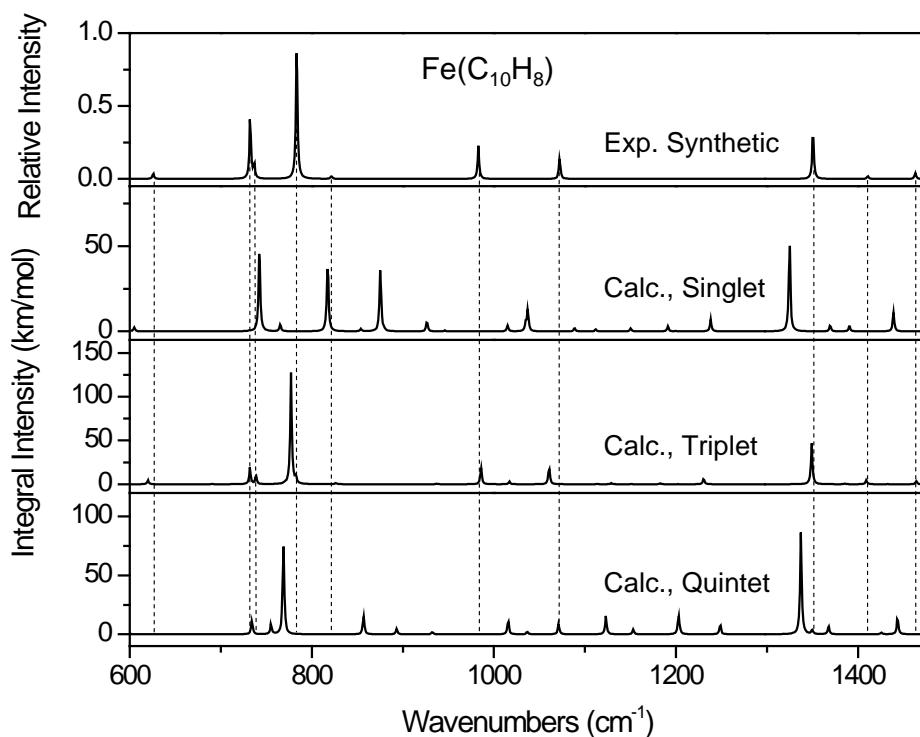


Figure 3-7. Synthetic experimental and calculated infrared absorption spectra with different spin multiplicities for the $\text{Fe}(\text{naphthalene})$ complex.

Table 3-6. IR absorption spectra of Fe(C₁₀H₈) and Fe(C₁₀D₈) iron(naphthalene) complexes.

Mode ^a	Fe(C ₁₀ H ₈)		Fe(C ₁₀ D ₈)	
	$\nu_{\text{cal}}^{\text{b}} / \text{cm}^{-1}$	$\nu_{\text{exp}} / \text{cm}^{-1}$	$\nu_{\text{cal}}^{\text{b}} / \text{cm}^{-1}$	$\nu_{\text{exp}} / \text{cm}^{-1}$
$\varepsilon+\tau+\pi$	252.5 (0.03)		240.0 (0.04)	
$\varepsilon+\tau+\pi$	309.6 (0.03)		289.4 (0.04)	
$\varepsilon+\tau+\pi$	330.2 (0.02)		311.8 (0.02)	
$\varepsilon+\tau+\pi$	382.4 (0.03)		347.1 (0.04)	
$\varepsilon+\tau+\pi$	457.9 (0.09)		400.7 (0.21)	
α	619.9 (0.04)	625.7 (0.04)	591.9 (0.06)	
$\varepsilon+\tau$	732.2 (0.14)	732.3 (0.44)	570.4 (0.02)	
$\varepsilon+\tau$			601.2 (0.08)	
$\varepsilon+\text{R}$	738.6 (0.08)	736.7 (0.10)		
ε	777.3 (1.00)	c	609.8 (1.00)	618.5 (1.00)
$\varepsilon+\tau$	782.5 (0.05)			
$\varepsilon+\tau$	826.4 (0.02)	821.5 (0.02)	644.7 (0.02)	
$\varepsilon+\tau$			759.3 (0.03)	
$\beta+\text{R}$	985.8 (0.14)	982.9 (0.23)	799.5 (0.03)	
$\beta+\text{R}$			813.2 (0.10)	816.2 (0.07)
$\beta+\text{R}$	1017.0 (0.02)			
$\beta+\text{R}$	1060.6 (0.15)	1072.2 (0.14)	846.8 (0.08)	858.5 (0.07)
$\beta+\text{R}$			867.5 (0.05)	
$\beta+\text{R}$			1062.4 (0.08)	1075.4 (0.04)
$\beta+\text{R}$	1230.4 (0.05)			
$\beta+\text{R}$	1349.1 (0.35)	1350.5 (0.35)	1254.7 (0.10)	1251.2 (0.11)
$\text{R}+\beta$	1409.1 (0.04)	1410.7 (0.02)	1300.2 (0.13)	1299.5 (0.03)
$\text{R}+\beta$			1349.5 (0.52)	1350.9 (0.41)
$\text{R}+\beta$	1463.9 (0.03)	1462.9 (0.04)	1377.1 (0.02)	
$\text{R}+\beta$			1423.0 (0.03)	
r	3047.4 (0.04)			
r	3062.4 (0.13)		2271.4 (0.25)	
r	3069.1 (0.21)		2267.4 (0.05)	
r	3077.2 (0.18)		2278.4 (0.08)	
r	3079.7 (0.12)		2283.5 (0.10)	

^a Notation used: R and r are CC and CH stretching modes, α and β are CCC and CCH in-plane bending modes, τ and ε are CCC and CCH out-of-plane vibrations, and π is iron-ring movement.

^b Frequencies are scaled uniformly by scaling factors of 0.972 and 0.952 for mid-IR and CH stretching modes, respectively. The integral intensity for the 758.1 and 582.8 cm⁻¹ bands are 131.3 and 78.8 km/mol, respectively. Only modes with relative intensities equal to or larger than 0.02 are listed.

^c No bands due to Fe(C₁₀H₈) are observed in the 775.4 – 791.8 cm⁻¹ region due to overlap by the strong band of neutral naphthalene at 783.4 cm⁻¹. The relative band integral intensities in experimental spectrum were scaled with the 1350.5 cm⁻¹ band intensity set to 0.35, a value equal to the calculated 1349.1 cm⁻¹ band intensity.

Our calculation shows that in the most stable structure for the Fe(naphthalene) complex the iron atom lies above one of the six-membered carbon rings, rather than centered above the whole molecule. This is also the case for the Fe(naphthalene)⁺ complex.⁷² The Fe(naphthalene) complex has C_s symmetry. Calculations also show that the triplet Fe(naphthalene) complex has the lowest energy. Since the experimental spectrum fits the calculated triplet spectrum the best (Figure 3-7), we conclude that the Fe(naphthalene) complex has a triplet ground state.

Fe(flourene) complexes

The experimental infrared spectra of iron codeposited with fluorene is compared with the calculated spectrum of triplet Fe(flourene) in Figure 3-8. The eight bands observed after deposition (at 718.0, 757.1, 776.5, 971.4, 1026.2, 1270.4, 1466.3 and 1509.1 cm⁻¹) all decreased after photolysis, in similar fashion, as noted above, for the mono complexes of Fe with benzene and naphthalene. The strongest band, observed at 776.5 cm⁻¹, is predicted to lie at 769.4 cm⁻¹.

Table 3-7, which compares the experimental data with the calculated vibrational frequencies, shows that good agreement is reached with the calculated triplet spectrum. Our calculations also show that 1) the iron atom in the Fe(flourene) complex resides 1.51 Å above one of the six-membered carbon rings, instead of above the middle five-membered one (and thus possesses C₁ symmetry), and 2) the Fe(flourene) complex with triplet multiplicity is the most stable (Table 3-1). For these reasons, we conclude that the Fe(flourene) complex is also a triplet, the same as the Fe(benzene) and Fe(naphthalene) complexes.

Table 3-7. IR absorption spectra of Fe(C₁₃H₁₀) iron(flourene) complex.

Mode ^a	v _{cal} ^b / cm ⁻¹	v _{exp} / cm ⁻¹	Mode ^a	v _{cal} ^b / cm ⁻¹	v _{exp} / cm ⁻¹
ε+τ+π	244.2 (0.07)		β+R	1220.8 (0.02)	
ε+τ+π	307.1 (0.06)		β+R	1273.5 (0.19)	1270.4 (0.19)
ε+τ+π	309.1 (0.05)		β+R	1296.2 (0.03)	
ε+τ+π	407.1 (0.04)		β+R	1351.8 (0.10)	

Table 3-7 Continued.

Mode ^a	$\nu_{\text{cal}}^{\text{b}} / \text{cm}^{-1}$	$\nu_{\text{exp}} / \text{cm}^{-1}$	Mode ^a	$\nu_{\text{cal}}^{\text{b}} / \text{cm}^{-1}$	$\nu_{\text{exp}} / \text{cm}^{-1}$
$\varepsilon+\tau+\pi$	421.8 (0.02)		$\beta+\text{R}$	1375.4 (0.03)	
$\varepsilon+\tau$	614.8 (0.03)		$\beta+\text{R}$	1393.2 (0.02)	
$\alpha+\beta$	618.6 (0.08)		$\beta+\text{R}$	1423.2 (0.05)	
$\varepsilon+\tau$	710.6 (0.20)	718.0 (0.29)	$\text{R}+\beta$	1447.1 (0.03)	
$\alpha+\beta$	732.4 (0.03)		$\beta+\text{R}$	1469.3 (0.12)	1466.3 (0.13)
$\varepsilon+\tau$	752.2 (0.83)	757.1 (0.98)	$\text{R}+\beta$	1499.5 (0.64)	1509.1 (0.54)
$\varepsilon+\tau$	769.4 (1.00)	776.5 (1.00)	$\text{R}+\beta$	1630.8 (0.36)	
$\varepsilon+\tau$	800.0 (0.06)		r	2898.6 (0.30)	
$\alpha+\beta$	822.4 (0.03)		r	2937.3 (0.09)	
$\varepsilon+\tau$	829.1 (0.05)		r	3040.1 (0.09)	
$\varepsilon+\tau$	942.3 (0.03)		r	3046.5 (0.05)	
$\text{R}+\beta$	970.7 (0.20)	971.4 (0.13)	r	3054.0 (0.07)	
$\text{R}+\beta$	992.0 (0.03)		r	3057.9 (0.21)	
$\beta+\text{R}$	1029.9 (0.11)	1026.2 (0.10)	r	3061.8 (0.25)	
$\beta+\text{R}$	1044.3 (0.14)		r	3069.3 (0.51)	
$\beta+\text{R}$	1096.0 (0.03)		r	3069.8 (0.07)	
$\text{R}+\beta$	1191.6 (0.03)		r	3069.8 (0.07)	

^aNotation used: R and r are CC and CH stretching modes, α and β are CCC and CCH in-plane bending modes, τ and ε are CCC and CCH out-of-plane vibrations, σ is HC(sp³)H out-of-plane bending mode, and π is iron-ring movement.

^bFrequencies are scaled uniformly by scaling factors of 0.972 and 0.949 for mid-IR and C-H stretching modes, respectively. The integral intensity for the 769.4 cm⁻¹ band is 80.9 km/mol. Only modes with relative intensities equal to or larger than 0.02 are listed.

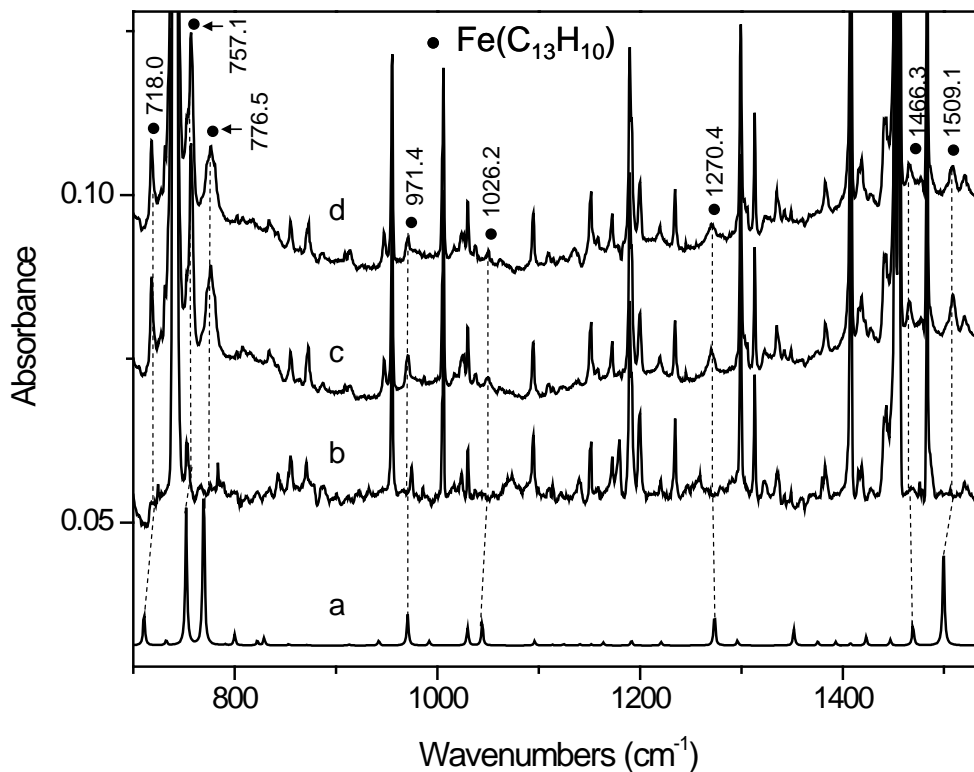


Figure 3-8. Calculated IR spectrum of $\text{Fe}(\text{C}_{13}\text{H}_{10})$ (a), experimental IR absorption spectrum of fluorene ($\text{C}_{13}\text{H}_{10}$) only (b), experimental IR absorption spectrum of Fe codeposited with fluorene (c), experimental IR absorption spectrum of Fe codeposited with fluorene after matrix UV-visible photolysis (d), all in solid Ar at 12K.

Fe(pyrene) complexes

The Fe(pyrene) complex has two possible isomers, with the optimized equilibrium structures **E** and **F** displayed in Figure 3-1. Structure **E** has the iron atom located above the carbon ring that shares four carbon atoms with other rings. In **F**, the iron atom sits above the carbon ring that shares three carbon atoms with other rings. Both structures have C_s symmetry.

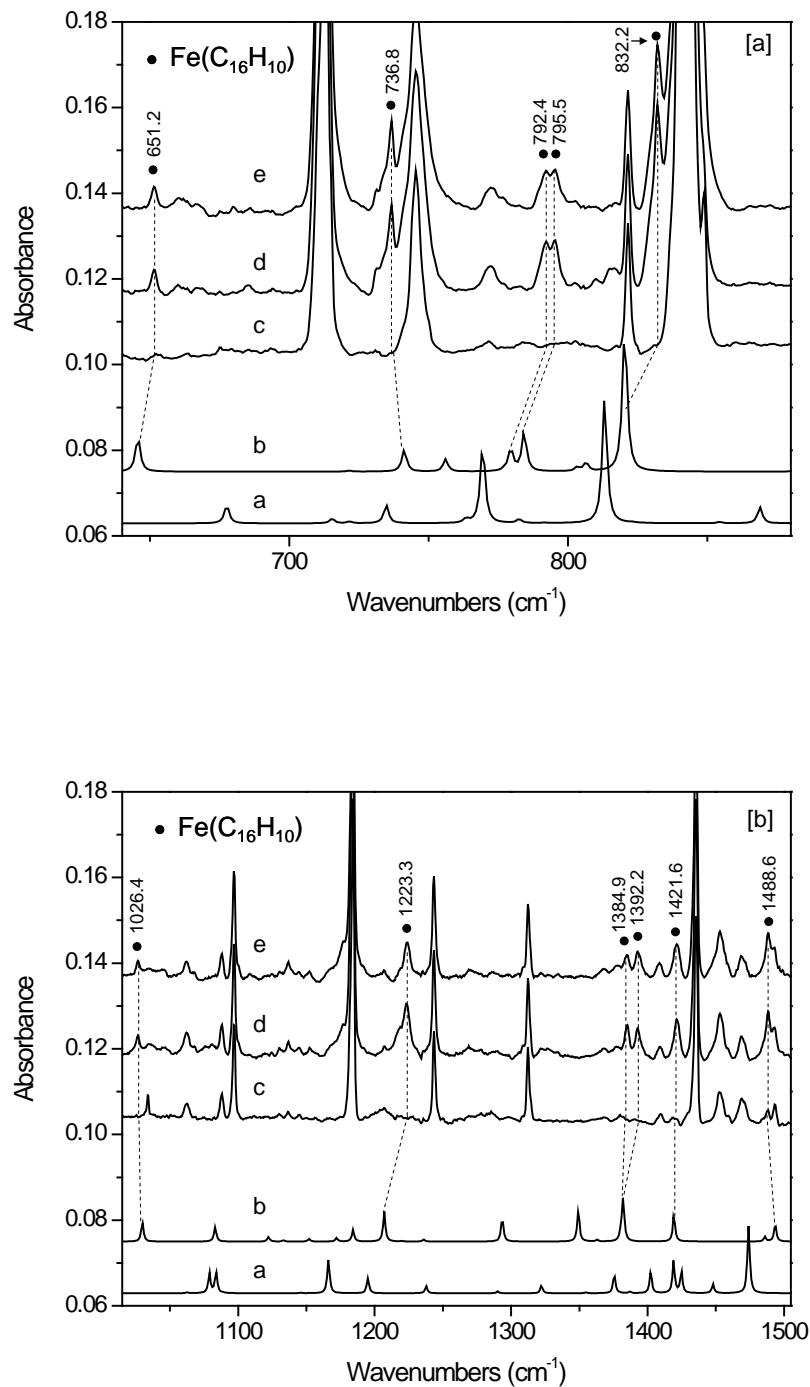


Figure 3-9. Calculated IR spectrum of $\text{Fe}(\text{C}_{16}\text{H}_{10})$ (structure **E**) (a), calculated IR spectrum of $\text{Fe}(\text{C}_{16}\text{H}_{10})$ (structure **F**) (b), experimental IR absorption spectrum of pyrene ($\text{C}_{16}\text{H}_{10}$) only (c), experimental IR absorption spectrum of Fe codeposited with pyrene (d), experimental IR absorption spectrum of Fe codeposited with pyrene after matrix UV-visible photolysis (e), all in solid Ar at 12K plotted in two energy regions [a] and [b].

Figure 3-9 shows two regions of the experimental IR spectra of iron codeposited with pyrene. The calculated spectra for the Fe(pyrene) **E** and **F** complexes are also given. Eleven bands were observed upon deposition, at 651.2, 736.8, 792.4, 795.5, 832.2, 1026.4, 1223.3, 1384.9, 1392.2, 1421.6 and 1488.6 cm^{-1} , with the strongest at 832.2 cm^{-1} . All these bands decreased with photolysis, and are here assigned to Fe(pyrene). While it is clear from Figure 3-9 that the calculated spectrum for isomer **E** fits the observed spectrum poorly, the experimental spectrum shows good agreement with the calculated triplet spectra for isomer **F**. Furthermore, **F** is more stable by 0.37eV than **E** (Table 3-1) and the observed frequencies compare favorably with the calculated vibrational frequencies for this isomer, as shown in Table 3-8. We therefore conclude that the most stable geometry for the Fe(pyrene) complex is structure **F** and that the complex has a triplet ground state.

In their work on the Fe-pyrene system, Elustondo and coworkers observed two sets of bands, at 790 and 831 cm^{-1} , and at 1221 and 1393 cm^{-1} .⁷¹ Their 790 cm^{-1} band probably corresponds to our 792.4 and 795.5 cm^{-1} bands, while their 831, 1221, 1393 cm^{-1} bands very likely are our 832.2, 1223.3, 1392.2 cm^{-1} bands, respectively. Elustondo attributed their bands to two different carriers on the basis of different annealing behavior.⁷¹ We have however found that all our bands decreased at similar rates with matrix photolysis and/or annealing. There is thus no indication from our work that these bands belong to two different carriers. Furthermore, according to our computational results in Table 3-8, all these bands can be assigned to the Fe(pyrene) complex. The band at 1966 cm^{-1} reported by Elustondo *et al.*⁷¹ was not observed in our work.

Table 3-8. IR absorption spectra of Fe(C₁₆H₁₀) iron(pyrene) complex (isomer **F** from Figure 3-1).

Mode ^a	$\nu_{\text{cal}}^{\text{b}} / \text{cm}^{-1}$	$\nu_{\text{exp}} / \text{cm}^{-1}$	Mode ^a	$\nu_{\text{cal}}^{\text{b}} / \text{cm}^{-1}$	$\nu_{\text{exp}} / \text{cm}^{-1}$
$\epsilon+\tau+\pi$	224.2 (0.08)		$\beta+\text{R}$	1122.1 (0.03)	
$\epsilon+\tau+\pi$	293.6 (0.03)		$\beta+\text{R}$	1172.1 (0.03)	

Table 3-8 Continued.

Mode ^a	$\nu_{\text{cal}}^{\text{b}} / \text{cm}^{-1}$	$\nu_{\text{exp}} / \text{cm}^{-1}$	Mode ^a	$\nu_{\text{cal}}^{\text{b}} / \text{cm}^{-1}$	$\nu_{\text{exp}} / \text{cm}^{-1}$
$\pi+\varepsilon+\tau$	318.3 (0.13)		$\beta+\text{R}$	1184.2 (0.08)	
α	340.5 (0.03)		$\text{R}+\beta$	1207.0 (0.21)	1223.3 (0.26)
$\alpha+\varepsilon+\tau$	412.1 (0.02)		$\text{R}+\beta$	1293.5 (0.17)	
$\varepsilon+\tau+\alpha$	468.1 (0.03)		$\text{R}+\beta$	1349.3 (0.22)	
$\alpha+\varepsilon+\tau$	496.6 (0.02)		$\text{R}+\beta$	1380.4 (0.06)	1384.9 (0.09)
$\varepsilon+\tau$	538.3 (0.03)		$\text{R}+\beta$	1382.2 (0.29)	1392.2 (0.10)
$\varepsilon+\tau$	645.4 (0.24)	651.2 (0.06)	$\text{R}+\beta$	1419.3 (0.19)	1421.6 (0.21)
$\varepsilon+\tau$	741.2 (0.15)	736.8 (0.11)	$\text{R}+\beta$	1486.0 (0.03)	
$\varepsilon+\tau$	756.1 (0.09)		$\text{R}+\beta$	1493.5 (0.13)	1488.6 (0.10)
$\varepsilon+\alpha+\beta$	779.6 (0.16)	792.4 (0.18)	$\text{R}+\beta$	1617.5 (0.04)	
$\varepsilon+\tau$	784.2 (0.27)	795.5 (0.18)	$\text{R}+\beta$	1619.7 (0.46)	
$\varepsilon+\tau$	803.4 (0.03)		r	3021.6 (0.03)	
$\alpha+\beta+\varepsilon$	806.5 (0.06)		r	3021.7 (0.02)	
$\varepsilon+\tau$	820.3 (1.00)	832.2 (1.00)	r	3033.6 (0.09)	
$\alpha+\beta$	972.8 (0.04)		r	3041.0 (0.56)	
$\beta+\text{R}$	1029.8 (0.13)	1026.4(0.12)	r	3049.5 (0.40)	
$\beta+\text{R}$	1083.1 (0.10)		r	3050.0 (0.06)	

^a Notation used: R and r are CC and CH stretching modes, α and β are CCC and CCH in-plane bending modes, τ and ε are CCC and CCH out-of-plane vibrations, π is iron-ring movement.

^b Frequencies are scaled uniformly by scaling factors of 0.972 and 0.944 for mid-IR and CH stretching modes, respectively. The integral intensity for the 820.3 band is 113.0 km/mol. Only modes with relative intensities equal to or larger than 0.02 are listed.

Fe(coronene) complexes

Figure 3-10 presents the experimental infrared spectra of iron codeposited with coronene along with the calculated spectrum for the triplet Fe(coronene) complex. Eight bands were observed after deposition, at 791.8, 815.7, 846.1, 1096.8, 1302.8, 1306.1, 1366.9 and 1438.9 cm^{-1} , with the strongest at 846.1 cm^{-1} . All bands decreased after UV photolysis, as found for the Fe(PAH) complexes described above, but at a greater rate. From Figure 3-10 it is clear that the photodissociation yield of Fe(coronene) complex is larger than for Fe(naphthalene), Fe(fluorene) or Fe(pyrene). The reason may be the significantly smaller binding energy for Fe(coronene) than for the other complexes: $D_0[\text{Fe}(\text{coronene})] = 0.52 \text{ eV}$, compared to the 1.91, 2.06, and 1.88 eV

for Fe(naphthalene), Fe(flourene), and Fe(pyrene), respectively (Table 3-1). The good agreement between the experimental and calculated band energies and intensities, shown in Figure 3-10 and Table 3-9, leads us to assign the above bands to the Fe(coronene) complex with a triplet electronic ground state.

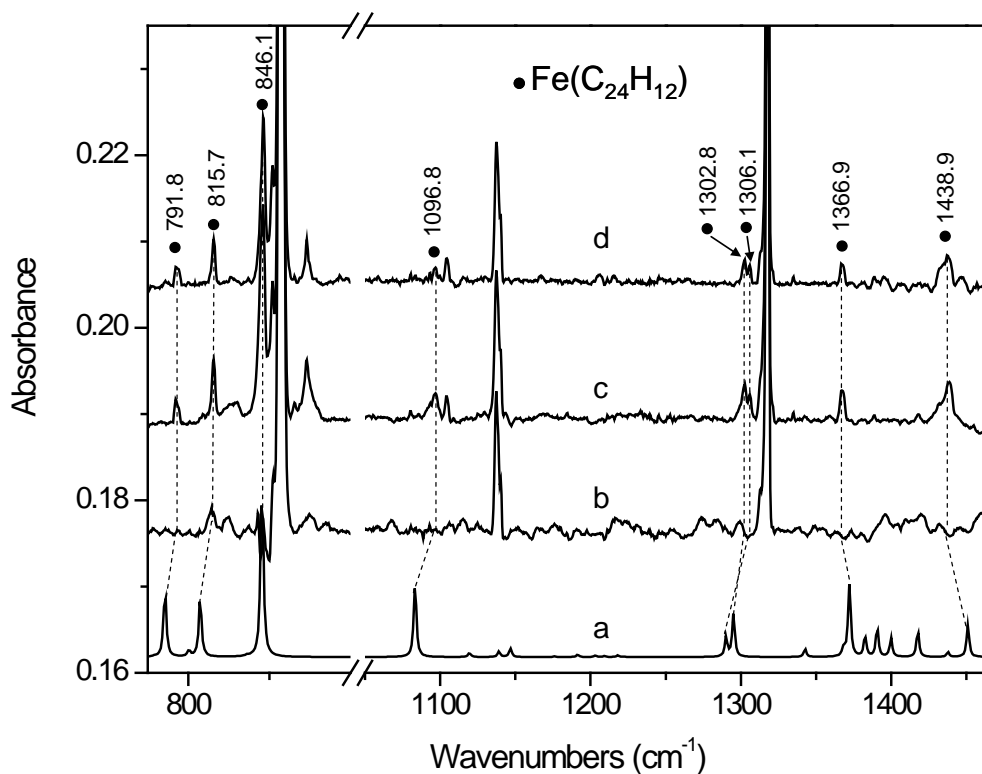


Figure 3-10. Calculated IR spectrum of Fe(C₂₄H₁₂) (a), experimental IR absorption spectrum of coronene (C₂₄H₁₂) only (b), experimental IR absorption spectrum of Fe codeposited with coronene (c), experimental IR absorption spectrum of Fe codeposited with coronene after matrix UV-visible photolysis (d), all in solid Ar at 12K.

Calculations also show that the iron sits over one of the outside carbon ring of the coronene, instead of the middle one, for C₁ symmetry. The iron-ring distance was calculated as 1.53 Å, very similar to the 1.55, 1.51, and 1.55 Å values found for the Fe(naphthalene), Fe(flourene) and Fe(pyrene) triplet complexes, respectively.

Table 3-9. IR absorption spectra of Fe(C₂₄H₁₂) iron (coronene) complex.

Mode ^a	$\nu_{\text{cal}}^{\text{b}} / \text{cm}^{-1}$	$\nu_{\text{exp}} / \text{cm}^{-1}$	Mode ^a	$\nu_{\text{cal}}^{\text{b}} / \text{cm}^{-1}$	$\nu_{\text{exp}} / \text{cm}^{-1}$
$\varepsilon+\tau+\pi$	112.2 (0.02)		R+ β	1295.1 (0.24)	1302.8 (0.11)
$\varepsilon+\tau+\pi$	196.8 (0.04)		R+ β	1342.7 (0.05)	
$\varepsilon+\tau+\pi$	308.4 (0.06)		R+ β	1368.4 (0.05)	
$\pi+\varepsilon+\tau$	342.1 (0.12)		R+ β	1372.2 (0.42)	1366.9 (0.15)
α	365.1 (0.04)		R+ β	1382.6 (0.12)	
α	368.8 (0.04)		R+ β	1390.6 (0.16)	
$\varepsilon+\tau+\alpha$	507.2 (0.11)		R+ β	1399.9 (0.11)	
$\varepsilon+\tau$	555.6 (0.04)		R+ β	1417.7 (0.15)	
$\varepsilon+\tau$	618.5 (0.08)		R+ β	1437.8 (0.03)	
$\varepsilon+\tau$	734.3 (0.04)		R+ β	1450.9 (0.17)	1438.9 (0.15)
$\varepsilon+\alpha+\tau$	753.1 (0.03)		R+ β	1467.6 (0.03)	
$\alpha+\beta+\varepsilon$	757.2 (0.05)		R+ β	1535.7 (0.05)	
$\varepsilon+\tau$	758.1 (0.02)		R+ β	1559.5 (0.04)	
$\varepsilon+\tau$	785.6 (0.38)	791.8 (0.15)	R+ β	1585.8 (0.12)	
$\varepsilon+\tau$	807.3 (0.33)	815.7 (0.17)	R+ β	1635.8 (0.04)	
$\varepsilon+\tau$	845.4 (1.00)	846.1(1.00)	r	3056.4 (0.02)	
R+ β	980.7 (0.03)		r	3057.7 (0.05)	
R+ β	1013.0 (0.07)		r	3058.5 (0.02)	
β +R	1083.3 (0.42)	1096.8 (0.15)	r	3074.4 (0.05)	
β +R	1119.4 (0.02)		r	3074.8 (0.11)	
β +R	1139.1 (0.03)		r	3075.3 (0.10)	
β +R	1146.8 (0.05)		r	3076.3 (0.76)	
R+ β	1290.1 (0.11)	1306.1 (0.07)	r	3077.0 (0.55)	

a) Notation used: R and r are CC and CH stretching modes, α and β are CCC and CCH in-plane bending modes, τ and ε are CCC and CCH out-of-plane vibrations, π is the iron-ring vibration.
b) Frequencies are scaled uniformly by scaling factors of 0.972 and 0.955 for mid-IR and CH stretching modes, respectively. The integral intensity for the 845.4 cm⁻¹ band is 114.4 km/mol, respectively.

Effect of complexation on IR spectra

Figure 3-11 gives a comparison of the calculated IR absorption spectra for the PAHs studied here, and their neutral and cationic complexes with iron. Comparing the Fe(PAH) to PAH spectra indicates that the CH out-of-plane bending modes (in the 800 cm⁻¹ (12.5 μm) energy region) are shifted to lower energy in the complex. The lone exception is the Fe(flourene) complex which contains a five-membered ring (for detailed band shifts, see Figure 3-8, 3-9 and

3-10). Presumably, the presence of Fe in the neutral Fe(PAH) complex induces a flatter CH out-of-plane bending mode potential which results in shifts in the low energy vibrations. The opposite is observed in the Fe(PAH)^+ complexes: the CH out-of-plane bending mode shifts to higher energy compared to the PAH^+ bands (Figure 3-11).⁷²

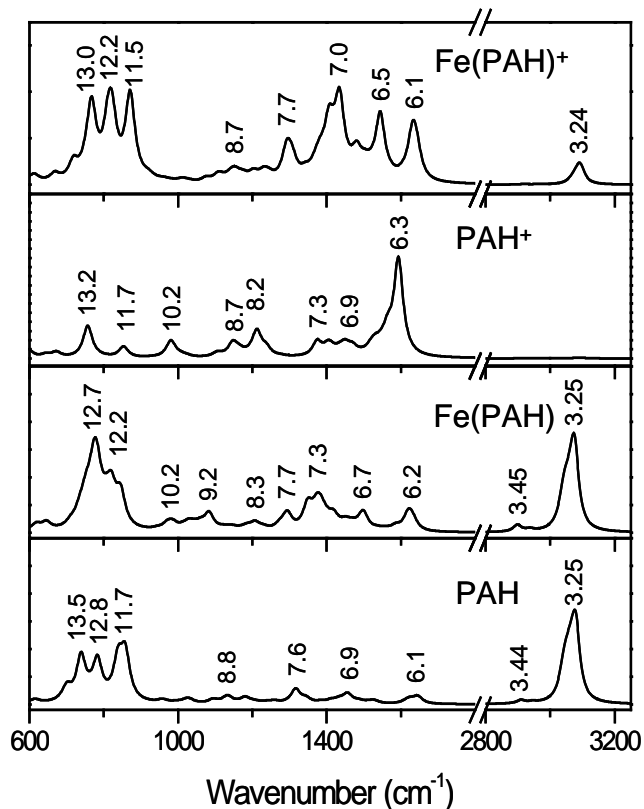


Figure 3-11. Comparison of summed IR absorption spectra calculated at the MPW1PW91/6-31+G(d,p) level for a 1:1:1:1 mixture of naphthalene, fluorene, pyrene and coronene (PAH panel), for their complexes with iron (Fe(PAH) panel), for similar mixture of cations (PAH^+ panel) and for their cationic complexes with iron (Fe(PAH)^+ panel). We note that the PAH , PAH^+ and Fe(PAH)^+ spectra are prepared at similar way to those of ref. 72,⁷² but for comparison purpose include also spectra of coronene, coronene⁺ and Fe(coronene)^+ .

In the mid-IR part of the Fe(PAH) spectrum, the highest energy CC stretching mode (6.2 μm) is shifted to still higher energy compared to the similar mode of the uncomplexed PAH

(Figure 3-11). Again, this is a reversed from what is found in the $\text{Fe}(\text{PAH})^+$ and PAH^+ systems. For the CH stretching modes ($3.25 \mu\text{m}$) essentially no changes were noted after complexation of the PAH with Fe.

In summary, as expected, there is a weaker interaction between neutral Fe and PAH ligands compared to the cationic complexes. This is manifest itself in smaller shifts in band positions and relative intensities in the $\text{Fe}(\text{PAH})$ complex IR spectra.

Summary

In this chapter the experimental infrared spectra for $\text{Fe}(\text{benzene})$, $\text{Fe}(\text{benzene})_2$, $\text{Fe}(\text{naphthalene})$, $\text{Fe}(\text{fluorene})$, $\text{Fe}(\text{pyrene})$ and $\text{Fe}(\text{coronene})$ complexes have been obtained. The spectral features showed good agreement with the harmonic vibrational frequencies calculated from density functional electronic structure calculations at the MPW1PW91/6-31+G(d, p) level. The energy calculations and the comparison of experimental with calculated spectra reveal that the most stable structures for these complexes are triplets. The binding energies for these complexes decrease with increasing PAH size which is opposite to that observed previously for the $\text{Fe}(\text{PAH})^+$ cationic complexes.⁷² Equilibrium geometry calculations show that the iron atom always sits over one of the six-membered carbon rings in the complex, closer to the naphthalene, fluorene, pyrene and coronene ligands by 0.12, 0.17, 0.17, and 0.19 Å, respectively, when compared to similar iron-ring distances in the respective cationic complexes.⁷² The estimated dissociation energies for the neutral $\text{Fe}(\text{PAH})$ complexes of $\text{Fe}(\text{naphthalene})$, $\text{Fe}(\text{fluorene})$, $\text{Fe}(\text{pyrene})$ and $\text{Fe}(\text{coronene})$ are lower than their cationic quartet spin state counterparts by 0.84, 0.82, 0.92 and 2.35 eV, respectively.⁷² Since the IR spectra of $\text{Fe}(\text{PAH})$ complexes display only small band shifts and intensity changes when compared to PAH free ligands, it is possible that they could contribute to the UIR broad bands at 3.3, 6.3, 7.8+8.6, 11.3, and 12.7 μm , as the PAHs do.¹⁹ However, because of the low dissociation energies of the $\text{Fe}(\text{PAH})$ complexes, it is

considered unlikely that these complexes would survive in the harsh environment of ISM. Their contribution to UIR bands is thus expected to be minimal or nonexistent.

CHAPTER 4 COPPER-CARBON CLUSTERS: STRUCTURE, INFRARED FREQUENCIES AND ISOTOPIC SCRAMBLING

Introduction

Transition metals may be important components in the chemistry of the interstellar medium. Iron, with its high nuclear stability, is the most abundant metal in interstellar space, but despite its abundance, it is known to be depleted about 100-fold compared to our solar system. Complexation of iron with polycyclic aromatic hydrocarbons (PAHs) and/or carbon clusters has been proposed as the reason for this depletion.^{51-53,72} Other transition metals are also present in the interstellar medium, although at lower concentrations.^{42,53} Their participation in interstellar chemistry is largely unknown, primarily because of a dearth of information on their spectral properties. However, recent studies by Graham and Rittby and coworkers on the infrared spectroscopy of matrix-isolated transition metal-C₃ clusters, such as linear GeC₃Ge, fanlike TiC₃, linear CrC₃ and CoC₃, and floppy NiC₃Ni have begun to provide some of this much-needed information.⁷⁹⁻⁸³

Using satellite-based measurements, Jenkins, Savage, and Spitzer analyzed Cu⁺ ion column densities along various lines of sight for early-type stars, and found a substantial depletion of Cu⁺ compared to our solar system.⁵³ Laboratory studies of copper reactivity with interstellar molecules such as carbon clusters are therefore important initial steps in understanding its interstellar chemistry. In this paper we report our laboratory study on the formation of Cu-carbon clusters, and present evidence for the existence of CuC₃.

Previous laboratory work on copper-carbon clusters has been limited. Cationic CuC_n⁺ clusters (n = 1-3), generated in spark discharges of Cu and graphite, have been observed in mass spectrometric studies.⁸⁴ Copper acetylide (CuC≡CCu) has been formed by the reaction of acetylenic compounds with copper salts in liquid ammonia⁸⁵, and is widely used as a catalyst in

the production of copper powder.⁸⁶ Other CuC_n compounds, including copper acetylide, have been observed in oxyacetylene/ hydrogen/ copper flames.⁸⁷ Time-of-flight mass spectrometric studies of Cu-C metallo-carbohedrenes (“met-cars”) identified the clusters Cu_nC_2^+ ($n = 2k+1$, $k = 1 - 7$) and Cu_nC_4^+ ($n = 2k+1$, $k = 2 - 4$) and speculated on their possible structures.⁸⁸

In this chapter we report on a matrix-isolation infrared spectroscopic study of laser-ablated Cu-carbon clusters and corresponding theoretical work on small stable copper-carbon systems, Cu_mC_n ($m = 1, 2$; $n = 1, 2, 3$). The equilibrium geometries, vibrational harmonic frequencies, and stabilities for these clusters have been calculated using density functional theory. When compared with our experimental data these results show that only the CuC_3 cluster was observed in our experiments. Photo-induced $^{12/13}\text{C}$ -isotopic scrambling in $\text{Cu}^{12/13}\text{C}_3$ isotopomers has also been observed and is proposed to occur via a bicyclic CuC_3 intermediate.

Computational and Experimental Details

Experimental methods

The experimental apparatus used for the generation and trapping of copper-carbon clusters in solid Ar is presented in chapter 2 and shown in Figure 2-3. Briefly, the output from a pulsed Nd-YAG laser (1064/532 nm, 0.2 – 0.5W, 10Hz) was split into two beams, with one beam (intensity ca. 60%) directed by prism P1 and focused by lens L1 to a ~ 0.5 mm diameter spot on a piece of Cu metal (SPEX, natural abundance: ^{63}Cu (69.2%) and ^{65}Cu (30.8%)). The second beam (intensity ca. 40%) was focused to a 2 – 3 mm diameter spot on a pressed pellet of ^{12}C and ^{13}C (ISOTECH). The Cu and C samples, *ca.* 4 – 5 mm apart, were positioned close to the CsI sample window. By rotating the glass plate beam splitter, the ratio of the intensity of the reflected beam to the intensity of the transmitted beam could easily be changed. With a ~ 80° angle of incidence, the intensities of the reflected and transmitted beams are equal, as expected from the Fresnel formula.⁴⁸ Both L1 and L2 lenses were mounted on micrometer screw-driven

mounts which allowed for periodic re-positioning of the focused laser beams onto fresh regions of the carbon and copper samples.

Infrared spectra were scanned using a NICOLET Magna 560 FT-IR spectrometer (0.5 cm^{-1} resolution) after a 2 – 3 hrs deposition of the Cu/C_n/Ar mixture on a CsI sample window held at 12K by a closed-cycle helium cryostat (APD Displex). Annealing to 35K followed by recooling to 12K, as well as photolysis with a medium pressure 100W Hg lamp, were used as needed to induce secondary reactions.

Computational methods

Calculation of molecular equilibrium geometries and associated vibrational harmonic mode frequencies and dissociation energies were calculated using density functional theory with the Gaussian 03 program package⁷³ using Becke's three-parameter hybrid functional combined with the non-local correction functional of Lee, Yang, and Parr (B3LYP)⁸⁹ and a 6-311++G (3df) basis set which contains three sets of d functions and one set of f functions.

For systems containing transition metals, the B3LYP functional has been shown to occasionally predict incorrect equilibrium geometries, as determined by a comparison of experimental and calculated vibrational spectra.^{76,90-92} So, in addition, we used the MPW1PW91 functional, a modified Perdew-Wang exchange and correlation functional, along with a 6-311++G(3df) basis set to verify the B3LYP optimized structure.^{74,75} This approach has been recommended by Wiberg,⁹⁰ Dunbar,⁹¹ and Oomens et al.⁷⁶ in their studies of C-, H-, and metal-containing systems. The MPW1PW91 functional was used in our recent studies of iron complexed with cationic and neutral polycyclic aromatic hydrocarbons.^{72,92}

We also tested the BPW91 functional (on the near-linear CuC₃ cluster) by using the 6-311++G(3df) basis set for the carbons and SDD pseudopotential for copper. Such a functional

has been recommended for copper, silver and gold⁹³ and has been used in calculations of various reaction products of these metals with hydrogen.⁹⁴

From our $^{63}\text{Cu}^{12/13}\text{C}_3$ isotopomer frequency calculations (BPW91/6-311++G(3df) [carbons]/SDD pseudopotential [Cu]), we find the maximum difference (after scaling) between predicted and observed vibrational frequencies is large, 7.3 cm^{-1} , but this value drops to 2.4 cm^{-1} when the MPW1PW91 functional is used with the same basis sets. Finally, when the MPW1PW91 functional and the 6-311++G(3df) basis set is used for all atoms, this maximum difference drops to 1.6 cm^{-1} , an acceptable value for ^{13}C - labeling assignments.

The potential energy surface of the isomerization reaction for the near linear CuC_3 cluster was plotted using the MPW1PW91/6-311++G (3df) level of theory exclusively. The transition state (TS) identified from this plot was verified using traditional transition state optimization with the Berny optimization algorithm, as incorporated in the Gaussian 03 package.⁷³

Experimental Infrared Spectra

Figure 4-1 displays the infrared absorption spectra in the $1200\text{-}1260\text{ cm}^{-1}$ and $1750\text{-}2200\text{ cm}^{-1}$ ranges for species formed by the laser ablation of graphite (spectrum a) and by the synchronized dual laser ablation of copper and graphite (spectrum b). The majority of bands in spectrum a have previously been assigned to various neutral carbon clusters ($\text{C}_3 - \text{C}_{12}$) by us and others.^{95,96} Several bands in spectrum b, not due to neutral carbon clusters, such as the anionic clusters, C_5^- (1831.8 cm^{-1})⁹⁷ and C_6^- (1936.5 cm^{-1})^{97,98} are also present; the C_5^- band is very weak and masked by the shoulder of the strong 1830.0 cm^{-1} band and is therefore not marked in the figure. Also present are impurities such as CO and H_2O , which are known to be more abundant when high laser ablation powers are used.⁸¹ Additional reaction products are also seen, namely, CuCO (2009.5 cm^{-1})⁹⁹ and C_3H (1824.4 cm^{-1}).^{100,101}

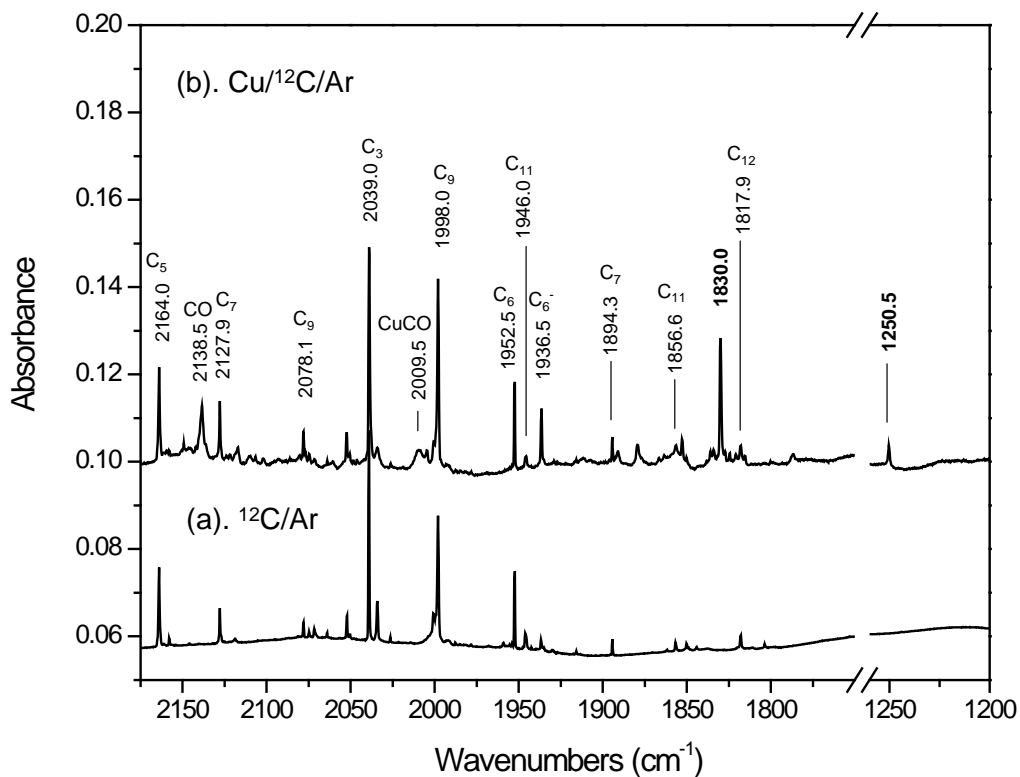


Figure 4-1. Infrared absorption spectra of products of laser ablation of graphite (^{12}C (99%) + ^{13}C (1%)) (spectrum a) and products of two-beam laser ablation of graphite and copper (spectrum b, enlarged twofold). The spectra were recorded after matrix annealing to 35 K then cooling back to 12 K. The major bands due to pure carbon clusters and their reaction products with copper at 1830 and 1250.5 cm^{-1} are indicated. Carbon monoxide and its product with copper are also marked.

Two new bands in spectrum b at 1830.0 and 1250.5 cm^{-1} , not found in spectrum a, were found to be dependent on both copper and carbon concentrations. To determine whether these two bands belong to the same species, a large number of experiments were performed under different experimental conditions, for example, different Cu/C concentration ratios (using different ablating laser beam intensities), matrix annealing up to 35K and, finally, UV-visible photolysis (up to 1 hr). We found that the ratio of the integral intensities of the 1830 and 1250.5

cm⁻¹ bands is constant under these different conditions (and $\cong 5.7 \pm 0.3$), supporting the conclusion that both bands arise from a common carrier.

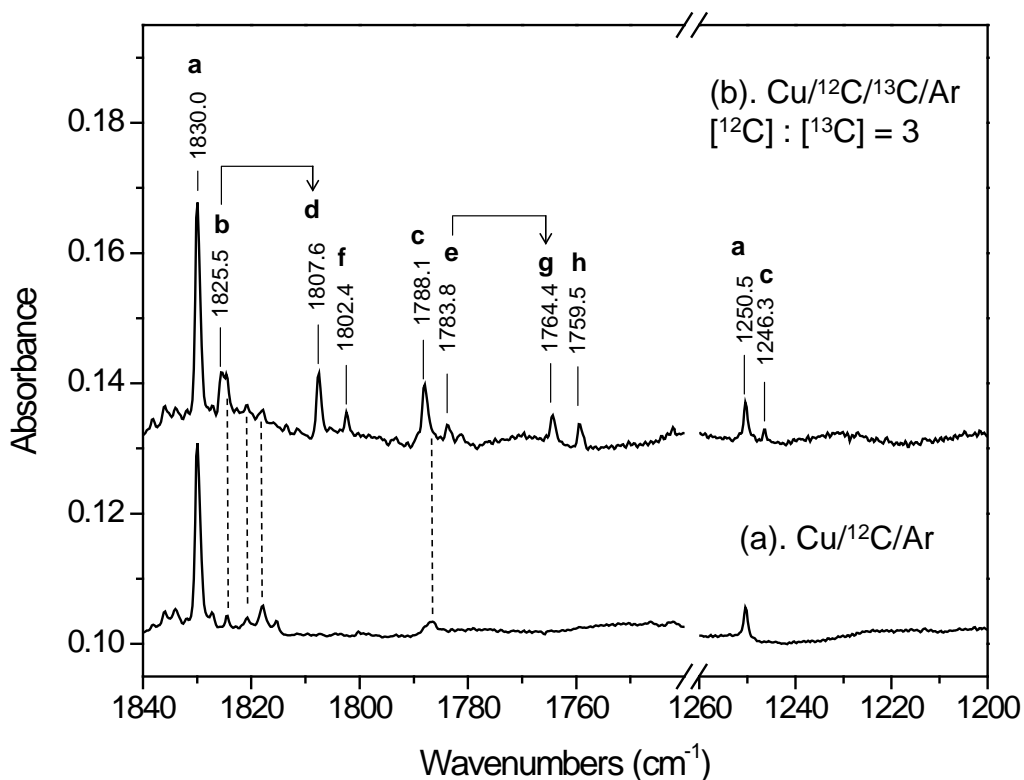


Figure 4-2. Infrared spectra of reaction products from laser ablation of Cu and ¹²C (spectrum a) displayed in two energy regions. The bands at 1830.0 and 1250.5 cm⁻¹ are due to a common carrier containing Cu and ¹²C. Spectrum b was collected from runs similar to spectrum a, but with a ¹³C-enriched sample. The band carriers marked by vertical dashed lines are due to: C₃H (1824.4 cm⁻¹),^{100,101} C₂H⁺ (1820.2 cm⁻¹),¹⁰² and C₁₂ (1817.9 cm⁻¹).¹⁰³ The fractionations of **b** → **d** as well as of **e** → **g** isotopomers *via* the proposed ^{12/13}C isotopic scrambling in *nl*-Cu^{12/13}C₃ (see text) are marked.

The results of isotopic (¹³C) substitution are shown in Figure 4-2 (top panel, spectrum b). Inspection of the ¹³C- labeled spectrum built on the 1830 cm⁻¹ band reveals eight isotopomeric bands, (**a-h**). A very similar isotopomer band pattern was previously observed for near-linear ^{12/13}C₃•H₂O complexes¹⁰⁴ and linear ^{12/13}C₃Cr⁸³ and ^{12/13}C₃Co⁸¹ clusters. Such a band pattern is

characteristic of the CC asymmetric stretching mode in linear or near-linear $^{12/13}\text{C}_3$ with one end bonded to a ligand. In the next section, we explore whether linear or near-linear CuC_3 clusters can account for these results.

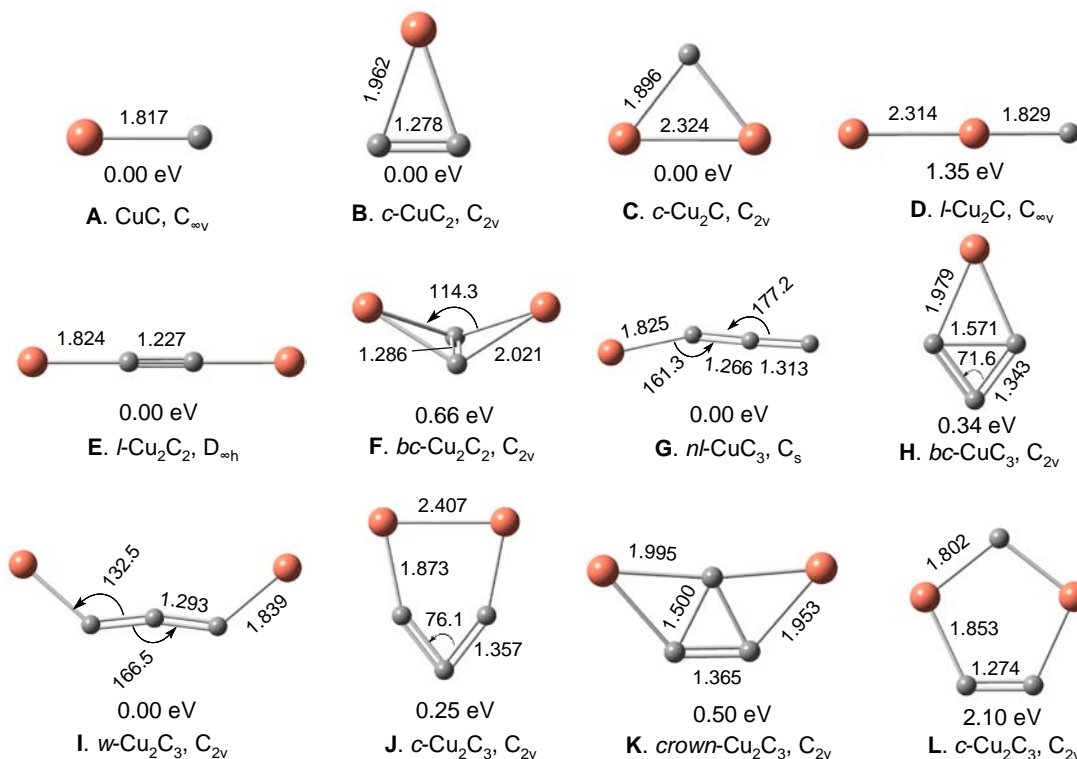


Figure 4-3. Optimized equilibrium structures for the CuC , CuC_2 , Cu_2C , Cu_2C_2 , Cu_3 , and Cu_2C_3 clusters. The bond lengths (Å) and angles (°) calculated at B3LYP/6-311++G(3df) (italic type, top) and at MPW1PW91/6-311++G(3df) (normal type) are marked. The relative isomer energies are indicated.

Equilibrium geometries and vibrations for the Cu_mC_n ($m=1,2, n=1, 2, 3$) clusters

Previous IR studies have identified metal-carbon clusters of the type MC_3 and MC_3M ($M =$ transition metal atom).⁷⁹⁻⁸³ Here we explore such clusters theoretically for $M = \text{Cu}$, and, in addition, explore the smaller MC , MC_2 , and MC_2M species. Figure 4-3 shows the stable equilibrium geometries found for the Cu_mC_n clusters ($m = 1, 2; n = 1, 2, 3$) with displayed geometry and energy parameters predicted by MPW1PW91 and B3LYP functionals. Predicted

harmonic vibrational frequencies and intensities are collected in Table 4-1. Total energies

(corrected for zero point vibrational energies) and dissociation energies are given in Table 4-2.

Table 4-1. Vibrational frequencies (cm^{-1}) and integral intensities (km/mol) for electronic ground states of Cu_mC_n ($m = 1, 2; n = 1, 2, 3$) clusters (displayed in Figure 4-3), calculated using B3LYP and MPW1PW91 functionals.

Cu_mC_n Isomer	B3LYP/6-311++G(3df)	MPW1PW91/6-311++G(3df)
A. CuC ($X^4\Sigma$)	σ 572.5 (10)	σ 585.6 (14)
B. <i>c</i> -CuC ₂ (X^2A_1)	a_1 1750.3 (7), a_1 436.4 (5), b_2 291.1(0)	a_1 1768.7 (5), a_1 449.3 (5), b_2 321.9 (0)
C. <i>c</i> -Cu ₂ C (X^3A_2)	a_1 528.3 (6), b_2 389.7 (5), a_1 210.2 (1)	a_1 534.1 (6), b_2 392.4 (7), a_1 218.9 (1)
D. <i>l</i> -Cu ₂ C ($X^3\Sigma_g$)	σ 665.0 (7), π 240.3 (2x26), σ 232.7 (5)	σ 574.5 (0), π 509.1 (474), σ 210.1 (1) , π 67.3 (0)
E. <i>l</i> -Cu ₂ C ₂ ($X^1\Sigma_g$)	σ_g 2093.1 (0), σ_u 659.3 (61), π_g 255.7 (2x0), σ_g 254.9 (0), π_u 98.2 (2x50)	σ_g 2112.0 (0), σ_u 662.2 (65), π_g 260.5 (2x0), σ_g 257.5 (0), π_u 98.4 (2x56)
F. <i>bc</i> -Cu ₂ C ₂ (X^1A_1)	a_1 1703.4 (10), b_2 497.2 (17), a_1 313.2 (21), a_2 140.1 (0), b_1 133.4 (9), a_1 57.8 (14)	a_1 1713.8 (8), b_2 518.3 (23), a_1 324.9 (23), a_2 201.9 (0), b_1 166.1 (10), a_1 51.1 (16)
G. <i>nl</i> -CuC ₃ (X^2A')	a' 1901.0 (134), a' 1272.6 (9), a' 453.6 (21), a' 364.3 (23), a'' 228.4 (9), a' 118.8 (15)	a' 1900.5 (172), a' 1281.5 (31), a' 432.0 (2), a'' 363.3 (28), a'' 227.5 (10), a'' 84.5 (17)
H. <i>bc</i> -CuC ₃ (X^2A_1)	a_1 1595.8 (25), b_2 1208.2 (19), a_1 634.5(22), a_1 351.6 (13), b_1 241.5(7), b_2 189.7 (2)	a_1 1618.3 (13), b_2 1221.9 (21), a_1 729.5 (5), a_1 372.2 (12), b_1 240.1(7), b_2 220.2 (1)
I. <i>w</i> -Cu ₂ C ₃ (X^1A_1)	b_2 1776.1 (404), a_1 1299.8 (9), a_1 567.2 (3), b_2 536.0 (35), a_1 314.8 (7), b_1 272.9 (3), a_2 241.6 (0), b_2 105.5 (135), a_1 50.2 (7)	b_2 1776.4 (437), a_1 1313.1 (7), a_1 570.3 (2), b_2 548.6 (21), a_1 322.9 (11), b_1 275.6 (4), a_2 240.4 (0), b_2 87.8 (137), a_1 47.5 (8)
J. <i>c</i> -Cu ₂ C ₃ (X^1A_1)	a_1 1488.7 (601), b_2 1287.2 (5), a_1 447.1 (26), b_2 413.2 (18), a_1 381.0 (112), b_1 356.0 (5), a_2 190.0 (0), a_1 186.7(6), b_2 168.6 (18)	a_1 1521.2 (552), b_2 1267.8 (11), a_1 469.9 (126), a_1 457.6 (136), b_2 411.5 (8), b_1 348.3 (6), a_2 198.5 (0), a_1 171.8 (15), b_2 144.8 (23)
K. <i>crown</i> - Cu ₂ C ₃ (X^1A_1)	a_1 1471.1 (26), a_1 842.9 (134), b_2 725.9(37), b_2 390.1 (55), a_1 300.6 (9), a_2 258.8 (0), b_2 221.6 (0), b_2 179.8 (18), a_1 90.3 (2)	a_1 1498.4 (11), a_1 906.8 (127), b_2 804.3(3), b_2 425.1 (42), a_1 319.4 (14), b_2 258.3 (0), a_2 256.8 (0), b_1 176.4 (17), a_1 97.2 (2)
L. <i>c</i> -Cu ₂ C ₃ (X^1A_1)	a_1 1748.1 (87), b_2 638.3 (2), a_1 592.8 (9), a_1 545.4 (20), b_2 539.9 (2), a_2 239.6 (0), b_1 210.3 (23), a_1 129.9 (1), b_2 109.7 (44)	a_1 1766.6 (90), b_2 658.9(2), a_1 605.6 (10), a_1 559.1 (21), b_2 557.6 (3), a_2 228.0 (0), b_1 206.4 (26), a_1 120.6 (1), b_2 70.2 (46)

Table 4-2. Calculated total energies, E_{ZPE} (Hartrees), corrected for zero point vibrational energies, and estimated dissociation energies, D_0 (eV) or isomerization energy barriers, E_{Iso} (eV) for Cu_mC_n ($n = 1, 2; m = 1, 2, 3$) isomers.

Cu_mC_n	B3LYP/6-311++G(3df)	MPW1PW91/6-311++G(3df)
A. CuC ($X^4\Sigma$)	$E_{ZPE} = -1678.402\ 951$ $D_0(\text{Cu}(X^2S_{1/2}) + C(X^3P)) = 1.99\ \text{eV}$	$E_{ZPE} = -1678.468\ 587$ $D_0(\text{Cu}(X^2S_{1/2}) + C(X^3P)) = 2.20\ \text{eV}$
B. <i>c</i> -CuC ₂ (X^2A_1)	$E_{ZPE} = -1716.545\ 045$ $D_0(\text{Cu}(X^2S_{1/2}) + C_2(X^1\Sigma_g^+)) = 2 \times 2.33\ \text{eV}$	$E_{ZPE} = -1716.594\ 551$ $D_0(\text{Cu}(X^2S_{1/2}) + C_2(X^1\Sigma_g^+)) = 2 \times 2.47\ \text{eV}$
C. <i>c</i> -Cu ₂ C (X^3A_2)	$E_{ZPE} = -3318.959\ 383$ $D_0(\text{Cu}(X^2S_{1/2}) + \text{CuC}(X^4\Sigma)) = 2.29\ \text{eV}$	$E_{ZPE} = -3319.095\ 577$ $D_0(\text{Cu}(X^2S_{1/2}) + \text{CuC}(X^4\Sigma)) = 2.21\ \text{eV}$
D. <i>l</i> -Cu ₂ C ($X^3\Sigma_g$)	$E_{ZPE} = -3318.885\ 540$ $D_0(\text{Cu}(X^2S_{1/2}) + \text{CuC}(X^4\Sigma)) = 0.28\ \text{eV}$	$E_{ZPE} = -3319.045\ 993$ $D_0(\text{Cu}(X^2S_{1/2}) + \text{CuC}(X^4\Sigma)) = 0.86\ \text{eV}$
E. <i>l</i> -Cu ₂ C ₂ ($X^1\Sigma_g$)	$E_{ZPE} = -3357.146\ 742$ $D_0(2\text{Cu}(X^2S_{1/2}) + C_2(X^1\Sigma_g^+)) = 2 \times 4.09\ \text{eV}$	$E_{ZPE} = -3357.269\ 606$ $D_0(2\text{Cu}(X^2S_{1/2}) + C_2(X^1\Sigma_g^+)) = 2 \times 4.23\ \text{eV}$
F. <i>bc</i> -Cu ₂ C ₂ (X^1A_1)	$E_{ZPE} = -3357.117\ 387$ $D_0(2\text{Cu}(X^2S_{1/2}) + C_2(X^1\Sigma_g^+)) = 4 \times 1.85\ \text{eV}$	$E_{ZPE} = -3357.245\ 412$ $D_0(2\text{Cu}(X^2S_{1/2}) + C_2(X^1\Sigma_g^+)) = 4 \times 1.95\ \text{eV}$
G. <i>nl</i> -CuC ₃ (X^2A')	$E_{ZPE} = -1754.623\ 580$ $D_0(\text{Cu}(X^2S_{1/2}) + C_3(X^1\Sigma_g^+)) = 2.07\ \text{eV}$	$E_{ZPE} = -1754.655\ 782$ $D_0(\text{Cu}(X^2S_{1/2}) + C_3(X^1\Sigma_g^+)) = 2.26\ \text{eV}$
H. <i>bc</i> -CuC ₃ (X^2A_1)	$E_{ZPE} = -1754.600\ 074$ $E_{Iso}(bc\text{-CuC}_3(X^2A_1) \rightarrow nl\text{-CuC}_3(X^2A')) = 0.59\ \text{eV}^a$	$E_{ZPE} = -1754.643\ 139$ $E_{Iso}(bc\text{-CuC}_3(X^2A_1) \rightarrow nl\text{-CuC}_3(X^2A')) = 0.91\ \text{eV}^b$
I. <i>w</i> -Cu ₂ C ₃ (X^1A_1)	$E_{ZPE} = -3395.164\ 221$ $D_0(\text{Cu}(X^2S_{1/2}) + nl\text{-CuC}_3(X^2A')) = 1.86\ \text{eV}$	$E_{ZPE} = -3395.269\ 749$ $D_0(\text{Cu}(X^2S_{1/2}) + nl\text{-CuC}_3(X^2A')) = 1.85\ \text{eV}$
J. <i>c</i> -Cu ₂ C ₃ (X^1A_1)	$E_{ZPE} = -3395.145\ 764$ $D_0(\text{Cu}(X^2S_{1/2}) + bc\text{-CuC}_3(X^2A_1)) = 2.00\ \text{eV}$	$E_{ZPE} = -3395.260\ 406$ $D_0(\text{Cu}(X^2S_{1/2}) + bc\text{-CuC}_3(X^2A_1)) = 1.94\ \text{eV}$
K. <i>crown</i> -Cu ₂ C ₃ (X^1A_1)	$E_{ZPE} = -3395.127\ 280$ $D_0(\text{Cu}(X^2S_{1/2}) + bc\text{-CuC}_3(X^2A_1)) = 1.50\ \text{eV}$	$E_{ZPE} = -3395.251\ 558$ $D_0(\text{Cu}(X^2S_{1/2}) + bc\text{-CuC}_3(X^2A_1)) = 1.70\ \text{eV}$
L. <i>c</i> -Cu ₂ C ₃ (X^1A_1)	$E_{ZPE} = -3395.085\ 801$ $D_0(c\text{-Cu}_2\text{C}(X^3A_2) + C_2(X^1\Sigma_g^+)) = 2 \times 3.06\ \text{eV}$	$E_{ZPE} = -3395.193\ 157$ $D_0(c\text{-Cu}_2\text{C}(X^3A_2) + C_2(X^1\Sigma_g^+)) = 2 \times 3.14\ \text{eV}$

^a The relative energy of TS($^2A'$) in Figure 5 is 1.23 eV when calculated at B3LYP/6-311++G(3df) level.

^b See the PES of Figure 4-4.

The CuC Copper-Carbon Cluster

MPW1PW91/6-311++G(3df) calculations predict that the lowest energy multiplet of diatomic CuC is a quartet with bond length = 1.817 Å. The doublet spin state is higher by 0.266 eV. B3LYP/6-311++G(3df) calculations find that the doublet state is only marginally higher (0.049 eV) than the quartet. Both theoretical levels predict very low vibrational integral intensities, 14 and 10 km/mol, respectively, which accounts for CuC not being observed in our experiments.

The CuC₂ Copper-Carbon Cluster

Our calculations predict that singlet dicarbon (C₂) reacts spontaneously with Cu (X²S_{1/2}) to form a doublet cyclic cluster, *c*-CuC₂ (structure **B**). The predicted Cu-C bond strength is 2.33 eV (2.47 eV) [B3LYP (MPW1PW91)], only slightly larger than in quartet CuC, (1.99 eV (2.20 eV)). Table 4-1 shows that the strongest infrared mode in *c*-CuC₂ lies at 1750.3 cm⁻¹ (1768.7 cm⁻¹) (CC stretch), but since its calculated intensity is only 7 km/mol (5 km/mol), the absence of this band in our spectra is understandable.

The Cu₂C Copper-Carbon Cluster

The lowest energy isomers of this cluster are triplets of **C** and **D**. The **D** (linear) isomer is higher in energy by 1.35 eV (MPW1PW91/6-311++G(3df)). The highest IR integral intensity for the more stable cyclic isomer **C** is only 7 km/mol and in an energy range inaccessible by our FT-IR.

The Cu₂C₂ Copper-Carbon Cluster

Copper acetylide, *l*-CuC₂Cu (**E**), is well known in catalytic chemistry.⁸⁶ Predicted to appear at 662 cm⁻¹, this species is also absent in our spectra, presumably also because of its low concentration and intensity (65 km/mol). The second isomer *bc*-Cu₂C₂ (**F**) is higher in energy by 0.66 eV (Figure 4-3) and also has a very low IR intensity of 23 km/mol (Table 4-1).

The CuC₃ Copper-Carbon Cluster

Two stable structures were found for the CuC₃ cluster: near-linear, *nl*-CuC₃ (**G**), and bicyclic, *bc*-CuC₃ (**H**). The former is more stable by 0.64 eV (0.34 eV) in B3LYP (MPW1PW91) calculations (Table 4-2). The highest predicted band intensity for **H** is 25 km/mol for the 1595.8 cm⁻¹ band. This species is not observed here.

The predicted CuC bond length in *nl*-CuC₃ (**G**) is 1.838 Å (1.825 Å), close to the experimental value of 1.8296 Å in CuCN.¹⁰⁵ Unscaled predicted vibrational frequencies (and integral intensities) for *nl*-CuC₃ are 1900.5 (172 km/mol) (asymmetric CC stretch) and 1281.5 cm⁻¹ (31 km/mol) (symmetric CC stretch). The calculated (MPW1PW91) isotopomer frequencies for the CC asymmetric and symmetric modes in *nl*-Cu¹²C₃ were scaled by factors (listed in Table 4-3) so they match the observed 1830 and 1250 cm⁻¹ bands. Although the MPW1PW91 predictions match experimental intensities [1830.0 (1.0) and 1250.5 (0.17) cm⁻¹], the B3LYP calculation fails to predict the correct intensity ratio for these bands (Table 4-1). The intensities predicted by B3LYP are 134 and 9 km/mol, (1.0 and 0.067 relative intensities), respectively. The geometry predicted for **G** is substantially different using B3LYP vs. MPW1PW91, especially for the CuCC angle, 153.0 vs. 161.3 degrees, respectively. In addition, some predicted mode symmetries are different for the two calculational levels, even though the structures and electronic ground states are the same (Table 4-1). The failure of the B3LYP functional for the **G** isomer is likely related to the large difference (0.3 eV) in predicted energy stability of the **G** and **H** isomers.

To confirm the assignment of the observed bands to the near linear species, isotopic substitution experiments were run. Figure 4-2 shows bands due to the ^{12,13}C-isotopomers built on the 1830.0 and 1250.5 cm⁻¹ bands. Table 4-3 gives the comparison between the observed isotopomer bands and the predicted (and scaled) *nl*-⁶³Cu^{12/13}C₃ frequencies. The frequencies

predicted by the MPW1PW91/6-311++G(3df) calculations support the assignment of these bands to *nl*-CuC₃ (*X*²A') (**G**). However, the B3LYP/6-311++G(3df) calculation gives considerably poorer results. The maximum differences between experimental and predicted isotopomer frequencies, $\nu_{\text{exp}} - \omega_{\text{sc}}$, are 4.3 cm⁻¹ (B3LYP/6-311++G(3df)) and 1.6 cm⁻¹ (MPW1PW91/6-311++G(3df)). The average values of these differences for all observed isotopomers (for both modes) are 2.1 and 0.96 cm⁻¹, respectively. Although the 1.6 and 0.96 cm⁻¹ values (MPW1PW91) are typical for structures assigned using isotopic ¹³C labeling, the 4.3 and 2.1 cm⁻¹ (B3LYP) values are unacceptably large.

Figure 4-2 shows that in the 1200 cm⁻¹ range only two isotopomer bands (labeled **a** and **c**) appear, while eight appear for the higher frequency mode. To understand this requires looking at the integral intensities of the **c** and **d** isotopomers for both modes (Table 4-3). MPW1PW91 calculations predict that the integral intensities for the asymmetric and symmetric C=C stretching modes in the **c** isotopomer are 158 and 32 km/mol, while in **d** they are 176 and 26 km/mol, respectively. Thus, for the **c** isotopomer, the intensity ratio of the upper to the lower frequency band is expected to be ≈ 4.9 ($=158/32$), which is very close to the observed ratio of the 1788.1 cm⁻¹ to 1246.3 cm⁻¹ bands. But, for the **d** isotopomer, the predicted ratio is ≈ 6.8 ($=176/26$), so the lower frequency band should be substantially weaker. Its absence is thus understandable.

Information about the mechanism of formation of CuC₃ can be obtained from a comparison of the isotopomeric band pattern observed for CuC₃ vs that for C₃. The C₃ isotopomers (and relative band intensities) observed (but not displayed) in the present work were: 12-12-12 (1.0), 12-12-**13** (0.46), **13**-12-**13** (0.09), 12-**13**-12 (0.28), **13**-**13**-12 (0.20) and **13**-**13**-**13** (0.11). The CuC₃ isotopomers observed (and shown in Figure 4-2 and listed in Table 4-3)

were: **a** (63-12-12-12) (1.0), **b** (63-12-12-**13**) (≈ 0.12) + **d** (63-**13**-12-12) (0.29), **f** (63-**13**-12-**13**) (0.08), **c** (63-12-**13**-12) (0.29), **e** (63-12-**13**-**13**) (0.06) + **g** (63-**13**-**13**-12) (0.12), and **h** (63-**13**-**13**-**13**) (0.11). After summing the indicated band absorbances (because the same assumed $^{12/13}\text{C}_3$ reactant leads to the (**b**, **d**) and (**e**, **g**) product pairs), the observed isotopomer band pattern of $\text{Cu}^{12/13}\text{C}_3$ is very similar to the intensity pattern in $^{12/13}\text{C}_3$. We can thus conclude that Cu atoms react with already-formed C_3 molecules to form CuC_3 .

Table 4-3. Experimental (Ar matrix, 12K) and calculated isotopomer frequencies (integral intensities) for the asymmetric and symmetric CC stretch fundamental modes of fully optimized equilibrium geometry of near-linear $^{63}\text{Cu}^{12/13}\text{C}$ (**G**, Figure 4-3). Proposed band assignments marked in Figure 4-2 are given in the first column.

Isotopomer	ν^{exp} /cm $^{-1}$	$\omega_{\text{sc}}^{\text{a}}$	$\nu^{\text{exp}} - \omega_{\text{sc}}$	$\omega_{\text{sc}}^{\text{b}}$	$\nu^{\text{exp}} - \omega_{\text{sc}}$	
		/cm $^{-1}$ (km/mol)	/cm $^{-1}$	/cm $^{-1}$ (km/mol)	/cm $^{-1}$	
		B3LYP/6-311++G(3df)		MPW1PW91/6-311++G(3df)		
Asymmetric CC stretch mode						
a	63-12-12-12	1830.0	1830.0 (134)	0.0	1830.0 (171)	0.0
b	63-12-12- 13	1825.5	1824.2 (131)	1.3	1825.5 (168)	0.0
c	63-12- 13 -12	1788.1	1785.2 (125)	2.9	1786.6 (158)	1.5
d	63- 13 -12-12	1807.6	1810.4 (134)	-2.8	1807.7 (176)	-0.1
e	63-12- 13 - 13	1783.8	1779.5 (123)	4.3	1782.2 (154)	1.6
f	63- 13 -12- 13	1802.4	1803.8 (132)	-1.4	1802.6 (172)	-0.2
g	63- 13 - 13 -12	1764.4	1764.5 (125)	-0.1	1763.1 (162)	1.3
h	63- 13 - 13 - 13	1759.5	1758.0 (123)	1.5	1758.0 (158)	1.5
Symmetric CC stretch mode						
a	63-12-12-12	1250.5	1250.5 (9)	0.0	1250.5 (31)	0.0
b	63-12-12- 13		1224.6 (9)		1224.2 (32)	
c	63-12- 13 -12	1246.3	1248.7 (9)	-2.4	1247.8 (32)	-1.5
d	63- 13 -12-12		1228.4 (7)		1229.7 (26)	
e	63-12- 13 - 13		1222.3 (10)		1220.8 (33)	
f	63- 13 -12- 13		1202.9 (8)		1203.9 (27)	
g	63- 13 - 13 -12		1249.0 (7)		1227.9 (27)	
h	63- 13 - 13 - 13		1222.6 (8)		1201.4 (28)	

^a Frequencies are scaled uniformly by a scaling factor of 0.9627 for the asymmetric mode and 0.9826 for the symmetric mode.

^b Frequencies are scaled uniformly by a scaling factor of 0.9629 for the asymmetric mode and 0.9758 for the symmetric mode.

This conclusion is supported by annealing and photolysis results. Matrix annealing (to 35 K), followed by cooling back to 12 K, increases the intensities of the 1830.0 and 1250.5 cm^{-1} bands by $\sim 27\%$. This suggests that Cu ($X^2S_{1/2}$) reacts with C_3 ($X^1\Sigma_g^+$) as a result of diffusion at higher matrix temperatures. Photolysis for 1 hr with photon energies of $h\nu \leq 5.5$ eV reduced both the 1830.0 and 1250.5 cm^{-1} bands by $\sim 13\%$. The predicted lowest energy photodissociation path is $nl\text{-CuC}_3 + h\nu \rightarrow \text{Cu} + l\text{-C}_3$, with a dissociation energy of 2.07 eV (2.26 eV) (*cf.*, Table 4-2). This is close to the calculated Cu-C bond energy of 1.99 eV (2.20 eV) [B3LYP (MPW1PW91)] for diatomic CuC.

The Cu_2C_3 Copper-Carbon Cluster

Four stable C_{2v} isomers were found on the singlet Cu_2C_3 potential surface. The lowest energy one is w-shaped (**I**) and the other, less stable ones (**J**, **K**, and **L**) are either cyclic or crown-shaped. Again, the large difference in stability between **I** and **K** for B3LYP and MPW1PW91 functionals is reflected in large frequency differences predicted for the three highest energy modes, and in the mismatch of the fundamental mode symmetries of **K**, as listed in Table 4-1. The most intense mode predicted for **I** is 1776.4 cm^{-1} (437 km/mol), the asymmetric CC stretch. No bands assignable to **I** or **J**, **K**, **L** clusters have been observed in this energy region.

$^{12/13}\text{C}$ -Isotope Scrambling in the Near Linear CuC_3 Clusters

Since the **b** (63-12-12-**13**) and **d** (63-**13**-12-12) isotopomers originate from the same singly-substituted isotopic C_3 precursor (**13**-12-12), Cu might be expected to bond to either chain end with equal probability. If so, it follows that the **b** and **d** isomers should have about the same infrared intensities. Theoretical predictions roughly affirm this expectation. The **d** isomer is predicted to be about 5% more intense than **b**. But, as can be seen in Figure 4-2, this is not what

is observed. The intensity of the **d** band is approximately twice the intensity of the **b** band. A similar argument can be made for the doubly-substituted isomers, **e** (63-12-**13-13**) and **g** (63-**13-13-12**) (see Figure 4-2). **g** is observed to be approximately twice as intense as **e**.

This anomaly is the result of photoscrambling. As background, we first consider a similar observation in $^{12/13}\text{C}_3$ that was also ascribed to isotopic photoscrambling.¹⁰⁶ In $^{12/13}\text{C}_3$, scrambling requires photon energies in the 2.75-3.54 eV range (covering the $\tilde{a}^3\Pi_u$ ($^3\Pi$) \leftarrow $\tilde{A}^1\Pi_u$ \leftarrow $X^1\Sigma_g^+$ transition).¹⁰⁶ The maximum barrier to the forward and backward reactions along the $\tilde{a}^3\Pi_u$ ($^3\Pi$) \leftrightarrow TS ($^3A'$) \leftrightarrow $^3A'_2$ \leftrightarrow TS ($^3A'$) \leftrightarrow $\tilde{a}^3\Pi_u$ ($^3\Pi$) reaction pathway has been computed (using full configuration interaction) by Fueno and Taniguchi¹⁰⁷ as 2.82 eV. Visible/UV photolysis of C_3 induces intramolecular rearrangement to a cyclic C_3 intermediate. This is followed by specific bond breaking which leads to a gain in the 12-**13-12** and 12-**13-13** isomer concentrations. This increase results because these isomers have lower zero point energies (ZPE) than their precursors (12-12-**13** or **13-12-13**). The observation of isotopic scrambling in C_3 supports the existence of the $^3A'$ transition state and the intermediate triplet cyclic C_3 ($^3A'_2$) structure predicted by Fueno and Taniguchi.¹⁰⁷

We now consider the photo-induced isotopic scrambling in CuC_3 clusters. Because photoscrambling in C_3 involves a cyclic intermediate, a reaction pathway between **G** and **H** was sought theoretically. The calculated PES (MPW1PW91/6-311++G(3df)) for the Cu-12-12-**13** and Cu-**13**-12-12 isomers is displayed in Figure 4-4. The angle α ($\text{C}_1\text{C}_2\text{C}_3$) was incremented from 71.6° to 180° and, at each step, all other structural parameters fully optimized. Starting from the left **G** isomer, the PES rises 1.25 eV to a transition state, TS, and then falls to the **H** isomer, which lies 0.34 eV above **G**. The structural parameters for **G** and **H** are given in Figure 3 and, for the TS, are: $R(\text{C}_1\text{C}_2) = 1.2975 \text{ \AA}$, $R(\text{C}_2\text{C}_3) = 1.3238 \text{ \AA}$, $R(\text{C}_3\text{Cu}) = 1.8537 \text{ \AA}$,

$\alpha(\text{C}_1\text{C}_2\text{C}_3) = 100.46^\circ$ and $\beta(\text{CuC}_3\text{C}_2) = 144.3^\circ$. At $\alpha = 77^\circ$, the ${}^2\text{A}'$ energy surface (small squares in Figure 4-4) intersects with the **H** isomer distortion PES (large filled circles). The latter has a stable minimum at $\alpha = 71.6^\circ$. For the two curves calculated between $\alpha > 77^\circ$ and 93° , the lower one (${}^2\text{A}'$) almost preserves the C_{2v} symmetry of the **H** isomer, although it was calculated using C_s symmetry. The bond lengths found show that $\text{R}(\text{C}_1\text{C}_2) \approx \text{R}(\text{C}_2\text{C}_3)$ and $\text{R}(\text{CuC}_1) \approx \text{R}(\text{CuC}_3)$. However, for the higher energy curve (${}^2\text{A}'$), the CC bond length differences increase, i.e., $\text{R}(\text{C}_1\text{C}_2) - \text{R}(\text{C}_2\text{C}_3) = 0.01 - 0.03 \text{ \AA}$ and the CuC bond lengths differences become large. At $\alpha = 180^\circ$, CuC_3 is linear but exhibits one imaginary frequency (-61 cm^{-1}). The calculated barrier to linearity for the **G** isomer is so much smaller (39 cm^{-1}) than its computed vibrational frequencies (*cf.* Table 4-1), that the *nl*- CuC_3 (**G**) isomer can be characterized as quasilinear.

The isotopic scrambling can most easily be tracked by following a specific *nl*- CuC_3 isotopomer on the PES in Figure 4-4. First, consider the 63-12-12-**13** isotopomer **G** as the reactant. To drive the photoscrambling reaction, the **G** isomer must first absorb a photon and become electronically excited. From the doublet excited state, reversion to the ground state occurs partially by energy dissipation into the matrix bath modes and partially by internal conversion to the ground electronic state. After internal conversion, the **G** isomer presumably retains sufficient thermal energy to surmount the ground state TS barrier, thus converting to the **H** isomer. The ^{13}C atom will now be located on the right hand side of **H** (see Figure 4-4). Further irradiation may either convert it back to the left **G** isomer (by breaking the just-formed $\text{Cu}-^{13}\text{C}$ bond) or lead it to the right **G** isotopomer (by breaking the $\text{Cu}-^{12}\text{C}$ bond). Either reaction is equally probable. If the latter reaction occurs, the 63-**13**-12-12 isotopomer will be formed, and the ^{13}C isotope position will have been scrambled. If the former reaction occurs, no scrambling will have occurred, and reversion to the initial reactant ensues. Backward reactions from the right

isotopomer (through **H** to the left **G**) could then occur. The relative rates of the forward and backward rates are dependent on the energy differences of the two stable **G** isotopomers and may be calculated.

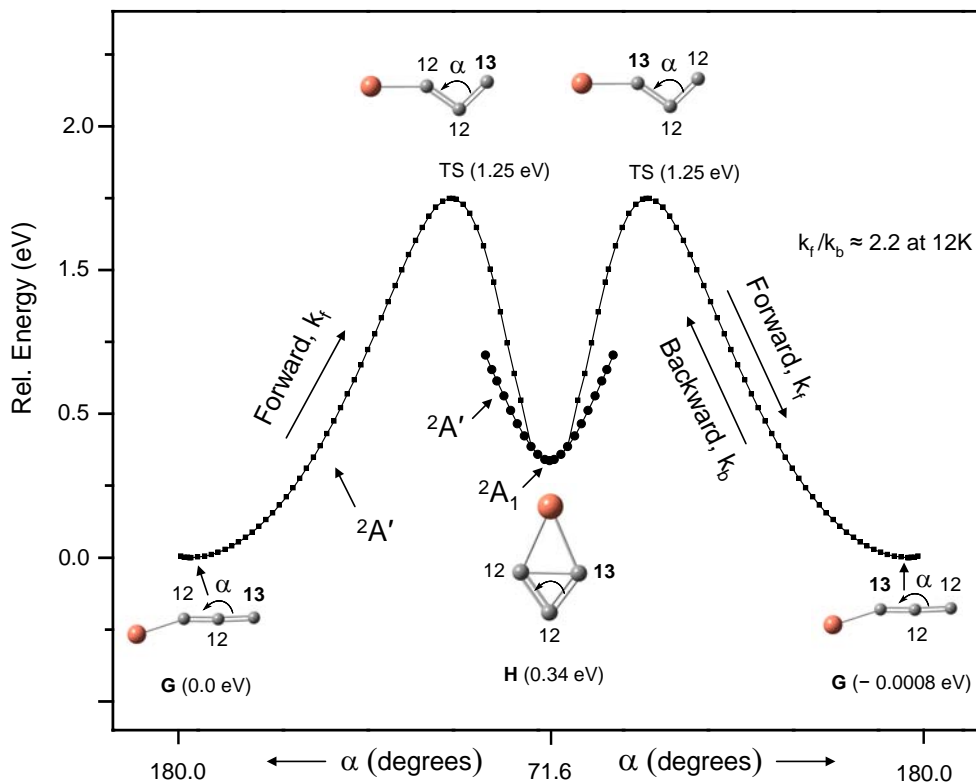


Figure 4-4. Total energy plot for the near linear CuC_3 ($^2A'$) and bicyclic CuC_3 ($^2A'$ and $^2A_1/2A_1$) clusters calculated at the MPW1PW91/6-311++G(3df) level by incrementing the α (CCC) angle in the range of $77 \leq \alpha \leq 180^\circ$ and $71.6 \leq \alpha \leq 93^\circ$, respectively. For each α the four remaining geometrical parameters were fully optimized. Note that the 63-12-12-**13** cluster reactant (left) rearranges to the 63-**13**-12-12 lower energy isotopomer product by breaking the ^{12}C -Cu bond in structure **H**, then passing over the TS and relaxing to the **G** product (right) in the forward reaction pathway.

The ratio of the forward-to-backward reaction rate constants, under thermal equilibrium conditions, can be described by

$$k_f/k_b = \exp(-\Delta G/kT) \quad (1)$$

where ΔG is the difference in the Gibbs free energy of products and reactants, k is the Boltzmann constant and T is the sample temperature.¹⁰⁸ At low temperatures (as in a matrix), it may be assumed that the changes in entropy are small, thus $\Delta G = \Delta E_{ZPE}$. Equation (1) can then be rewritten

$$k_f/k_b = \exp(-\Delta E_{ZPE} / kT) \quad (2)$$

The energy of the 63-13-12-12 isotopomer is lower than the 63-12-12-13 isotopomer by 6.6 cm^{-1} (MPW1PW91/6-311++G (3df)). Thus $\Delta E_{ZPE} = -6.6 \text{ cm}^{-1}$ and the ratio of the forward and reverse rate constants, estimated from (2), is ≈ 2.2 (at 12 K). Thus, the concentration of the 63-**13**-12-12 isotopomer **d** will increase at the expense of the 63-12-12-**13** isotopomer **b**, as observed in Figure 4-2.

A similar procedure can be applied to the 63-**13-13**-12 product and 63-12-**13-13** reactant isotopomers. Again, ΔE_{ZPE} was found to be -6.6 cm^{-1} and $k_f / k_b \approx 2.2$ (at 12 K). Thus, the 63-**13-13**-12 isotopomer **g** is expected to increase, while 63-12-**13-13** isotopomer **e** should decrease, again as observed.

The photo-induced $^{12/13}\text{C}$ -isotopic scrambling effect in CuC_3 could be applicable to those clusters potentially formed in interstellar space, both in the gas phase and/or trapped on cold grain surfaces. The scrambling reactions could be driven by the absorption of stellar UV-visible radiation or cosmic radiation which penetrates even to dark and cold nebular interiors. Such scrambling will yield isotopic fractionation in $^{63}\text{Cu}^{12/13}\text{C}_3$ clusters *via* the reactions described here.

Longer CuC_n ($n = 4 - 9$) clusters

As indicated in Figure 4-1, there are many larger carbon clusters are formed in the present experiments (i.e., larger than C_3). There are also many bands left unassigned (in spectrum b of

Figure 4-1), particularly in the 1800 cm^{-1} region. Some of these may be due to carbon and copper-bearing clusters. To investigate this possibility, we calculated equilibrium geometries and vibrational harmonic frequencies for clusters with stoichiometry CuC_n ($n = 4 - 9$) using MPW1PW91/6-311++G(3df) level of theory. The most stable geometries found are given in Figure 4-5 and the predicted vibrational frequencies in Table 4-4.

Table 4-4. Calculated (at MPW1PW91/6-311++G(3df)) harmonic vibrational frequencies and their integral intensities (in parentheses) for the CuC_n ($n = 4 - 9$) copper-carbon clusters (displayed in Fig. 4-5).

Cluster	Calc. (unsc.) freq's / cm^{-1} (km/mol)	Calc.(sc.) freq's ^a / cm^{-1} (km/mol)
CuC_4, C_s	2139.9(48), 1870.7(160), 1021.5(21), 500.7(0), 497.7(1), 362.9(10), 198.3(54), 148.7(14), 88.1(1)	1801.3 (160)
CuC_5, C_s	2041.6(0), 1945.1(1023), 1515.3(62), 870.2(23), 604.0(6), 518.8(1), 381.5(1), 344.2(7), 324.1(4), 177.6(24), 162.8(16), 62.8(2)	1872.9 (1023)
$\text{CuC}_6, C_{\infty v}$	2169.6(207), 2100.1(246), 1917.8(329), 1275.1(0), 750.3(18), 648.8(1), 616.2(1), 499.2(0), 452.9(9), 305.3(8), 274.4(1), 265.6(0), 156.5(21), 144.6(33), 57.5(1), 56.2(0)	2089.1 (207) 2022.2 (246) 1846.6 (329)
$\text{CuC}_7, C_{\infty v}$	2139.0(111), 2056.6(1), 1883.2 (2106), 1617.7(264), 1138.8(3), 697.4(3), 669.2(19), 584.0(0), 580.3(0), 491.6(0), 377.8(3), 351.2(10), 285.6(7), 226.7(0), 216.1(0), 123.8(21), 119.9(19), 44.8(0), 44.2(0)	1813.3 (2106)
$\text{CuC}_8, C_{\infty v}$	2205.7(1015), 2125.6(220), 2070.6(8), 1923.0(501), 1409.3(66), 1014.5(15), 692.4(0), 656.2(1), 599.3(17), 587.9(1), 573.2(0), 467.2(0), 432.5(0), 293.5(17), 288.5(7), 268.0(6), 198.0(1), 185.2(0), 104.4(17), 102.1(21), 37.7(0), 37.0(0)	2123.9 (1015) 1851.7 (501)
$\text{CuC}_9, C_{\infty v}$	2178.6(30), 2145.3(168), 2028.0(209), 1818.0(3419), 1666.5(558), 1293.6(71), 925.5(29), 734.7(4), 648.1(0), 642.6(0), 563.2(0), 549.0(18), 538.4(0), 475.5(0), 376.9(0), 351.4(2), 253.7(4), 251.7(13), 248.4(10), 162.9(1), 161.4(0), 86.4(15), 85.8(15), 30.5(0), 30.0(0)	1750.6 (3419)

^a Most intense C-C asymmetric stretch modes, only, they are scaled uniformly by 0.9629 factor, transferred from CuC_3 -nl cluster.

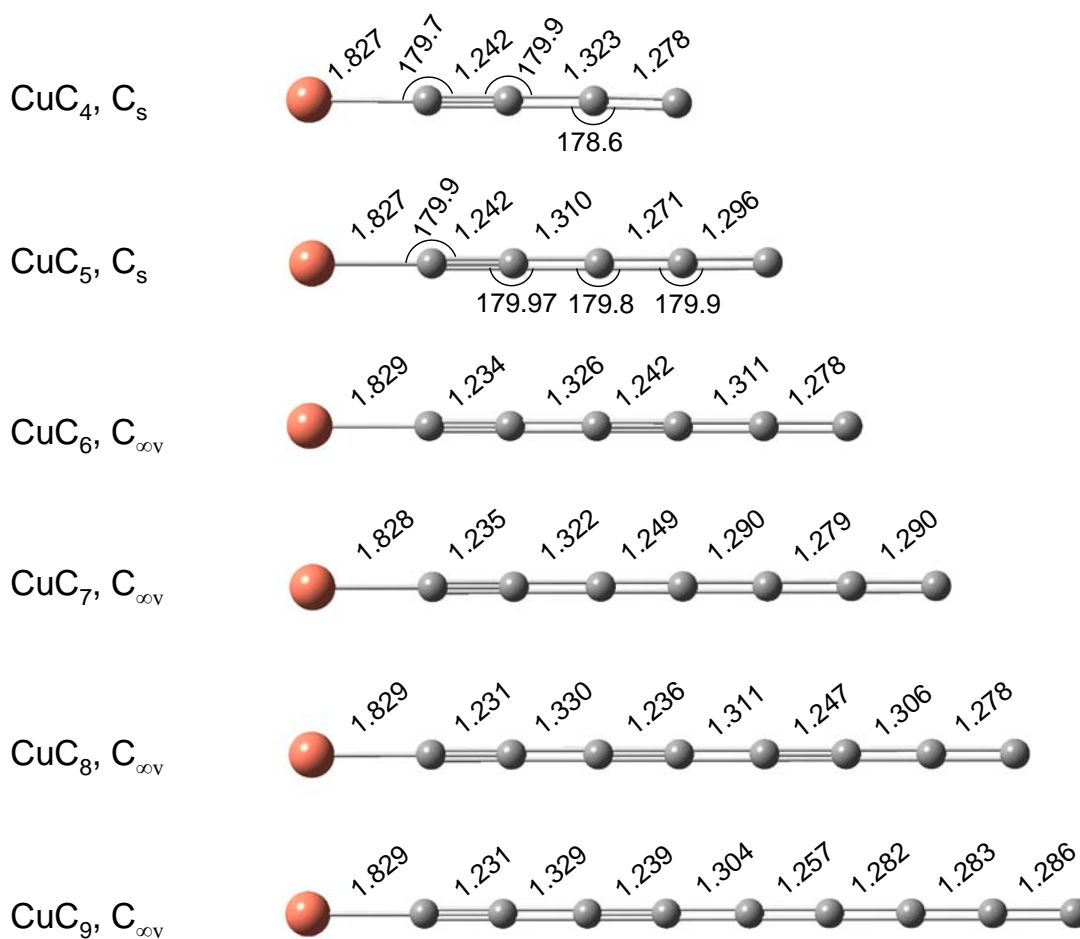


Figure 4-5. Optimized equilibrium structures for the CuC_n ($n = 4 - 9$) clusters. The bond lengths (Å) and angles (°) calculated at MPW1PW91/6-311++G(3df) are marked.

The lowest energy equilibrium geometries for the CuC_n ($n = 4 - 9$) clusters are near-linear C_s structures. While for the CuC_4 and CuC_5 clusters the $E_{\text{ZPE}}(C_{\infty v}) - E_{\text{ZPE}}(C_s)$ differences are 116 and 80 cm^{-1} , respectively, for larger clusters they are smaller than 30 cm^{-1} and decreases with the size of the cluster. For this reason, and because very similar mode frequencies and their integral intensities are found in both point group symmetries, the CuC_n ($n = 6 - 9$) are displayed in Figure 4-5 as linear ones. Similar to the pure linear carbon clusters some alternation in bond lengths is noted also in CuC_n ($n = 4 - 9$) clusters, particularly on Cu side of the cluster. But, generally, the carbon-carbon bonding is different in CuC_n ($n = 4 - 9$) clusters than in C_n ($n = 4 -$

9) clusters, with some triple $C \equiv C$ bonds form (see Figure 4-5). The bonding differences and mass effect are reflected in big changes in the infrared spectra when compared to pure C_n clusters. The most intense $C = C$ asymmetric stretch vibrations in the C_n ($n = 3 - 9$) clusters occur in the $2165 (C_5) - 1544 \text{ cm}^{-1}(C_4)$ region, while for the CuC_n ($n = 3 - 9$) clusters this mode is located in the narrow $1873 - 1751 \text{ cm}^{-1}$ region (Note: uniform scaling for the harmonic calculated frequencies from nl- CuC_3 was applied for all clusters (see Table 4-5)). It is interesting to note that only the CuC_n clusters with an even number of carbons have strong bands in the high energy region. Such clusters have also different C-C bonding than odd number carbons CuC_n clusters. This is indicated by increasing number of triple CC bonds in even-numbered clusters (see Figure 4-5).

The most intense calculated (and scaled) mode frequencies in Table 4-5 can be used to find any energy coincidences with the observed extra bands in the Cu/C/Ar experiment of Figure 4-1. The frequencies of all the strongest bands predicted for the CuC_n ($n = 4 - 9$) are grouped in the narrow energy range of $2124 - 2022 \text{ cm}^{-1}$ and $1873 - 1751 \text{ cm}^{-1}$, they overlap some of the extra bands that were observed in the $2117 - 2061 \text{ cm}^{-1}$ and $1896 - 1787 \text{ cm}^{-1}$ range, respectively. Thus, it is very likely that those weak experimental bands observed in Figure 4-1 in both regions are due to the CuC_n ($n = 4 - 9$) clusters. However, these extra bands were very weak, so that ^{13}C -isotope labeled experiments did not help in this case because the isotopomer bands are usually much smaller than the all- ^{12}C bands. In order to make further assignments of these bands, we tried to produce copper-carbon clusters and trap them in nitrogen matrices instead of the solid argon matrices. Longer carbon chains C_n ($n > 3$) have been observed to form in nitrogen matrices. For instance, linear C_{11} clusters were formed and studied in nitrogen matrices. The intensities of the C_{11} bands were much larger in nitrogen matrices compared to argon matrices so

that ^{13}C isotopic substitution experiments were employed to successfully assign the C_{11} bands.¹⁰⁹ Therefore, we ran experiments in nitrogen matrices, expecting to form larger linear carbon clusters and therefore larger CuC_n clusters, such as CuC_5 and CuC_7 . However, this approach was not very successful and the bands were still too small to assign. Only theoretical work of longer CuC_n ($n = 4 - 9$) clusters were presented in this dissertation.

Summary

After the ablation and trapping of copper and carbon in an argon matrix, new infrared absorption bands were observed at 1830.0 and 1250.5 cm^{-1} . These bands have been assigned to the two most intense modes, i.e, the asymmetric and symmetric C=C stretches, of the Cu-carbon cluster, $nI\text{-}^{63}\text{CuC}_3$. This assignment was supported by calculations using density functional theory with MPW1PW91 functional and 6-311++G (3df) basis set. The MPW1PW91/6-311++G (3df) approach predicts the relative integral intensities for these modes quite well. However, the BPW91/6-311++G(3df) [carbons]// SDD pseudopotentials [Cu] and B3LYP/6-311++G(3df) calculations failed to correctly predict the ^{13}C -labeled infrared isotopomer frequencies and the relative integral intensities for those modes.

The photo-induced isotopic scrambling in $^{63}\text{Cu}^{12/13}\text{C}_3$ isotopomers was observed and explained *via* a computed (MPW1PW91/6-311++G(3df)) PES for this reaction. The forward reactions of $\mathbf{G} \rightarrow \mathbf{G}^* \rightarrow \text{TS} \rightarrow \mathbf{H} \rightarrow \text{TS} \rightarrow \mathbf{G}$ indicates that scrambling in the isotopomers 63-12-12-13 (**b**) \rightarrow 63-13-12-12 (**d**) and 63-12-13-13 (**e**) \rightarrow 63-13-13-12 (**g**) occurs via the bicyclic **H** isomer. At 12 K the estimated forward rate constant (k_f) is 2.2 times larger than the backward rate constant (k_b), so the accumulation of 63-13-12-12 and 63-13-13-12 isotopomers is expected during matrix photolysis, exactly as observed.

A number of pure carbon clusters larger than C_3 , seen in Figure 4-1, were formed in the present experiments. Many bands, mainly in the 1775 - 1900 cm^{-1} range, in Figure 4-1b have

been left unassigned. It is likely that many are due to products of reactions of larger carbon clusters with copper. Theoretical calculation using MPW1PW91/6-311++G(3df) level of theory predicts that the lowest energy equilibrium geometries for the CuC_n ($n = 4 - 9$) clusters are near linear C_s structures. However, for CuC_n ($n = 6 - 9$) clusters, the energy difference between the linear structure and near-linear structure are very small (less than 30 cm^{-1}) and the difference decreases as the length of the clusters increases. The frequencies of the strongest bands predicted for the CuC_n ($n = 4 - 9$) are grouped in the range of $2124 - 2022 \text{ cm}^{-1}$ and $1873 - 1751 \text{ cm}^{-1}$.

CHAPTER 5 SILVER-CARBON CLUSTER: STRUCTURE AND INFRARED FREQUENCIES

Introduction

The interaction of metals with carbon has been a topic of long-standing interest. In part, this is the result of the potential involvement of metal-carbon molecules in catalysis.^{110,111} Ever since the discovery of the novel metallocarbohedrenes (“met-cars”) by Castleman and coworkers, metal-carbon research has accelerated.⁸⁵ Met-cars have been formed with the stoichiometry M_8C_{12} where $M = Ti, V, Zr, Nb, Mo, Hf, Cr,$ or Fe , but they can also be formed with two metals with stoichiometry $Ti_{8-x}M_xC_{12}$, where M is $Si, Y, Zr, Nb, Mo, Hf, Ta,$ or W .¹¹²⁻¹¹⁵ Other types of clusters have also been studied. These have included the anionic clusters $V_mC_n^-$ ($m=1-4, n=2-8$), $Co_2C_n^-$ ($n=2, 3$), and $Nb_2C_n^-$ ($n=4-9$), studied by photoelectron spectroscopy and density functional theory (DFT) calculations.¹¹⁶⁻¹¹⁸ Wang and coworkers investigated the first row transition metal- C_3 clusters MC_3^- (with $M=Sc, V, Cr, Mn, Fe, Co, Ni$) as well as FeC_n^- ($n=3, 4$), NbC_n^- ($n=2-7$) and TiC_n^- ($n=2-5$) also using photoelectron spectroscopy.¹¹⁹⁻¹²² Similar studies on MC_n^- clusters (with $M=Sc, Y, La; n=5-20$) were reported by Kohno et al.¹²³ $Cu_nC_2^+$ ($n=2k+1, k=1-7$) and $Cu_nC_4^+$ ($n=2k+1, k=2-4$) clusters were studied using time-of-flight mass spectrometry.⁸⁸ Cationic CuC_n^+ clusters ($n=1-3$) were generated in spark discharges of Cu and graphite, and observed in mass spectrometric studies.⁸⁴ Matrix isolation vibrational spectroscopy studies of $GeC_3Ge, TiC_3, CrC_3, CoC_3, AlC_3, AlC_3Al$ and NiC_3Ni have been reported by Graham and coworkers.^{79-83,124} Copper and Silver polyynides (Cu and Ag -capped carbynes) were characterized using Raman spectroscopy.¹²⁵ Other properties of metal-carbon clusters including trends in ionization potentials and electronic affinities have been investigated as well.^{126,127} Studies of CuC_3 and its photo-induced isotopic scrambling were

recently reported by us.¹²⁸ Since silver is similar in electron configuration to copper, it is interesting to see whether similar, or different, silver-carbon clusters are formed.

Only a few reports on silver-carbon clusters have appeared. Silver acetylide ($\text{AgC}\equiv\text{CAg}$), one of the oldest organometallics, was synthesized by reacting acetylenic compounds with an ammoniacal silver nitrate solution.^{129,130} Cationic AgC_n^+ clusters ($n = 1-3$), generated in a radio frequency spark ion source, were investigated using mass spectrometric methods.⁸⁴

In this chapter, we report the first vibrational spectroscopic study of a silver-carbon cluster trapped in solid argon at 12 K. Corresponding theoretical work on small stable silver-carbon clusters, Ag_mC_n ($m = 1, 2$; $n = 1, 2, 3$) using density functional calculations has been carried out in the search for the equilibrium geometry and vibrational frequencies of the cluster giving rise to the two new bands observed. Both experiments and calculations indicate that the near-linear AgC_3 cluster is responsible.

Computational and Experimental Details

Experimental Methods

Silver-carbon clusters were generated by two-beam laser ablation of silver and graphite, or, in the case of the isotopic studies, a pressed pellet of ^{12}C and ^{13}C (ISOTECH). The experimental apparatus used for the generation and trapping of silver-carbon clusters in solid argon is similar to that described in Chapter 2 and Chapter 4. Briefly, the output of a pulsed Nd: YAG laser (1064/532 nm, 0.2 – 0.5W, 10Hz) was split into two beams, with one beam focused on a small piece of silver sample (SPEX), and the other beam focused on the carbon sample. The reaction products were co-deposited with argon gas onto a 12K CsI window cooled by a closed-cycle helium cryostat (APD Displex). After 2-3 hours deposition, infrared absorption spectra were collected using a NICOLET Magna 560 FT-IR spectrometer (0.5 cm^{-1} resolution). Annealing of

the matrix (heating to 35 K and recooling to 12 K), as well as photolysis with a medium pressure 100W Hg lamp, were also performed to induce secondary reactions.

Computational Methods

All calculations were carried out using the Gaussian 03 suite of programs.⁷³ The equilibrium geometries, harmonic vibrational frequencies, and dissociation energies were calculated using the MPW1PW91 functional, a modified Perdew-Wang exchange and correlation functional,^{74,75} with a SDD (the Stuttgart/Dresden ECP's and D95V basis set for silver and carbon, respectively).¹³¹ In previous work, the SDD basis set was chosen to calculate M-NH₃ (M = Cu, Ag) and M⁺-H₂S (M = Cu, Ag, Au) systems.^{132,133} The MPW1PW91 functional was recommended by Wiberg,⁹⁰ Dunbar,⁹¹ and Oomens et al.⁷⁶ for the calculation of C, H, and metal-containing systems. The MPW1PW91 functional was also used in our recent studies of iron complexed with cationic and neutral polycyclic aromatic hydrocarbons.^{72,92}

In our previous work on the CuC₃ cluster,¹²⁸ we compared the results calculated by the MPW1PW91 functional and the B3LYP (Becke's three-parameter hybrid functional combined with the non-local correction functional of Lee, Yang, and Parr),⁸⁹ respectively. It showed that calculations using the MPW1PW91 functional supported the experimental data, whereas the B3LYP functional did poorly in predicting the ¹³C-labeled isotopomer frequencies and the relative integral intensities of ⁶³Cu^{12/13}C₃. Since silver and copper atoms have similar electronic configurations (Ag([Xe]4d¹⁰5s¹) and Cu([Ar]3d¹⁰4s¹)), we tested the MPW1PW91/SSD level of calculation on the near-linear CuC₃ cluster by comparing them to the MPW1PW91/6-311++(3df) results and to the experimental ⁶³Cu^{12/13}C₃ isotopomer frequencies.¹²⁸ The comparison revealed that the maximum isotopomer frequency differences (after scaling) between MPW1PW91/SSD and experiment is 2.3 cm⁻¹, with an average difference of 1.3 cm⁻¹, compared to the 1.6 cm⁻¹ and 0.96 cm⁻¹ values when the MPW1PW91/6-311++(3df) was used.¹²⁸ Although the

MPW1PW91/SDD numbers are a little higher than the MPW1PW91/6-311++(3df) ones, they are still acceptable for isotopic ^{13}C isotopomer frequency matching. For this reason, we used the MPW1PW91/SSD functional/basis set in the present work.

Experimental Infrared Spectra

The infrared absorption spectra in the 1180-1250 cm^{-1} and 1750-2200 cm^{-1} range for the species laser-ablated from graphite and for the species formed by the synchronized dual laser ablation of silver and graphite are displayed in Figure 5-1 in panels a and b, respectively. Various neutral carbon clusters (from $\text{C}_3 - \text{C}_{12}$) were observed in both spectrum a and b.^{95,96} Bands at 1936.5 cm^{-1} in spectrum b is assigned to C_6^{\ominus} .⁹⁸ Impurities such as CO and H_2O are also present in the experiments, due to high laser ablation power.⁸¹ A weak band at 1824.4 cm^{-1} , assigned to C_3H ,^{100,101} was also observed.

Two new bands were observed in spectrum b, at 1827.8 and 1231.6 cm^{-1} . The higher frequency band is about three times more intense than the lower frequency one. Both were found to be dependent on silver and carbon concentrations, and are thus attributed to a species containing both silver and carbon.

Numerous experiments were performed to determine whether the bands belong to the same species. Different Ag/C ratios were affected by varying the ablating laser intensities. The two new bands decrease in intensity with lower ablation power and increase with higher power. Matrix annealing up to 35 K and recooling to 12 K increases the intensity of both bands by about 25%. UV-visible photolysis with a medium pressure mercury lamp up to 1 hour decreases both bands about 15%. Under all these different conditions, the integral intensity ratio of the 1827.8 and 1231.6 cm^{-1} bands remained constant ($= 3.03 \pm 0.3$), indicating that they belong to the same species.

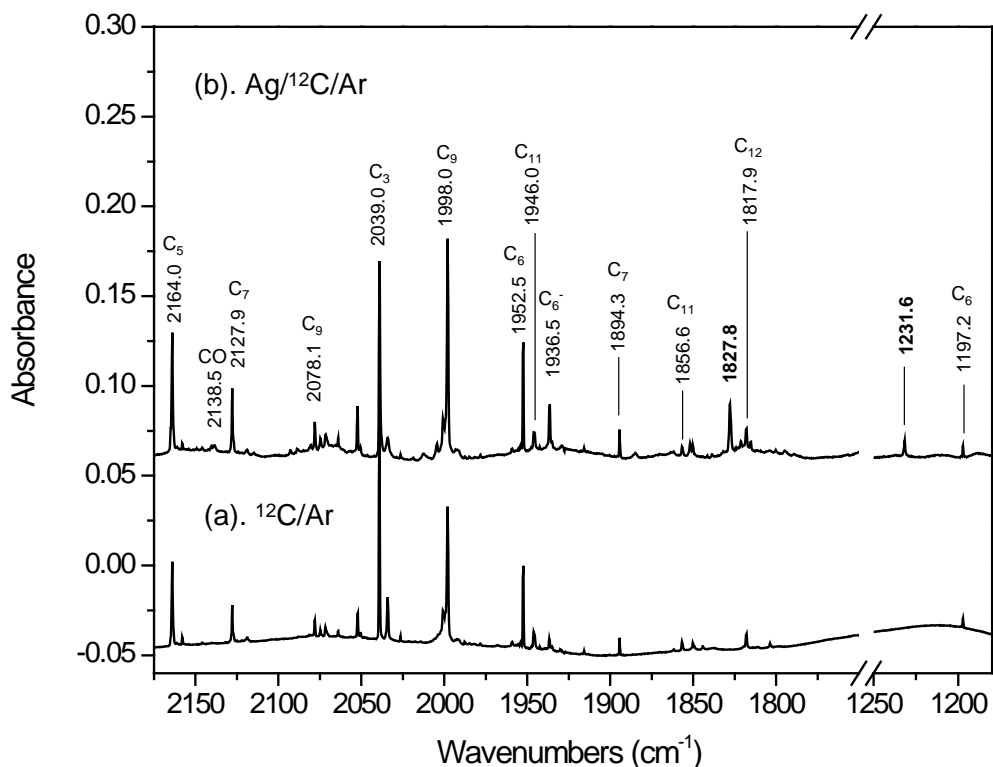


Figure 5-1. Infrared absorption spectra of products of laser ablation of graphite (spectrum a) and products of two-beam laser ablation of graphite and silver (spectrum b). The spectra were recorded after matrix annealing to 35K then cooling back to 12 K. The major bands due to pure carbon clusters and their reaction products with silver at 1827.8 and 1231.6 cm^{-1} are indicated.

Isotopic (^{13}C) substitution is a powerful means of identifying the structure of unknown molecular system. Figure 5-2 shows the spectrum of the reaction products of the laser ablation of Ag and ^{12}C (spectrum a) compared to the spectrum of reaction products of laser ablation of Ag and $^{12/13}\text{C}$ mixture (spectrum b). There are clearly eight isotopomeric bands (a – h) built on the 1827.8 cm^{-1} band in the ^{13}C -labeled spectrum. In the lower energy region (1231.6 cm^{-1} band), eight very weak bands were also observed. They are here tentatively assigned to various isotopomers (see Table 5-2). A similar isotopomer band pattern was previously observed for the near-linear $^{12/13}\text{CuC}_3$ cluster,¹²⁸ the near-linear $^{12/13}\text{C}_3\cdot\text{H}_2\text{O}$ complex,¹⁰⁴ and the linear $^{12/13}\text{C}_3\text{Cr}$

and $^{12/13}\text{C}_3\text{Co}$ clusters.^{81,83} This strongly suggests that the 1827.8 cm^{-1} band should be assigned to the CC asymmetric stretching mode in linear or near-linear $^{12/13}\text{C}_3$ isotopomers bonded at one end to Ag. This preliminary conclusion is confirmed in the next section by computation of the equilibrium geometries and harmonic frequencies of a number of silver-carbon clusters, including $\text{Ag}^{12/13}\text{C}_3$.

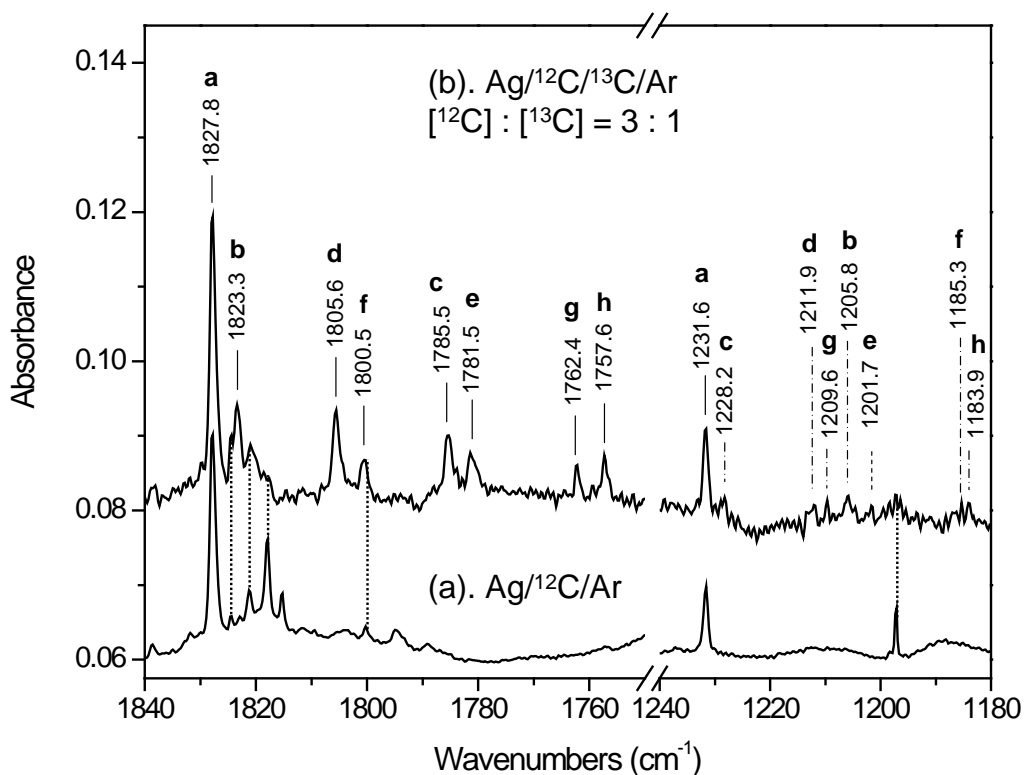


Figure 5-2. Infrared spectra of reaction products from laser ablation of Ag and ^{12}C (spectrum a) and from laser ablation of Ag and $^{12/13}\text{C}$ (spectrum b). The bands marked by vertical dashed lines are tentatively assigned to isotopomeric partners of the 1231.6 cm^{-1} band. The bands marked by vertical dotted lines are due to: C_3H (1824.4 cm^{-1}),^{100,101} C_2H^+ (1820.2 cm^{-1}),¹⁰² C_{12} (1817.9 cm^{-1}),¹⁰³ and C_6 (1197.2 cm^{-1}).¹³⁴

Equilibrium Geometries and Vibrations for Ag_mC_n ($m=1, 2$; $n=1-3$) Clusters.

A number of metal-carbon clusters of the type MC_3 and MC_3M ($M = \text{transition metal}$) have been studied previously.^{79-83,124,128} Here we explore theoretically the AgC , AgC_2 , AgC_3 , Ag_2C ,

Ag₂C₂ and Ag₂C₃ clusters. Figure 5-3 shows the stable equilibrium geometries and relative energies predicted (MPW1PW91/SDD) for these clusters. Harmonic vibrational frequencies and integral intensities are displayed in Table 5-1.

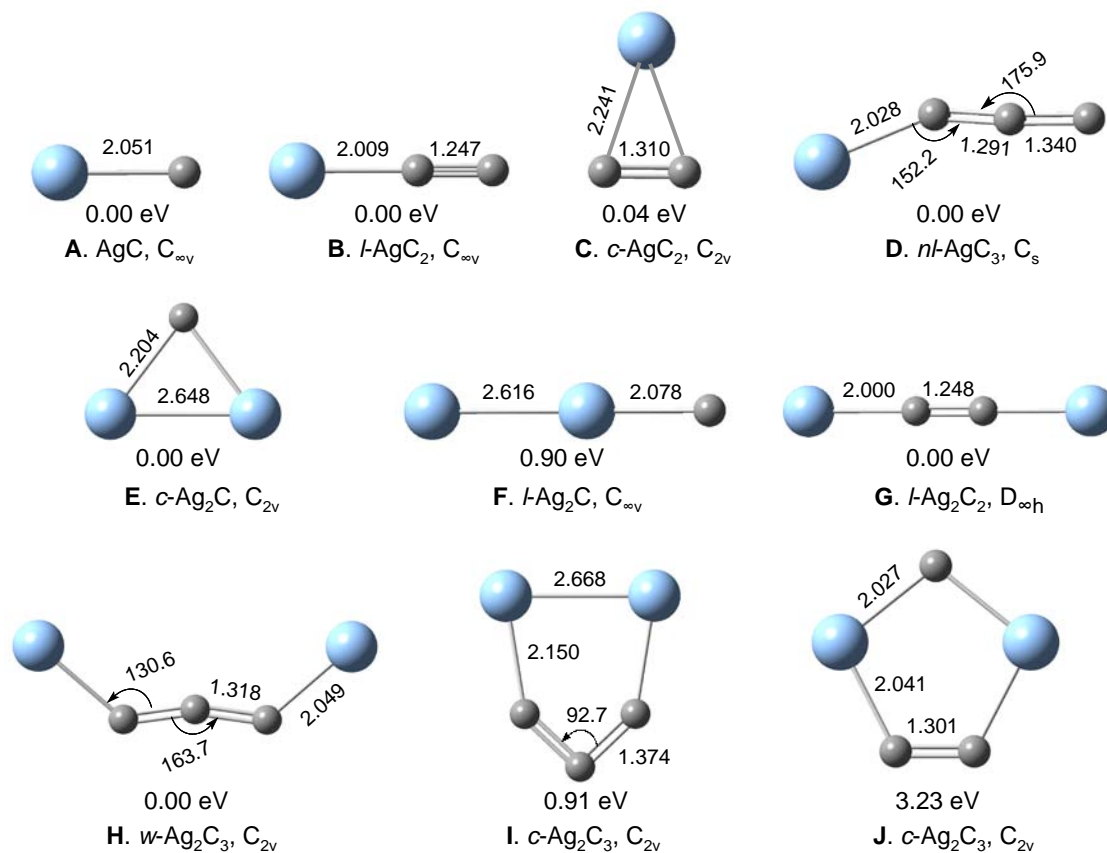


Figure 5-3. Equilibrium structures for the AgC, AgC₂, AgC₃, Ag₂C, Ag₂C₂, and Ag₂C₃ clusters. The bond lengths (Å) and angles (°) calculated at MPW1PW91/SDD are marked. The relative isomer energies are indicated.

The AgC Silver-Carbon Cluster

The ground state of diatomic AgC is calculated to be a quartet with a bond length of 2.051 Å. The doublet spin state is higher in energy than the quartet by 0.31 eV. The calculation indicates a very low vibrational integral intensity (9 km/mol), which is probably the reason why AgC was not observed in the experiments.

Table 5-1. Vibrational Frequencies (cm^{-1}) and Integral Intensities (km/mol) for Electronic Ground States of Ag_mC_n ($m = 1, 2; n = 1, 2, 3$) Clusters (displayed in Figure 5-3), Calculated Using MPW1PW91/SDD Functional/basis sets.

Ag_mC_n Isomer	MPW1PW91/SDD
A. AgC ($X^4\Sigma$)	σ 477.2 (9)
B. $l\text{-AgC}_2$ ($X^2\Sigma$)	σ 2018.5 (34), σ 425.0 (21), π 97.2 (2x2)
C. $c\text{-AgC}_2$ (X^2A_1)	a_1 1702.2 (16), a_1 369.8 (11), b_2 179.0 (0)
D. $nl\text{-AgC}_3$ (X^2A')	a' 1860.0 (117), a' 1224.1 (14), a' 421.9 (35), a' 335.8 (9), a'' 227.6 (5), a' 101.4 (17)
E. $c\text{-Ag}_2\text{C}$ (X^3A_2)	a_1 388.7 (2), b_2 255.7 (4), a_1 156.1 (0)
F. $l\text{-Ag}_2\text{C}$ ($X^3\Sigma_g$)	σ 417.7 (4), σ 158.7 (1), π 110.7 (1), π 42.5 (0)
G. $l\text{-Ag}_2\text{C}_2$ ($X^1\Sigma_g$)	σ_g 2092.4 (0), σ_u 600.3 (78), π_g 239.5 (2x0), σ_g 183.9 (0), π_u 83.9 (2x51)
H. $w\text{-Ag}_2\text{C}_3$ (X^1A_1)	b_2 1761.1 (639), a_1 1265.7 (11), a_1 547.3 (0), b_2 449.7 (44), b_1 289.9 (2), a_1 261.5 (9), a_2 215.9 (0), b_2 115.0 (155), a_1 36.4 (4)
I. $c\text{-Ag}_2\text{C}_3$ (X^1A_1)	a_1 1390.4 (721), b_2 1297.4 (0), a_1 355.3 (120), b_2 335.4 (30), b_1 334.2 (4), a_1 317.3 (1), a_1 150.3 (2), b_2 134.8 (10), a_2 120.7 (0)
J. $c\text{-Ag}_2\text{C}_3$ (X^1A_1)	a_1 1705.6 (103), a_1 519.1 (18), b_2 510.0 (0), a_1 465.3 (7), b_2 452.1 (0), a_2 233.3 (0), b_2 187.7 (43), b_1 174.0 (22), a_1 101.3 (0)

The AgC_2 Silver-Carbon Cluster

Two structures, **B** and **C** in Figure 5-3, are predicted for AgC_2 . Linear $l\text{-AgC}_2$ (**B**) is marginally more stable by 0.04 eV than cyclic $c\text{-AgC}_2$ (**C**). Table 5-1 shows that the strongest infrared modes in $l\text{-AgC}_2$ and $c\text{-AgC}_2$ lie at 2018.5 and 1702.2 cm^{-1} , respectively. However, since the calculated integral intensities are relatively low, 34 and 16 km/mol , the absence of these two bands is understandable.

The AgC_3 Silver-Carbon Cluster

Only one stable structure (**D**) is found for the AgC_3 cluster: the near linear one, as displayed in Figure 5-3. The bond lengths and angles calculated using MPW1PW91/SDD level are marked in the figure. The $nl\text{-AgC}_3$ cluster has a doublet spin multiplicity. Searches for

doublet bicyclic-AgC₃ and cyclic-C₃ bonded to Ag each resulted in one imaginary frequency. Predicted vibrational frequencies (unscaled) and integral intensities for *nl*-AgC₃ are 1860.0 cm⁻¹ (117 km/mol) (asymmetric CC stretch mode) and 1224.1 cm⁻¹ (14 km/mol) (symmetric CC stretch mode). The intensity ratio of the two bands is relatively high (8.36) compared to experiment (3.03 ± 0.3). The B3LYP functional with SDD basis set was also tested on *nl*-AgC₃. The predicted vibrational frequencies (and integral intensities) are 1864.9 (133) and 1211.4 cm⁻¹ (9 km/mol), an even worse prediction of the intensity ratio.

To confirm the assignment of the observed bands to the near-linear species, isotopic substitution experiments were run. Figure 5-2 shows bands due to the ^{12,13}C-isotopomers built on the 1827.8 and 1231.6 cm⁻¹ bands. The comparison between the observed isotopomer bands and the predicted (scaled) *nl*-¹⁰⁷Ag^{12/13}C₃ frequencies are listed in Table 5-2. As found in the study of CuC₃ clusters, the harmonic vibrational frequencies predicted by the MPW1PW91/SDD calculations is in good agreement with the assignment of these bands to *nl*-AgC₃ (*X*²A') (structure **D**), while the B3LYP/SDD match is again poorer. The maximum differences between experimental and predicted isotopomer frequencies, $\nu_{\text{exp}} - \omega_{\text{sc}}$, are 4.3 cm⁻¹ for B3LYP/SDD and 1.8 cm⁻¹ for MPW1PW91/SDD. The average values of these differences for all observed isotopomers (for both modes) are 1.3 (B3LYP) and 0.63 cm⁻¹ (MPW1PW91). Although the 1.8 and 0.63 cm⁻¹ values are typical for structures assigned using isotopic ¹³C labeling, the 4.3 and 1.3 cm⁻¹ B3LYP values are too large to be acceptable. Thus, based on the comparison with the MPW1PW91 calculation, we conclude that *nl*-AgC₃ (structure **D**) was formed in our experiments and is responsible for the two bands at 1827.8 and 1231.6 cm⁻¹.

Table 5-2. Comparison of Experimental and Calculated Isotopomer Frequencies (Integral Intensities) for the Asymmetric C=C Stretch and Symmetric C=C Stretch Fundamental Modes of Near Linear $^{107}\text{Ag}^{12/13}\text{C}_3$.

Isotopomer	$\nu_{\text{exp}}^{\text{a}}$ /cm ⁻¹	B3LYP/SDD		MPW1PW91/SDD		
		$\omega_{\text{sc}}^{\text{b}}$ /cm ⁻¹ (km mol ⁻¹)	$\nu_{\text{exp}} - \omega_{\text{sc}}$ /cm ⁻¹	$\omega_{\text{sc}}^{\text{c}}$ /cm ⁻¹ (km mol ⁻¹)	$\nu_{\text{exp}} - \omega_{\text{sc}}$ /cm ⁻¹	
Asymmetric C=C stretch mode						
a	107-12-12-12	1827.8	1827.8 (133)	0.0	1827.8 (117)	0.0
b	107-12-12- 13	1823.3	1822.0 (132)	1.3	1823.2 (115)	0.1
c	107-12- 13 -12	1785.5	1782.9 (125)	2.6	1784.1 (108)	1.4
d	107- 13 -12-12	1805.6	1808.1 (132)	-2.5	1805.7 (118)	-0.1
e	107-12- 13 - 13	1781.5	1777.2 (124)	4.3	1779.7 (106)	1.8
f	107- 13 -12- 13	1800.5	1801.6 (131)	-1.1	1800.5 (116)	0.0
g	107- 13 - 13 -12	1762.4	1762.3 (125)	0.1	1760.9 (110)	1.5
h	107- 13 - 13 - 13	1757.6	1755.9 (123)	1.7	1755.8 (108)	1.8
Symmetric C=C stretch mode						
a	107-12-12-12	1231.6	1231.6 (9)	0.0	1231.6 (14)	0.0
b	107-12-12- 13	1205.8	1205.3 (9)	0.5	1204.8 (15)	1.0
c	107-12- 13 -12	1228.2	1230.0 (9)	-1.8	1229.2 (14)	-1.0
d	107- 13 -12-12	1211.9	1210.4 (8)	1.5	1211.7 (12)	0.2
e	107-12- 13 - 13	1201.7	1203.2 (9)	-1.5	1201.9 (15)	-0.2
f	107- 13 -12- 13	1185.3	1184.5 (8)	0.8	1185.3 (12)	0.0
g	107- 13 - 13 -12	1209.7	1209.3 (8)	0.4	1210.0 (12)	-0.3
h	107- 13 - 13 - 13	1183.9	1183.1 (8)	0.8	1183.2 (13)	0.7

^a Experimental band energies for symmetric mode are tentative due to their weak intensities.

^b Frequencies are scaled uniformly by scaling factor of 0.9801 for asymmetric mode and by 1.0167 for symmetric mode.

^c Frequencies are scaled uniformly by scaling factor of 0.9795 for asymmetric mode and by 1.0061 for symmetric mode.

When silver bonds to either end of the same singly-substituted isotopic precursor, i.e., $^{12/13}\text{C}_3$ (12-12-**13**), both **b** (107-12-12-**13**) and **d** (107-**13**-12-12) isotopomers may be formed. Figure 5-2 shows that the **b** and **d** bands have comparable intensities, as expected. Similarly, when Ag attaches to the C_3 (12-**13**-**13**) precursor, both **e** (107-12-**13**-**13**) and **g** (107-**13**-**13**-12) isotopomers are formed. Again, Figure 5-2 shows that the **e** and **g** bands have similar intensities. In our previous study of CuC_3 , it was found that the analogous sets of isotopomeric bands were *not* of equal intensity. It was shown that this resulted from photo-induced isotopic scrambling of ^{13}C and ^{12}C isotopes in the cluster. The present observation that the bands in the **b**, **d** set and in

the **e**, **g** set retain their equal intensities leads to the conclusion that no photo-induced isotopic scrambling takes place in AgC_3 . The photoscrambling in CuC_3 and C_3 involves a cyclic intermediate,^{106,107,128} but such a stable cyclic structure could not be found for AgC_3 .

It is interesting to compare the structural parameters and binding energies of the *nl*- AgC_3 and *nl*- CuC_3 clusters, both calculated at the MPW1PW91/SDD level. The metal-carbon bond lengths (BL) in *nl*- AgC_3 are much longer than in *nl*- CuC_3 . The BL (Ag-C) = 2.028 Å vs BL (Cu-C) = 1.810 Å. On the other hand, the carbon-carbon BLs are similar. In AgC_3 , the CC BLs are 1.291 and 1.340 Å, while in CuC_3 , they are 1.287 and 1.342 Å. The bond angle Ag-C-C in *nl*- AgC_3 is significantly smaller (152.2°) than in *nl*- CuC_3 (160.6°). The longer bond lengths in *nl*- AgC_3 reflect its lower dissociation energy (1.77 eV) compared to 2.38 eV for *nl*- CuC_3 . The Ag-C bond is weaker than the Cu-C bond by 0.61 eV, reflecting the larger size of the silver atom.

The Ag_2C Silver-Carbon Cluster

The lowest energy isomers of Ag_2C cluster are triplets of **E** and **F**. Our calculation using MPW1PW91/SDD shows the **F** (linear) isomer is higher in energy by 0.90 eV. No Ag_2C was observed in our experiments because the highest IR integral intensity for the more stable cyclic isomer **E** is only 4 km/mol and all predicted frequencies are out of the energy range accessible by our FT-IR instrument.

The Ag_2C_2 Silver-Carbon Cluster

The linear AgC_2Ag cluster (**G**), also known as silver acetylide, is the only stable structure found. This species is predicted to appear at 600.3 cm^{-1} with 78 km/mol integral intensity, but is not observed.

The Ag_2C_3 Silver-Carbon Cluster

Three stable C_{2v} isomers were found for Ag_2C_3 ; all are singlets. The *w*-shaped one (**H**) has the lowest energy, and the other two with cyclic structures (**I** and **J**) are less stable by 0.91 and

3.23 eV, respectively. Table 5-1 shows the harmonic vibrational frequencies and integral intensities for all three. The most intense mode predicted for **H** is 1761.1 cm^{-1} (639 km/mol), the asymmetric CC stretch. Although the integral intensities for structures **H**, **I**, and **J** are all very large, we did not observe any bands assignable to these clusters.

Summary

New silver-carbon species were sought by simultaneous dual laser ablation of silver and carbon followed by trapping in solid argon matrices at 12 K. Two new bands were observed at 1827.8 and 1231.6 cm^{-1} . Based on the results of isotopic ^{13}C -substitution experiments and density functional theory calculations with the MPW1PW91/SDD functional/basis set, these two bands were assigned to the asymmetric and symmetric CC stretching modes in the near-linear AgC_3 cluster.

The calculated dissociation energy at the MPW1PW91/SDD level for the *nl*- AgC_3 is 1.77 eV, which is lower by 0.61 eV than in *nl*- CuC_3 . The weaker binding in *nl*- AgC_3 is reflected in its longer metal-carbon bonds compared to the ones in *nl*- CuC_3 .

No photo-induced isotopic scrambling in $^{107}\text{Ag}^{12/13}\text{C}_3$ isotopomers was observed as was found in $\text{Cu}^{12/13}\text{C}_3$, a finding consistent with the fact that no stable cyclic structure of doublet AgC_3 could be found theoretically. Such a structure was previously determined to be essential to the photoscrambling found in CuC_3 .

The equilibrium structures and vibrational frequencies for AgC , AgC_2 , Ag_2C , Ag_2C_2 and Ag_2C_3 were also calculated using MPW1PW91/SDD, but none were observed in our experiments. Though there remain bands unassigned in our spectra, mainly in the $1750 - 1900\text{ cm}^{-1}$ range, it is likely that they are due to larger clusters of AgC_n ($n > 3$).

CHAPTER 6 GOLD-CARBON CLUSTER: STRUCTURE AND INFRARED FREQUENCIES

Introduction

Gold is a classic noble metal and seldom reacts with other molecules or atoms. Therefore, reactions of gold and small molecules are always of great interest. For example, extensive efforts have been made to study the reaction of gold with carbon monoxide due to its potential application in catalysis. The Andrews group has reported $\text{Au}(\text{CO})_n$ ($n=1, 2$) and $\text{Au}(\text{CO})_n^+$ ($n=1-4$) clusters trapped in a neon matrix.¹³⁵ Xu and coworkers further studied the reaction of Au and CO and discovered $\text{Au}_n(\text{CO})$ ($n=1-5$) and $\text{Au}_n(\text{CO})_2$ ($n=1, 2$) clusters.¹³⁶ A photoelectron spectroscopic and quasi-relativistic density functional theory (DFT) study of complexes of the $\text{Au}_6(\text{CO})_n^-$ and $\text{Au}_6(\text{CO})_n$ ($n=0-3$) complexes was reported by Wang *et al.*¹³⁷ Interaction of CO with cationic gold clusters in the gas phase was studied using vibrational spectroscopy by the Rayner group.^{138,139} Recently, Duncan and coworkers produced $\text{Au}^+(\text{CO})_n$ complexes in the gas phase and investigated them using IR photodissociation spectroscopy.¹⁴⁰ Infrared spectra of analogous gold thiocarbonyl complexes, $\text{Au}(\text{CS})_n$ ($n=1, 2$) and Au_2CS were also studied.¹⁴¹ In their investigation of the reactions of gold with hydrogen, Wang *et al.* reported that gold hydride anions are stable.^{94,142} The gold atom is found to be in three different oxidation states in the gold dihalides $\text{AuX}_2^{-/0/+}$ (with $\text{X}=\text{Cl}, \text{Br}$).¹⁴³ Other reactions, such as gold with nitrous oxide, N_2O , were also studied in excess argon using matrix infrared spectroscopy.¹⁴⁴

Our work on copper-carbon and silver-carbon clusters was discussed in the two previous chapters. Since gold is similar in electron configuration to copper and silver, it was of interest to see whether gold reacts similarly with carbon or forms other, more novel molecules or clusters.

Gold-carbon clusters, such as $\text{Au} \equiv \text{C}^+$, $\text{Au}=\text{C}=\text{Au}^{2+}$ and XAuC (where $\text{X} = \text{F}, \text{Cl}, \text{Br}, \text{I}$) have been previously studied theoretically.¹⁴⁵⁻¹⁴⁷ However, experimental work is severely

lacking. To our knowledge, the study of the photodissociation of AuC_n^+ by Duncan and coworkers is the only experimental investigation published to date.¹⁴⁸ In this chapter, we present a vibrational spectroscopic study of a gold-carbon cluster trapped in solid argon at 12 K, also present complementary theoretical work on gold-carbon clusters. The equilibrium geometry, vibrational frequencies and ^{13}C -labeled isotopomer frequencies have been calculated using density functional theory and compared to the experimental values.

Computational and Experimental Details

Experimental Methods

Gold-carbon clusters were generated by two-beam laser ablation of gold and graphite. The experimental apparatus used for the generation and trapping of gold-carbon clusters in solid argon is similar to that used previously for producing copper-carbon clusters and silver-carbon clusters: The output of a pulsed Nd: YAG laser (1064/532 nm, 0.2 – 0.5W, 10Hz) was split into two beams, with one beam focused on a small piece of gold sample (Lesker), and the other beam focused on the graphite sample or a pressed pellet of ^{12}C and ^{13}C (ISOTECH) in the case of the isotopic studies. The reaction products were co-deposited with argon gas onto a 12K CsI window cooled by a closed-cycle helium cryostat (APD Displex). After 2-3 hours deposition, infrared absorption spectra were collected using a NICOLET Magna 560 FT-IR spectrometer (0.5 cm^{-1} resolution). The matrix was annealed to 35 K and recooled to 12 K, and was photolyzed with a medium pressure 100W Hg lamp, to induce secondary reactions.

Computational Methods

Using the Gaussian 03 suite of programs,⁷³ the equilibrium geometries, harmonic vibrational frequencies and dissociation energies were calculated using DFT theory, including the MPW1PW91, BPW91 and B3LYP functional, along with different basis sets. The MPW1PW91 functional, a modified Perdew-Wang exchange and correlation functional,^{74,75} was

used with a SDD basis set.¹³¹ The MPW1PW91 functional was recommended by Wiberg,⁹⁰ Dunbar,⁹¹ and Oomens et al.⁷⁶ for the calculation of C, H, and metal-containing systems. The MPW1PW91 functional was also used in our recent studies of iron complexed with cationic and neutral polycyclic aromatic hydrocarbons.^{72,92} The SDD basis set combines the Stuttgart-Dresden effective core potential (ECP) for gold with the D95V basis set for carbon.¹³¹ In previous work, the SDD basis set was chosen to study the M-NH₃ (M = Cu, Ag) and M⁺-H₂S (M = Cu, Ag, Au) systems.^{132,133} The MPW1PW91/SDD level of theory successfully predicted the ¹³C-labeled isotopomer frequencies in our recent study of the silver-carbon cluster, AgC₃.¹⁴⁹ Since gold, silver and copper atoms have similar electronic configurations (Au([Xe]4f¹⁴5d¹⁰6s¹), Ag([Kr]4d¹⁰5s¹) and Cu([Ar]3d¹⁰4s¹)), we first calculated using the MPW1PW91/SSD level of calculation on the near-linear AuC₃ cluster and compared them to the experimental ¹⁹⁷Au^{12/13}C₃ isotopomer frequencies. The LanL2DZ basis set (D95 on carbon and Los Alamos ECP plus DZ on gold)¹⁵⁰⁻¹⁵² was also used in calculations involving silver and gold.¹³⁵ The MPW1PW91/LanL2DZ method was also tested. We also use the MPW1PW91 with SDDAll (Selects Stuttgart potentials for both gold and carbon atoms) basis set for calculations of the ¹³C-labeled isotopomer frequencies for near-linear AuC₃ clusters.

We also tested the BPW91 functional with SDD and LanL2DZ basis sets on the near-linear AuC₃ cluster. Such a functional has been recommended for calculations of copper, silver, and gold compounds by Wang et. al.⁹⁴ who calculated the reaction products gold with hydrogen using BPW91 density functional, 6-311++G(d,p) basis set for hydrogen and SDD pseudopotentials for the metal atom. In conclusion, we used the BPW91/6-311++G(3df)/SDD pseudopotentials level of theory (6-311++G(3df) for carbon and SDD pseudopotentials for gold).

Finally, different combinations of MPW1PW91, BPW91, B3LYP functional with 6-311++G(3df) basis set for carbon, SDD or LanL2DZ basis sets for gold (without pseudopotentials) were used to calculate ^{13}C -labeled isotopomer frequencies.

Experimental Infrared Spectra

The infrared absorption spectra in the 1250-1300 cm^{-1} and 1750-2200 cm^{-1} range for the species laser-ablated from graphite and for the species formed by the synchronized dual laser ablation of silver and graphite are displayed in Figure 6-1 in panels a and b, respectively. A number of bands observed in spectrum a and b have been previously assigned to the C_3 , C_5 , C_6 , C_7 , C_9 , C_{11} and C_{12} clusters.^{95,96} The 1936.5 cm^{-1} band, assigned to C_6^{\oplus} .⁹⁸ was observed in spectrum b but not in spectrum a. Due to high laser ablation power, impurities such as CO and H_2O are also present.⁸¹ A weak band at 1824.4 cm^{-1} , assigned to C_3H ,^{100,101} was also observed.

Two new bands were observed in spectrum b, at 1845.2 and 1275.7 cm^{-1} . The higher frequency band is about five times more intense than the lower frequency one. Both were found to be dependent on silver and carbon concentrations, and are thus attributed to a species containing both silver and carbon.

In order to determine whether these two bands belong to the same species, a number of experiments were performed under different experimental conditions. First, different Au/C ratios were applied by varying the ablating laser intensities. The two new bands decrease in intensity with lower ablation power and increase with higher power. Second, the intensities of both bands increase by about 25% after matrix annealing up to 35 K and recooling to 12 K. And last, UV-visible photolysis with a medium pressure mercury lamp up to 1 hour decreases both bands about 15%. The integral intensity ratio of the 1845.2 and 1275.7 cm^{-1} bands remained almost constant ($= 7.25 \pm 0.3$) under these different conditions, supporting the conclusion that they belong to the same species.

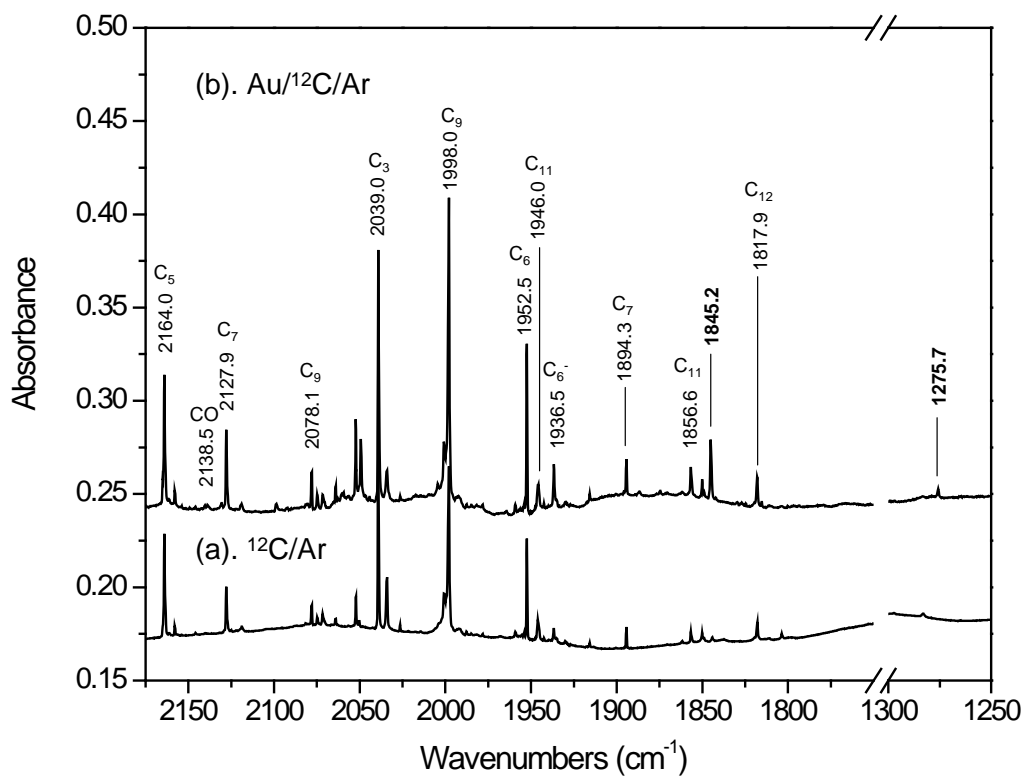


Figure 6-1. Infrared absorption spectra of products of laser ablation of graphite (spectrum a) and products of two-beam laser ablation of graphite and gold (spectrum b). The spectra were recorded after matrix annealing to 35K then cooling back to 12 K. The major bands due to pure carbon clusters and their reaction products with gold at 1845.2 and 1275.7 cm^{-1} are indicated.

Isotopic (^{13}C) substitution experiments were performed again to identify the structure of the unknown species, similar to what was done in the study of copper-carbon clusters and silver-carbon clusters. Figure 6-2 shows the spectrum of the reaction products of the laser ablation of Au and ^{12}C (spectrum a) compared to the spectrum of reaction products of laser ablation of Au and $^{12/13}\text{C}$ mixture (spectrum b). Eight isotopomeric bands (**a** – **h**) built on the 1845.2 cm^{-1} band were clearly observed in the ^{13}C -labeled spectrum. In the lower energy region (1275.7 cm^{-1} band), five very weak bands were also observed. They are here tentatively assigned to various isotopomers (see Table 6-2 through 6-5).

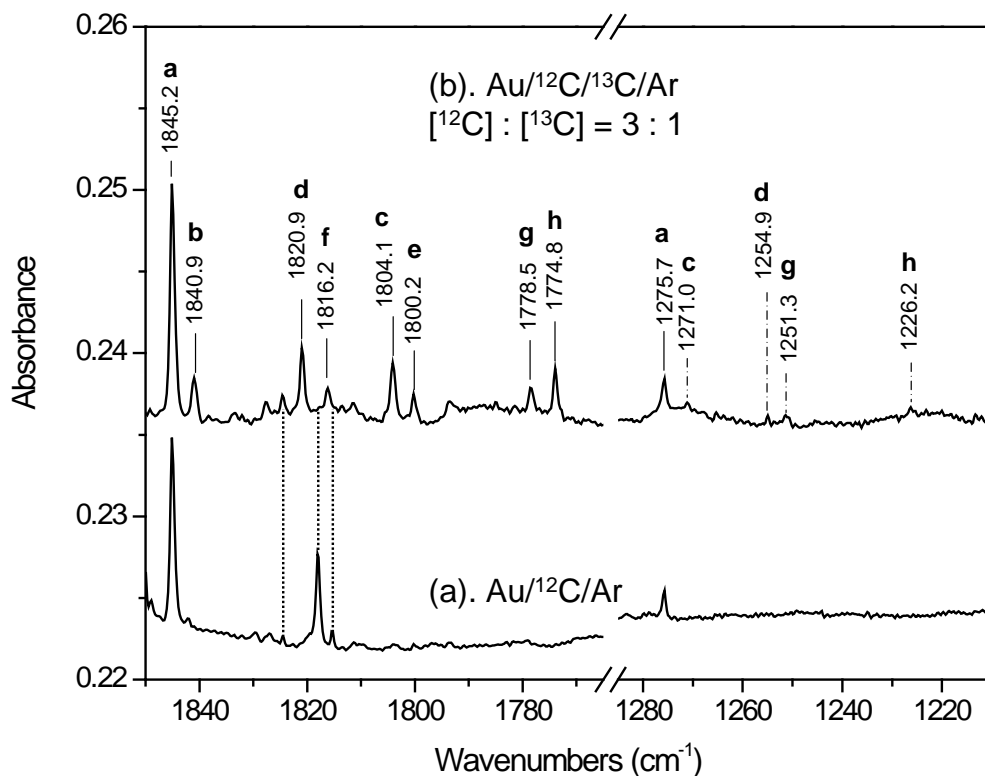


Figure 6-2. Infrared spectra of reaction products from laser ablation of Au and ^{12}C (spectrum a) and from laser ablation of Au and $^{12/13}\text{C}$ (spectrum b). The bands marked by vertical dashed and dotted lines are tentatively assigned to isotomeric partners of the 1275.7 cm^{-1} band. The bands marked by vertical dotted lines are due to: C_3H (1824.4 cm^{-1}),^{100,101} C_{12} (1817.9 cm^{-1}),¹⁰³

Figure 6-3 shows the infrared spectra of reaction products from laser ablation of Cu and $^{12/13}\text{C}$ (spectrum a), Ag and $^{12/13}\text{C}$ (spectrum b) and Au and $^{12/13}\text{C}$ (spectrum c) in the $1750\text{--}1850\text{ cm}^{-1}$ energy region, showing very similar isotopomer band patterns with only small energy shifts. We note that similar isotopomer band pattern was also previously observed for the near-linear $^{12/13}\text{C}_3\cdot\text{H}_2\text{O}$ complex,¹⁰⁴ and the linear $^{12/13}\text{C}_3\text{Cr}$ and $^{12/13}\text{C}_3\text{Co}$ clusters.^{81,83} Such a band pattern is characteristic of the $\text{C}=\text{C}$ asymmetric stretch mode in $^{12/13}\text{C}_3$ with its one end bonded to the ligand in a near-linear or linear cluster geometry. This strongly suggests that the 1845.2 cm^{-1}

band should be assigned to the CC asymmetric stretching mode in linear or near-linear $^{12/13}\text{C}_3$ isotopomers bonded at one end to Au.

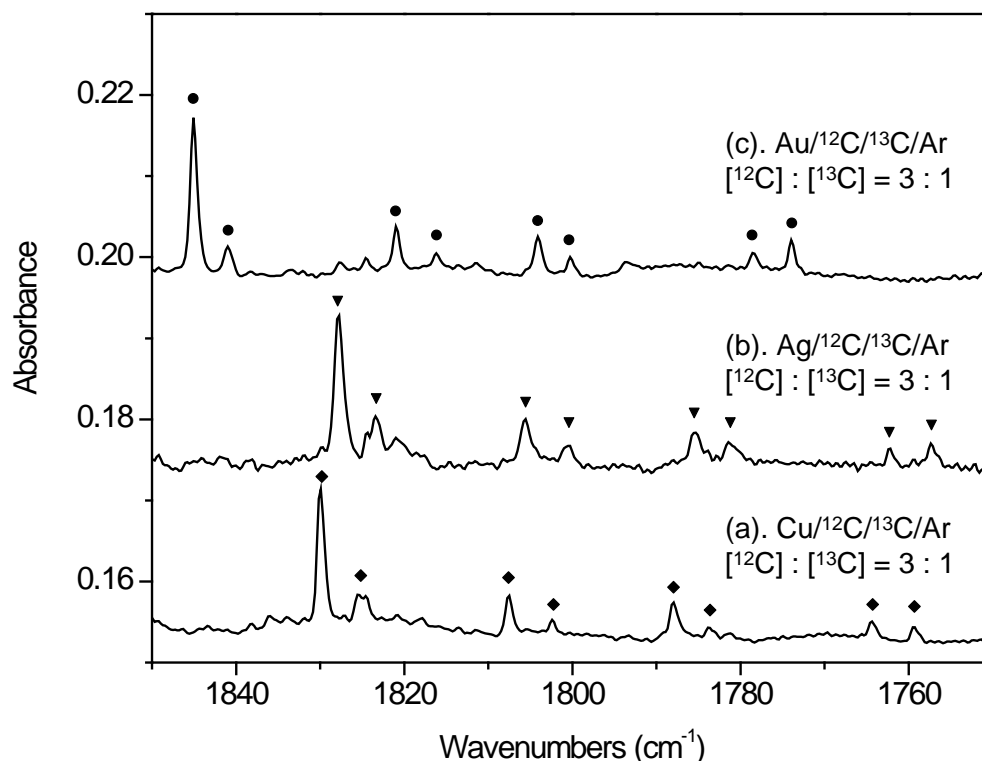


Figure 6-3. Infrared spectra of reaction products from laser ablation of Cu and $^{12/13}\text{C}$ (spectrum a), Ag and $^{12/13}\text{C}$ (spectrum b) and Au and $^{12/13}\text{C}$ (spectrum c) in 1750-1850 cm^{-1} region. The bands marked are assigned to isotopomeric bands for $\text{Cu}^{12/13}\text{C}_3$, $\text{Ag}^{12/13}\text{C}_3$ and $\text{Au}^{12/13}\text{C}_3$.

After inspection of the ^{13}C -labelled spectra of Figure 6-2, we discuss why the lower frequency mode (1275.7 cm^{-1} band) we see only five isotopomer bands (labeled a, c, d, g and h), while there are eight isotopomeric bands in the higher energy region (1845.2 cm^{-1}). Since the intensity of the band at 1275.7 cm^{-1} is about one-fifth of the 1845.2 cm^{-1} band, it is expected that the intensities of the isotopomer bands built on the 1275.7 cm^{-1} band will also be about one-fifth of those built on 1845.2 cm^{-1} band. But the isotopomer bands b, f, e are already very small.

Therefore, the absence of the isotopomer bands in the lower frequency region is understandable. In the next section, we discuss the agreement between the experimental results and theoretical calculation.

When gold bonds to either end of the same singly substituted isotopic precursor, i.e., $^{12/13}\text{C}_3$ (12-12-**13**), **b** (197-12-12-**13**) and **d** (197-**13**-12-12) isotopomers are formed. Figure 6-2 shows that the **b** and **d** bands have comparable intensities, as expected. Similarly, when Au attaches to the C_3 (12-**13**-**13**) precursor, **e** (107-12-**13**-**13**) and **g** (107-**13**-**13**-12) isotopomers are formed. Again, Figure 6-2 shows that the **e** and **g** bands have similar intensities. This is consistent with our previous study of AgC_3 , which indicates that no photo-induced isotopic scrambling takes place in AuC_3 .¹⁴⁹

Theoretical Calculations for Gold-Carbon AuC_3 Cluster

The near-linear structure is the only stable structure found for the AuC_3 cluster, as displayed in Figure 6-4. The bond lengths and angles calculated using MPW1PW91/SDD and MPW1PW91/LanL2DZ functional/basis sets are marked in the figure. The near-linear AuC_3 cluster has a doublet spin multiplicity. Predicted vibrational frequencies (unscaled) and intergral intensities for near-linear AuC_3 using different functional/basis sets are listed in Table 6-1. For all calculations, the most intense band is in $1850\text{-}1900\text{ cm}^{-1}$ region (asymmetric C=C stretch mode); A much weaker band is predicted in the 1200 cm^{-1} region. This is consistent with our experimental data: a strong band appears at 1845.2 cm^{-1} and a weaker band at 1275.7 cm^{-1} . The intensity ratio of the two bands is relatively high (20.4-92.3) compared to experiment value (7.25) independent of the functional/basis sets used. The MPW1PW91/SDD, MPW1PW91/LanL2DZ and MPW1PW91/SDDAll functional/basis sets gave the best predictions of the relative intensity ratio of the two bands (29.1, 23.6 and 20.4, respectively). The BPW91/6-311++G(3df)/SDD(pseudopotential) level of calculation gave the worst results (92.3).

Table 6-1. Vibrational frequencies (cm^{-1}) and integral intensities (km/mol) for electronic ground states of near-linear AuC_3 clusters (displayed in Figure 6-4), calculated using different functional/basis sets.

Functional/basis sets	Near-linear AuC_3 (X^2A')
MPW1PW91/SDD	a' 1911.6 (204), a' 1264.3 (7), a' 511.7 (36), a' 356.7 (2), a'' 266.7 (4), a' 138.5 (4)
MPW1PW91/LanL2DZ	a' 1916.4 (212), a' 1271.4 (9), a' 525.0 (45), a' 368.0 (3), a'' 273.6 (4), a' 141.9 (6)
MPW1PW91/SDDALL	a' 1960.3 (204), a' 1280.7 (10), a' 501.1 (34), a' 343.1 (4), a'' 229.8 (3), a' 135.9 (3)
BPW91/SDD	a' 1885.0 (343), a' 1218.4 (4), a' 515.4 (16), a' 337.8 (2), a'' 230.5 (4), a' 132.8 (0)
BPW91/LanL2DZ	a' 1889.5(326), a' 1227.2 (6), a' 531.9 (26), a' 350.5 (2), a'' 240.0 (4), a' 137.9 (1)
MPW1PW91/ 6-311++G(3df)/SDD	a' 1943.1 (252), a' 1297.8 (5), a' 523.7 (33), a' 343.9 (6), a'' 195.1 (9), a' 137.6 (3)
MPW1PW91/ 6-311++G(3df)/LanL2DZ	a' 1941.8 (268), a' 1299.4 (5), a' 523.5 (38), a' 343.4 (7), a'' 202.1 (9), a' 141.0 (4)
BPW91/ 6-311++G(3df)/SDD(pseudo)	a' 1922.8 (369), a' 1254.3 (4), a' 527.0 (21), a' 328.3 (4), a'' 173.1 (9), a' 131.6 (1)
B3LYP/ 6-311++G(3df)/LanL2DZ	a' 1949.9 (315), a' 1286.4 (7), a' 513.9 (34), a' 336.7 (4), a'' 208.2 (9), a' 135.4 (2)

We also calculated the ^{13}C -labeled isotopomer frequencies for the near-linear AuC_3 cluster using all the functional/basis sets mentioned above. The comparison between the observed isotopomer bands and the predicted (scaled) near-linear $^{197}\text{Au}^{12/13}\text{C}_3$ frequencies are listed in Tables 6-2 through 6-5. In the silver-carbon clusters and copper-carbon clusters, calculations with the MPW1PW91/SDD level of theory showed good agreement with experimental data. However, none of the calculation methods predict ^{13}C -labeled isotopomer frequencies for the near-linear AuC_3 cluster very well.

The MPW1PW91/SDD, MPW1PW91/LanL2DZ functional/basis sets give relatively good results. But the maximum differences between experimental and predicted isotopomer frequencies, $\nu_{\text{exp}} - \omega_{\text{sc}}$, are 7.0 cm^{-1} for MPW1PW91/SDD and 6.3 cm^{-1} for MPW1PW91/LanL2DZ, which is still too large to be accepted. Typical value of $\nu_{\text{exp}} - \omega_{\text{sc}}$ is usually within 2.0 cm^{-1} . Using different basis sets on carbon atom and gold atom does not help

either, as the maximum differences between experimental and predicted isotopomer frequencies, $\nu_{\text{exp}} - \omega_{\text{sc}}$, are 9.7 cm^{-1} for MPW1PW91/6-311++G(3df)/SDD and 9.6 cm^{-1} for MPW1PW91/6-311++G(3df)/LanL2DZ, which is an even worse prediction.

Table 6-2. Comparison of Experimental and Calculated (at BPW91/SDD and BPW91/LanL2DZ level) Isotopomer Frequencies (Integral Intensities) for the Asymmetric C=C Stretch and Symmetric C=C Stretch Fundamental Modes of Near Linear $^{197}\text{Au}^{12/13}\text{C}$.

X	Isotopomer	ν_{exp} / cm^{-1}	$\omega_{\text{sc}}^{\text{a}}$ / cm^{-1}	$\nu_{\text{exp}} - \omega_{\text{sc}}$ / cm^{-1}	$\omega_{\text{sc}}^{\text{b}}$ / cm^{-1}	$\nu_{\text{exp}} - \omega_{\text{sc}}$ / cm^{-1}
Asymmetric C=C Stretch Mode						
a	197-12-12-12	1845.2	1845.2 (343)	0.0	1845.2 (326)	0.0
b	197-12-12- 13	1840.9	1837.0 (339)	3.9	1837.4 (322)	3.5
c	197-12- 13 -12	1804.1	1798.9 (329)	5.2	1799.3 (313)	4.8
d	197- 13 -12-12	1820.9	1828.6 (336)	-7.7	1827.9 (317)	-7.0
e	197-12- 13 - 13	1800.2	1790.7 (325)	9.5	1791.5 (309)	8.7
f	197- 13 -12- 13	1816.3	1819.7 (332)	-3.4	1819.4 (314)	-3.1
g	197- 13 - 13 -12	1778.6	1781.6 (321)	-3.0	1781.2 (304)	-2.6
h	197- 13 - 13 - 13	1773.8	1772.6 (317)	1.2	1772.6 (301)	1.2
Symmetric C=C Stretch Mode						
a	197-12-12-12	1275.7	1275.7 (4)	0.0	1275.7 (6)	0.0
b	197-12-12- 13		1251.8 (4)		1251.9 (5)	
c	197-12- 13 -12	1271.1	1274.4 (4)	-3.3	1274.2 (5)	-3.1
d	197- 13 -12-12	1254.9	1250.0 (4)	4.9	1250.1 (6)	4.8
e	197-12- 13 - 13		1250.0 (4)		1250.0 (5)	
f	197- 13 -12- 13		1226.7 (4)		1226.8 (5)	
g	197- 13 - 13 -12	1251.3	1249.3 (4)	2.0	1249.3 (6)	2.0
h	197- 13 - 13 - 13	1226.2	1225.5 (3)	0.7	1225.6 (5)	0.6

^a Frequencies are scaled uniformly by scaling factor of 0.9788 for asymmetric mode and by 1.0470 for symmetric mode.

^b Frequencies are scaled uniformly by scaling factor of 0.9765 for asymmetric mode and by 1.0395 for symmetric mode.

The Andrews group used the BPW91 density functional, and 6-311++G(d,p) for hydrogen and SDD pseudopotentials for gold to successfully calculate the gold hydrides, AuH_n , and their anions. However, a similar level of theory, BPW91/6-311++G(3df)/SDD (pseudopotential) gave the worst results in our study of the near-linear AuC_3 clusters. The maximum difference between experimental and predicted isotopomer frequencies, $\nu_{\text{exp}} - \omega_{\text{sc}}$, is as large as 11.5 cm^{-1} .

Table 6-3. Comparison of Experimental and Calculated (at MPW1PW91/SDD, MPW1PW91/SDDAll and MPW1PW91/LanL2DZ level) Isotopomer Frequencies (Integral Intensities) for the Asymmetric C=C Stretch and Symmetric C=C Stretch Fundamental Modes of Near Linear $^{197}\text{Au}^{12/13}\text{C}$.

X	Isotopomer	ν_{exp} /cm ⁻¹	$\omega_{\text{sc}}^{\text{a}}$	$\nu_{\text{exp}} - \omega_{\text{sc}}$	$\omega_{\text{sc}}^{\text{b}}$	$\nu_{\text{exp}} - \omega_{\text{sc}}$	$\omega_{\text{sc}}^{\text{c}}$	$\nu_{\text{exp}} - \omega_{\text{sc}}$
			/cm ⁻¹	/cm ⁻¹	/cm ⁻¹	/cm ⁻¹	/cm ⁻¹	/cm ⁻¹
			MPW1PW91/SDD		MPW1PW91/SDDALL		MPW1PW91/LanL2DZ	
Asymmetric C=C Stretch Mode								
a	197-12-12-12	1845.2	1845.2 (204)	0.0	1845.2 (180)	0.0	1845.2 (212)	0.0
b	197-12-12-13	1840.9	1838.5 (202)	2.4	1838.3 (178)	2.6	1838.8 (210)	2.1
c	197-12-13-12	1804.1	1799.7 (194)	4.4	1799.4 (171)	4.7	1800.1 (210)	4.0
d	197-13-12-12	1820.9	1826.4 (200)	-5.5	1826.8 (175)	-5.9	1825.7 (207)	-4.8
e	197-12-13-13	1800.2	1793.2 (192)	7.0	1792.6 (170)	7.6	1793.9 (200)	6.3
f	197-13-12-13	1816.3	1819.0 (198)	-2.7	1819.3 (174)	-3.0	1818.6 (205)	-2.3
g	197-13-13-12	1778.6	1779.9 (190)	-1.3	1780.2 (167)	-1.6	1779.6 (197)	-1.0
h	197-13-13-13	1773.8	1772.6 (188)	1.2	1772.6 (166)	1.2	1772.6 (195)	1.2
Symmetric C=C Stretch Mode								
a	197-12-12-12	1275.7	1275.7 (7)	0.0	1275.7 (10)	0.0	1275.7 (9)	0.0
b	197-12-12-13		1250.5 (7)		1250.2 (10)		1250.6 (8)	
c	197-12-13-12	1271.1	1274.0 (7)	-2.9	1274.1 (10)	-3.0	1273.8 (9)	-2.7
d	197-13-12-12	1254.9	1251.9 (7)	3.0	1251.8 (10)	3.1	1252.0 (8)	2.9
e	197-12-13-13		1248.2 (7)		1248.2 (10)		1248.0 (9)	
f	197-13-12-13		1227.2 (7)		1226.9 (9)		1227.3 (8)	
g	197-13-13-12	1251.3	1250.8 (7)	0.5	1250.8 (10)	0.5	1250.7 (8)	0.6
h	197-13-13-13	1226.2	1225.6 (7)	0.6	1225.5 (9)	0.7	1225.6 (8)	0.6

^a Frequencies are scaled uniformly by scaling factor of 0.9653 for asymmetric mode and by 1.0090 for symmetric mode.

^b Frequencies are scaled uniformly by scaling factor of 0.9413 for asymmetric mode and by 0.9961 for symmetric mode.

^c Frequencies are scaled uniformly by scaling factor of 0.9628 for asymmetric mode and by 1.0034 for symmetric mode.

Table 6-4. Comparison of Experimental and Calculated (at MPW1PW91/6-311++G(3df)/SDD and MPW1PW91/6-311++G(3df)/LanL2DZ level) Isotopomer Frequencies (Integral Intensities) for the Asymmetric C=C Stretch and Symmetric C=C Stretch Fundamental Modes of Near Linear $^{197}\text{Au}^{12/13}\text{C}$.

X	Isotopomer	ν^{exp} /cm ⁻¹	$\omega_{\text{sc}}^{\text{a}}$	$\nu^{\text{exp}} - \omega_{\text{sc}}$	$\omega_{\text{sc}}^{\text{b}}$	$\nu^{\text{exp}} - \omega_{\text{sc}}$
			/cm ⁻¹	/cm ⁻¹	/cm ⁻¹	/cm ⁻¹
			MPW1PW91/ 6-311++G(3df)/SDD	MPW1PW91/ 6-311++G(3df)/LanL2DZ		
Asymmetric C=C Stretch Mode						
a	197-12-12-12	1845.2	1845.2 (252)	0.0	1845.2 (268)	0.0
b	197-12-12- 13	1840.9	1837.1 (250)	3.8	1837.2 (265)	3.7
c	197-12- 13 -12	1804.1	1798.6 (240)	5.5	1798.7 (255)	5.4
d	197- 13 -12-12	1820.9	1828.9 (247)	-8.0	1828.8 (262)	-7.9
e	197-12- 13 - 13	1800.2	1790.5 (237)	9.7	1790.8 (252)	9.6
f	197- 13 -12- 13	1816.3	1820.0 (245)	-3.7	1820.0 (260)	-3.7
g	197- 13 - 13 -12	1778.6	1781.5 (235)	-2.9	1781.4 (249)	-2.8
h	197- 13 - 13 - 13	1773.8	1772.6 (233)	1.2	1772.6 (247)	1.2
Symmetric C=C Stretch Mode						
a	197-12-12-12	1275.7	1275.7 (5)	0.0	1275.7 (5)	0.0
b	197-12-12- 13		1251.0 (5)		1251.1 (5)	
c	197-12- 13 -12	1271.1	1274.5 (5)	-3.4	1274.5 (5)	-3.4
d	197- 13 -12-12	1254.9	1250.6 (5)	4.3	1250.7 (5)	4.2
e	197-12- 13 - 13		1249.5 (5)		1249.5 (5)	
f	197- 13 -12- 13		1226.6 (5)		1226.6 (5)	
g	197- 13 - 13 -12	1251.3	1249.9 (5)	1.4	1250.0 (5)	1.3
h	197- 13 - 13 - 13	1226.2	1225.6 (5)	0.6	1225.5 (5)	0.7

^a Frequencies are scaled uniformly by scaling factor of 0.9496 for asymmetric mode and by 0.9830 for symmetric mode.

^b Frequencies are scaled uniformly by scaling factor of 0.9503 for asymmetric mode and by 0.9818 for symmetric mode.

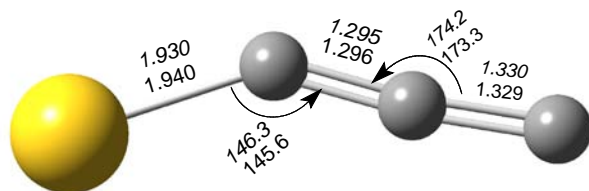


Figure 6-4. Optimized equilibrium structure for the AuC₃ cluster. The bond lengths (Å) and angles (°) calculated at MPW1PW91/LanL2DZ (italic type, top) and at MPW1PW91/SDD (normal type) are marked.

Overall, the results calculated with MPW1PW91 functional are better than those with BPW91 or B3LYP functional. Therefore, we believe that MPW1PW91 is still a better method

when dealing with heavy metals, such as copper, silver and gold. To get better results of ^{13}C -labeled isotopomer frequencies, an improved basis set than either the SDD and LanL2DZ or the application of relativistic methods is apparently needed.

Table 6-5. Comparison of Experimental and Calculated (at BPW91/6-311++G(3df)/SDD (pseudopotential) and B3LYP/6-311++G(3df)/LanL2DZ level) Isotopomer Frequencies (Integral Intensities) for the Asymmetric C=C Stretch and Symmetric C=C Stretch Fundamental Modes of Near Linear $^{197}\text{Au}^{12/13}\text{C}$.

X	Isotopomer	ν_{exp} /cm ⁻¹	$\omega_{\text{sc}}^{\text{a}}$ /cm ⁻¹	$\nu_{\text{exp}} - \omega_{\text{sc}}$ /cm ⁻¹	$\omega_{\text{sc}}^{\text{b}}$ /cm ⁻¹	$\nu_{\text{exp}} - \omega_{\text{sc}}$ /cm ⁻¹
Asymmetric C=C Stretch Mode						
a	197-12-12-12	1845.2	1845.2 (369)	0.0	1845.2 (315)	0.0
b	197-12-12- 13	1840.9	1835.8 (365)	5.1	1836.4 (312)	4.5
c	197-12- 13 -12	1804.1	1798.2 (353)	5.9	1798.3 (301)	5.8
d	197- 13 -12-12	1820.9	1830.5 (360)	-9.6	1829.9 (307)	-9.0
e	197-12- 13 - 13	1800.2	1788.7 (349)	11.5	1789.5 (298)	10.7
f	197- 13 -12- 13	1816.3	1820.4 (357)	-4.1	1820.3 (305)	-4.0
g	197- 13 - 13 -12	1778.6	1782.9 (344)	-4.3	1782.3 (293)	-3.7
h	197- 13 - 13 - 13	1773.8	1772.7 (341)	1.1	1772.6 (290)	1.2
Symmetric C=C Stretch Mode						
a	197-12-12-12	1275.7	1275.7 (4)	0.0	1275.7 (7)	0.0
b	197-12-12- 13		1252.2 (4)		1251.2 (6)	
c	197-12- 13 -12	1271.1	1274.7 (4)	-3.6	1274.8 (7)	-3.7
d	197- 13 -12-12	1254.9	1249.4 (4)	5.5	1250.2 (7)	4.7
e	197-12- 13 - 13		1250.9 (4)		1249.9 (4)	
f	197- 13 -12- 13		1226.5 (4)		1226.3 (7)	
g	197- 13 - 13 -12	1251.3	1248.6 (4)	2.7	1249.6 (7)	1.7
h	197- 13 - 13 - 13	1226.2	1225.6 (4)	0.6	1225.5 (6)	0.7

^a Frequencies are scaled uniformly by scaling factor of 0.9596 for asymmetric mode and by 1.0171 for symmetric mode.

^b Frequencies are scaled uniformly by scaling factor of 0.9463 for asymmetric mode and by 0.9917 for symmetric mode.

Summary

A new gold-carbon species was produced by simultaneous dual laser ablation of gold and carbon, followed by trapping in solid argon matrices at 12 K. Two new bands were observed at 1845.2 and 1275.7 cm⁻¹. The ^{13}C -isotopic labeling experiments show that these two bands have a very similar isotopomer band pattern compared to the near-linear AgC₃ cluster and CuC₃ cluster.

Therefore, these two bands are concluded to be due to the asymmetric and symmetric CC stretching modes in the near-linear AuC₃ cluster.

The predictions of ¹³C-labeled isotopomer frequencies for the near-linear AuC₃ cluster of using density functional theory calculations do not match the experimental data very well. Calculation with MPW1PW91/SDD, MPW1PW91/LanL2DZ functional/basis sets gave relatively better results, but they are still not with an acceptable range.

No photo-induced isotopic scrambling in ¹⁹⁷Au^{12/13}C₃ isotopomers was observed, a similar finding with the study of Ag^{12/13}C₃, which is consistent with the fact that no stable cyclic structure of doublet AuC₃ could be found theoretically. Such a structure was previously determined to be essential to the photoscrambling found in near-linear Cu^{12/13}C₃ cluster.

CHAPTER 7 CONCLUSIONS AND FUTURE WORK

The presence of polycyclic aromatic hydrocarbons (PAHs) and their cations, and carbon clusters in the interstellar medium is now widely accepted. Metals, such as iron and copper are also present in the interstellar space. However, very little research has been done on the reaction of metals with these astrophysical species. In this work, we studied the reaction products of iron with polycyclic aromatic hydrocarbons, and metals with carbon clusters using matrix isolation spectroscopy along with theoretical calculations.

Iron and PAH Complexes

Infrared absorption spectra of neutral complexes of iron with benzene, naphthalene, fluorene, pyrene, and coronene in solid Ar at 12K have been obtained. Supporting calculations of the equilibrium geometries, stabilities, and harmonic vibrational frequencies of these complexes have been carried out using density functional theory (MPW1PW91/6-31+G(d,p) method) using a modified Perdew-Wang exchange and correlation functional/basis set. Our results indicate that the spin multiplicities of the complexes' electronic ground states are triplets. The calculations show that the iron atom is situated over the six-membered carbon ring of the polycyclic aromatic hydrocarbon (PAH) ligand. Calculated dissociation energies (D_0) range from 0.52 eV for Fe(coronene) to 2.06 eV for Fe(fluorene). All are substantially less tightly bound than their cationic counterparts. Cationic Fe(PAH) complexes are therefore thought to be more plausible candidates for the carriers of the unidentified interstellar infrared (UIR) emission bands.

Metal Carbon Clusters

Copper-carbon clusters, silver-carbon clusters and gold-carbon clusters were formed by dual Nd/YAG laser vaporization of metal and carbon targets, trapped in solid Ar at 12K and investigated by infrared spectroscopy. Density functional (DFT) calculations of a number of

possible molecular structures for Cu, Ag and Au carbon clusters have been performed and their associated vibrational harmonic mode frequencies and dissociation energies were determined. ^{13}C -isotopic substitution experiments were performed to assist the identification of the new bands observed in each experiment.

Two new bands at 1830.0 and 1250.5 cm^{-1} were observed in the copper-carbon experiments. They were assigned to the asymmetric and symmetric C=C stretching modes, respectively, in the near-linear CuC_3 (X^2A') cluster. This assignment was supported by the DFT calculation at the MPW1PW91/6-311++G(3df) level and by ^{13}C -isotopic substitution experiments. The MPW1PW91/6-311++G(3df) level of calculation successfully predicts the relative integral intensities and the ^{13}C -labeled isotopomer frequencies for these modes while the B3LYP/6-311++G(3df) approach failed to do so.

In the study of the silver-carbon system, we observed two extra bands at 1827.8 and 1231.6 cm^{-1} . Based on the results of isotopic ^{13}C -substitution experiments and density functional theory calculations with the MPW1PW91/SDD functional/basis set, these two bands were assigned to the asymmetric and symmetric CC stretching modes in the near-linear AgC_3 cluster. The results of calculation at MPW1PW91/SDD and B3LYP/SDD level were compared to the experimental data. Again, the MPW1PW91/SDD method made better predictions on both relative integral intensities and the ^{13}C -labeled isotopomer frequencies for the two modes. Therefore, we believed that MPW1PW91 is a better method when dealing with metal-containing systems.

After dual ablation and trapping of gold and carbon in the argon matrix, new infrared absorption bands were observed at 1845.2 and 1275.7 cm^{-1} . A new gold-carbon species was believed to be responsible for the two new bands. The ^{13}C -isotopic labeling experiments showed

that these two bands have similar isotopomer band pattern compared to the near-linear assigned AgC_3 cluster and CuC_3 cluster. Therefore, these two bands are very likely due to the asymmetric and symmetric CC stretching modes in the near-linear AuC_3 cluster. However, the density functional calculation using MPW1PW91, B3LYP and BPW91 functional, along with SDD, LanL2DZ or using different basis sets on gold and carbon atom, all failed to predict the ^{13}C -labeled isotopomer frequencies for the two bands. Hence, the assignment of the two new bands is tentative.

Many pure carbon clusters larger than C_3 were formed in the metal (Cu, Ag, Au)-carbon experiments. There are a number of bands left unassigned in the spectra, mainly in the 1700-1900 cm^{-1} region. These bands are likely due to the products of reactions of larger carbon clusters with metal. Although efforts were made to produce and identify the copper and longer carbon chain clusters, none could be determined unequivocally due to the experimental difficulty of ^{13}C -isotopic labeling of larger carbon clusters (i.e., too low intensities for the isotopomeric bands).

Photo-induced $^{12/13}\text{C}$ isotopic scrambling in $\text{Cu}^{12/13}\text{C}_3$ clusters has also been observed. The potential energy surface (PES) of the isomerization reaction for the near-linear CuC_3 cluster was plotted using the MPW1PW91/6-311++G(3df) level of theory. The mechanism for the photoscrambling is shown to involve the formation of a bicyclic CuC_3 isomer. However, no photo-induced isotopic scrambling was observed in the near-linear AgC_3 clusters or AuC_3 clusters, probably because no stable cyclic structure of AgC_3 and AuC_3 is possible. Such a structure was found to be essential to the photoscrambling procedure found in CuC_3 .

Future Work

The possible contribution of various PAH^+ cations to the unidentified interstellar infrared emission bands (UIRs) has been well established in previous work. But comparable broad studies

of Metal (PAH)⁺ complexes are not yet available. In future work such studies could be extended for the most abundant interstellar metals, such as Al, Ni, and Cu. To differentiate between the various metal-PAH cationic complexes deposited in the rare-gas matrix, one could mass-select them to deposition. Figure 7-1 shows such apparatus.

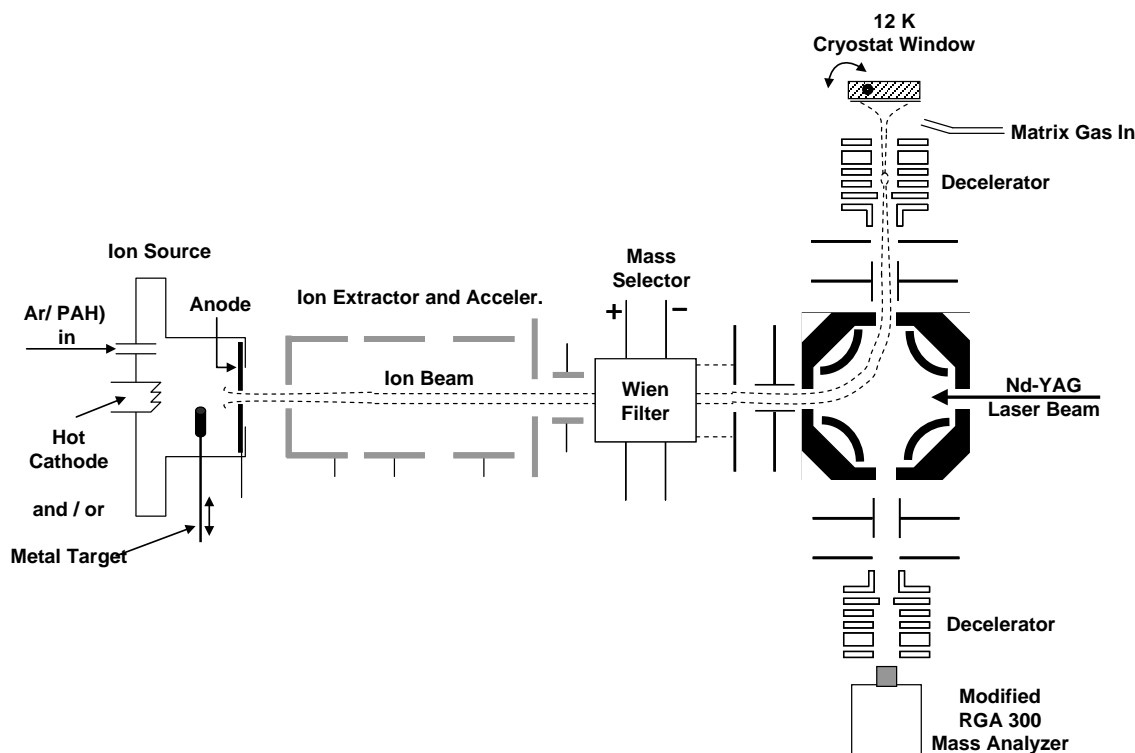


Figure 7-1. Experimental Setup for Ion Mass Selection and Trapping.

The PAH will be sublimed into the ion source, the high repetition Nd/YAG laser will be used to ablate and ionize a metal which will react with PAHs in the ion source. The metal ions will collide with sublimed neutral PAHs forming cationic metal-PAH⁺ complexes. After extraction in the ion extractor, the Metal-PAH⁺ beam will be passed through the mass selector ($\Delta m/m = 400$), the ionic PAH fragments will be turned + 90° with a quadrupole turner, decelerated, and then mass analyzed with a modified RGA 300 Mass Analyzer. Once the mass signal of the desired fragment has been optimized, the quad turner will be set to direct the beam in the - 90° direction where it will be deposited with the matrix gas on a rotatable cryostat sample

window. Although neutral complexes may also form, their trajectory will be different from the ionic complex beam; they will not be focused by the einzel lenses in the ion extractor and will not be turned by the quad turner. Mass analysis will again be performed and after redirection toward the cryostat window, deposition in a matrix will occur. Ne matrices will be used since these matrices perturb electronic transitions less than other matrices. Depending on the ion currents achievable we anticipate that lengthy depositions will probably be necessary to collect enough material for spectral studies. Infrared absorption spectra for ions deposited will be scanned using modified MIDAC FT-IR spectrometer in reflection mode. Such an experimental apparatus can also be used to study the reactions of metal with the fragments of the PAHs. These kinds of reactions could possibly occur in the interstellar space. The PAHs could potentially be fragmented by cosmic radiation.

Other future work would be to further study the interaction of metals with longer carbon chain clusters. Argon and nitrogen matrices were used in the present work, and did not produce large enough amounts of metal-longer carbon clusters. An “overcoating” approach could be tried. First, metal and carbon clusters will be formed by dual laser ablation and trapped in an argon matrix as usual. Then krypton gas will be introduced to the chamber and form a “top coat” on the already-formed matrix. Since krypton has a higher melting point than argon, the matrices can be maintained when annealed to a higher temperature. A lot of longer carbon chain cluster will form during the annealing process, thus increasing the chances of metal atom bonding to the longer carbon chain clusters. Once large signals of ^{12}C metal-carbon clusters are obtained, the ^{13}C -labeling isotopic experiments can be performed to assist in the identification of the molecules.

LIST OF REFERENCES

- (1) Ehrenfreund, P.; Charnley, S. B. *Annu. Rev. Astron. Astrophys.* **2000**, *38*, 427.
- (2) Schmidt, T.; Sharp, R. G. *Aust. J. Chem.* **2005**, *58*, 69.
- (3) Gillett, F. C.; Forrest, W. J.; Merrill, K. M. *Astrophys. J.* **1973**, *183*, 87.
- (4) Russell, R. W.; Soifer, B. T.; Willner, S. P. *Astrophys. J.* **1977**, *217*, L149.
- (5) Russell, R. W.; Soifer, B. T.; Willner, S. P. *Astrophys. J.* **1978**, *220*, 568.
- (6) Merrill, P. W. *Astrophys. J.* **1934**, *79*, 183.
- (7) Merrill, P. W. *Astrophys. J.* **1936**, *83*, 126.
- (8) University of New Hampshire Experimental Space Plasma Group. *The Interstellar Medium: an online tutorial*; <http://www-ssg.sr.unh.edu/ism/intro.html> 08/2008.
- (9) Ehrenfreund, P.; Krafft, C.; Kochan, H.; Pirronello, V. *Laboratory Astrophysics and Space Research*; Kluwer Academic Publishers, 1999.
- (10) Ferriere, K. M. *Rev. Mod. Phys.* **2001**, *73*, 1031.
- (11) NASA The Cosmic Ice Laboratory. *Interstellar Molecules*; <http://www-691.gsfc.nasa.gov/cosmic.ice.lab/interstellar.htm> 06/2008.
- (12) Swings, P.; Rosenfeld, L. *Astrophys. J.* **1937**, *86*, 483.
- (13) Kuan, Y. J.; Charnley, S. B.; Huang, H. C.; Tseng, W. L.; Kisiel, Z. *Astrophysical Journal* **2003**, *593*, 848.
- (14) Snyder, L. E.; Lovas, F. J.; Hollis, J. M.; Friedel, D. N.; Jewell, P. R.; Remijan, A.; Ilyushin, V. V.; Alekseev, E. A.; Dyubko, S. F. *Astrophysical Journal* **2005**, *619*, 914.
- (15) Wilson, E. *Chemical & Engineering News* **2005**, *83*, 44.
- (16) Tielens, A. G. G. M.; Hony, S.; Van Kerckhoven, C.; Peeters, E. Interstellar and circumstellar PAHs. In *European Space Agency, [Special Publication] SP*, 1999; Vol. SP-427; pp 579.
- (17) Leger, A.; Puget, J. L. *Astron. Astrophys.* **1984**, *137*, L5.
- (18) Allamandola, L. J.; Tielens, A. G. G. M.; Barker, J. R. *Astrophys. J.* **1985**, *290*, L25.
- (19) Szczepanski, J.; Vala, M. *Nature* **1993**, *363*, 699.

- (20) Allamandola, L. J.; Hudgins, D. M.; Sandford, S. A. *Astrophys. J.* **1999**, *511*, L115.
- (21) Szczepanski, J.; Fuller, J.; Ekern, S.; Vala, M. *Spectrochim. Acta, Part A* **2001**, *57*, 775.
- (22) Allamandola, L. J.; Hudgins, D. M.; Bauschlicher, C. W.; Langhoff, S. R. *Astron. Astrophys.* **1999**, *352*, 659.
- (23) Hinkle, K. W.; Keady, J. J.; Bernath, P. F. *Science* **1988**, *241*, 1319.
- (24) Bernath, P. F.; Hinkle, K. H.; Keady, J. J. *Science* **1989**, *244*, 562.
- (25) Leger, A.; Dhendecourt, L. *Astron. Astrophys.* **1985**, *146*, 81.
- (26) Ruffle, D. P.; Bettens, R. P. A.; Terzieva, R.; Herbst, E. *Astrophys. J.* **1999**, *523*, 678.
- (27) McCarthy, M. C.; Gottlieb, C. A.; Gupta, H.; Thaddeus, P. *Astrophys. J.* **2006**, *652*, L141.
- (28) Brunken, S.; Gupta, H.; Gottlieb, C. A.; McCarthy, M. C.; Thaddeus, P. *Astrophys. J.* **2007**, *664*, L43.
- (29) Remijan, A. J.; Hollis, J. M.; Lovas, F. J.; Cordiner, M. A.; Millar, T. J.; Markwick-Kemper, A. J.; Jewell, P. R. *Astrophys. J.* **2007**, *664*, L47.
- (30) Millar, T. J.; Walsh, C.; Cordiner, M. A.; Ni Chuimin, R.; Herbst, E. *Astrophys. J.* **2007**, *662*, L87.
- (31) Heger, M. L. *Lick Observatory bulletin* **1922**, *337*, 141.
- (32) Tuairisg, S. O.; Cami, J.; Foing, B. H.; Sonnentrucker, P.; Ehrenfreund, P. *Astron. Astrophys. Suppl. Ser.* **2000**, *142*, 225.
- (33) Herbig, G. H. *Annu. Rev. Astron. Astrophys.* **1995**, *33*, 19.
- (34) Douglas, A. E. *Nature* **1977**, *269*, 130.
- (35) Fulara, J.; Lessen, D.; Freivogel, P.; Maier, J. P. *Nature* **1993**, *366*, 439.
- (36) Ehrenfreund, P.; Foing, B. H. *Astron. Astrophys.* **1996**, *307*, L25.
- (37) Foing, B. H.; Ehrenfreund, P. *Astron. Astrophys.* **1997**, *317*, L59.
- (38) Vanderzwet, G. P.; Allamandola, L. J. *Astron. Astrophys.* **1985**, *146*, 76.
- (39) Le Page, V.; Snow, T. P.; Bierbaum, V. M. *Astrophys. J.* **2003**, *584*, 316.

- (40) Salama, F.; Bakes, E. L. O.; Allamandola, L. J.; Tielens, A. G. G. M. *Astrophys. J.* **1996**, *458*, 621.
- (41) Brechignac, P.; Pino, T. *Astron. Astrophys.* **1999**, *343*, L49.
- (42) The NASA Imagine Team. In *What is your Cosmic Connection to the Elements*; 1997: <http://imagine.gsfc.nasa.gov/docs/teachers/elements/imagine/contents.html>, 09/2008.
- (43) Shull, J. M. *Phys. Scr.* **1993**, *T47*, 165.
- (44) Van Steenberg, M. E.; Shull, J. M. *Astrophys. J.* **1988**, *330*, 942.
- (45) Klotz, A.; Marty, P.; Boissel, P.; Serra, G.; Chaudret, B.; Daudey, J. P. *Astron. Astrophys.* **1995**, *304*, 520.
- (46) Marty, P.; deParseval, P.; Klotz, A.; Serra, G.; Boissel, P. *Astron. Astrophys.* **1996**, *316*, 270.
- (47) Whittle, E.; Dows, D. A.; Pimentel, G. C. *J. Chem. Phys.* **1954**, *22*, 1943.
- (48) Fowles, G. R. *Introduction to Modern Optics*; Dover Publications Inc.: New York, 1975.
- (49) Snow, T. P.; Rachford, B. L.; Figoski, L. *Astrophys. J.* **2002**, *573*, 662.
- (50) Escalante-Ramirez, V. *Re: Space matter, energy, anti-matter* 2003; <http://www.madsci.org/posts/archives/Mar2003/1046619096.As.r.html>, 11/2008.
- (51) De Boer, K. S.; Lamers, H. J. G. L. M. *Astron. Astrophys.* **1978**, *69*, 327.
- (52) Savage, B. D.; Bohlin, R. C. *Astrophys. J.* **1979**, *229*, 136.
- (53) Jenkins, E. B.; Savage, B. D.; Spitzer, L. *Astrophys. J.* **1986**, *301*, 355.
- (54) Serra, G.; Chaudret, B.; Saillard, Y.; Lebeuze, A.; Rabaa, H.; Ristorcelli, I.; Klotz, A. *Astron. Astrophys.* **1992**, *260*, 489.
- (55) Chaudret, B.; Lebeuze, A.; Rabaa, H.; Saillard, J. Y.; Serra, G. *New J. Chem.* **1991**, *15*, 791.
- (56) Timms, P. L. *J. Chem. Soc. D-Chem. Comm.* **1969**, 1033.
- (57) Efner, H. F.; Tevault, D. E.; Fox, W. B.; Smardzewski, R. R. *J. Organomet. Chem.* **1978**, *146*, 45.
- (58) Aleksanyan, V. T.; Kurtikyan, T. S. *Koord. Khim.* **1977**, *3*, 1548.

- (59) Shobert, A. L.; Hisatsune, I. C.; Skell, P. S. *Spectrochim. Acta, Part A* **1984**, *40*, 609.
- (60) Morand, P. D.; Francis, C. G. *Organometallics* **1985**, *4*, 1653.
- (61) Parker, S. F.; Peden, C. H. F. *J. Organomet. Chem.* **1984**, *272*, 411.
- (62) Ball, D. W.; Kafafi, Z. H.; Hauge, R. H.; Margrave, J. L. *J. Am. Chem. Soc.* **1986**, *108*, 6621.
- (63) Boissel, P. *Astron. Astrophys.* **1994**, *285*, L33.
- (64) Marty, P.; deParseval, P.; Klotz, A.; Chaudret, B.; Serra, G.; Boissel, P. *Chem. Phys. Lett.* **1996**, *256*, 669.
- (65) Caraiman, D.; Bohme, D. K. *Int. J. Mass spectrom.* **2003**, *223*, 411.
- (66) Buchanan, J. W.; Reddic, J. E.; Grieves, G. A.; Duncan, M. A. *J. Phys. Chem. A* **1998**, *102*, 6390.
- (67) Buchanan, J. W.; Grieves, G. A.; Flynn, N. D.; Duncan, M. A. *Int. J. Mass spectrom.* **1999**, *187*, 617.
- (68) Buchanan, J. W.; Grieves, G. A.; Reddic, J. E.; Duncan, M. A. *Int. J. Mass spectrom.* **1999**, *183*, 323.
- (69) Foster, N. R.; Grieves, G. A.; Buchanan, J. W.; Flynn, N. D.; Duncan, M. A. *J. Phys. Chem. A* **2000**, *104*, 11055.
- (70) Jaeger, T. D.; Duncan, M. A. *J. Phys. Chem. A* **2004**, *108*, 11296.
- (71) Elustondo, E.; Dalibart, M.; Deroult, J.; Mascetti, J. *Phys. Chem. Earth Part C* **1999**, *24*, 583.
- (72) Szczepanski, J.; Wang, H. Y.; Vala, M.; Tielens, A. G. G. M.; Eyler, J. R.; Oomens, J. *Astrophys. J.* **2006**, *646*, 666.

- (73) Frisch, M. J.; Trucks, G. W.; Schlegel, H. B.; Scuseria, G. E.; Robb, M. A.; Cheeseman, J. R.; Montgomery, J. J. A.; Vreven, T.; Kudin, K. N.; Burant, J. C.; Millam, J. M.; Iyengar, S. S.; Tomasi, J.; Barone, V.; Mennucci, B.; Cossi, M.; Scalmani, G.; Rega, N.; Petersson, G. A.; Nakatsuji, H.; Hada, M.; Ehara, M.; Toyota, K.; Fukuda, R.; Hasegawa, J.; Ishida, M.; Nakajima, T.; Honda, Y.; Kitao, O.; Nakai, H.; Klene, M.; Li, X.; Knox, J. E.; Hratchian, H. P.; Cross, J. B.; Bakken, V.; Adamo, C.; Jaramillo, J.; Gomperts, R.; Stratmann, R. E.; Yazyev, O.; Austin, A. J.; Cammi, R.; Pomelli, C.; Ochterski, J. W.; Ayala, P. Y.; Morokuma, K.; Voth, G. A.; Salvador, P.; Dannenberg, J. J.; Zakrzewski, V. G.; Dapprich, S.; Daniels, A. D.; Strain, M. C.; Farkas, O.; Malick, D. K.; Rabuck, A. D.; Raghavachari, K.; Foresman, J. B.; Ortiz, J. V.; Cui, Q.; Baboul, A. G.; Clifford, S.; Cioslowski, J.; Stefanov, B. B.; Liu, G.; Liashenko, A.; Piskorz, P.; Komaromi, I.; Martin, R. L.; Fox, D. J.; Keith, T.; Al-Laham, M. A.; Peng, C. Y.; Nanayakkara, A.; Challacombe, M.; Gill, P. M. W.; Johnson, B.; Chen, W.; Wong, M. W.; Gonzalez, C.; Pople, J. A. Gaussian 03; Revision B. 05 ed.; Gaussian, Inc.: Wallingford, CT, 2003.
- (74) Perdew, J. P.; Wang, Y. *Phys. Rev. B* **1992**, *45*, 13244.
- (75) Adamo, C.; Barone, V. *J. Chem. Phys.* **1998**, *108*, 664.
- (76) Oomens, J.; Moore, D. T.; von Helden, G.; Meijer, G.; Dunbar, R. C. *J. Am. Chem. Soc.* **2004**, *126*, 724.
- (77) Values taken from the NIST atomic spectra database.
<http://physics.nist.gov/PhysRefData/ASD/index.html>.
- (78) Brown, K. G.; Person, W. B. *Spectrochim. Acta, Part A* **1978**, *34*, 117.
- (79) Robbins, D. L.; Rittby, C. M. L.; Graham, W. R. M. *J. Chem. Phys.* **2001**, *114*, 3570.
- (80) Kinzer, R. E.; Rittby, C. M. L.; Graham, W. R. M. *J. Chem. Phys.* **2006**, *125*.
- (81) Bates, S. A.; Rhodes, J. A.; Rittby, C. M. L.; Graham, W. R. M. *J. Chem. Phys.* **2007**, *127*.
- (82) Kinzer, R. E.; Rittby, C. M. L.; Graham, W. R. M. *J. Chem. Phys.* **2008**, *128*.
- (83) Bates, S. A.; Rittby, C. M. L.; Graham, W. R. M. *J. Chem. Phys.* **2006**, *125*.
- (84) Datta, B. P.; Sant, V. L.; Raman, V. A.; Subbanna, C. S.; Jain, H. C. *Int. J. Mass Spectrom. Ion Processes* **1989**, *91*, 241.
- (85) Guo, B. C.; Kerns, K. P.; Castleman, A. W. *Science* **1992**, *255*, 1411.
- (86) Kosolapova, T. Y. *Carbide*; Plenum Press: New York, 1971.

- (87) Katskov, D. A.; Kruglikova, L. P.; L'Vov, B. V.; Polzik, L. K. *Zhurnal Prikladnoi Spektroskopii; J. Appl. Spectry. [USSR]* **1976**, *25*, 1459.
- (88) Yamada, Y.; Castleman, A. W. *Chem. Phys. Lett.* **1993**, *204*, 133.
- (89) Becke, A. D. *J. Chem. Phys.* **1993**, *98*, 5648.
- (90) Wiberg, K. B. *J. Comput. Chem.* **1999**, *20*, 1299.
- (91) Dunbar, R. C. *J. Phys. Chem. A* **2002**, *106*, 7328.
- (92) Wang, Y.; Szczepanski, J.; Vala, M. *Chem. Phys.* **2007**, *342*, 107.
- (93) Legge, F. S.; Nyberg, G. L.; Peel, J. B. *J. Phys. Chem. A* **2001**, *105*, 7905.
- (94) Wang, X. F.; Andrews, L. *Angew. Chem. Int. Ed.* **2003**, *42*, 5201.
- (95) Weltner, W., Jr.; Van Zee, R. J. *Chem. Rev.* **1989**, *89*, 1713.
- (96) Van Orden, A.; Saykally, R. J. *Chem. Rev.* **1998**, *98*, 2313.
- (97) Szczepanski, J.; Hodyss, R.; Vala, M. *J. Phys. Chem. A* **1998**, *102*, 8300.
- (98) Szczepanski, J.; Auerbach, E.; Vala, M. *J. Phys. Chem. A* **1997**, *101*, 9296.
- (99) Gutsev, G. L.; Andrews, L.; Bauschlicher, C. W. *Chem. Phys.* **2003**, *290*, 47.
- (100) Jacox, M. E.; Milligan, D. E. *Chem. Phys.* **1974**, *4*, 45.
- (101) Jiang, Q.; Rittby, C. M. L.; Graham, W. R. M. *J. Chem. Phys.* **1993**, *99*, 3194.
- (102) Andrews, L.; Kushto, G. P.; Zhou, M. F.; Willson, S. P.; Souter, P. F. *J. Chem. Phys.* **1999**, *110*, 4457.
- (103) Ding, X. D.; Wang, S. L.; Rittby, C. M. L.; Graham, W. R. M. *J. Chem. Phys.* **2000**, *112*, 5113.
- (104) Szczepanski, J.; Ekern, S.; Vala, M. *J. Phys. Chem.* **1995**, *99*, 8002.
- (105) Grotjahn, D. B.; Brewster, M. A.; Ziurys, L. M. *J. Am. Chem. Soc.* **2002**, *124*, 5895.
- (106) Szczepanski, J.; Vala, M. *Eur. Phys. J. - Special Topics* **2007**, *144*, 27.
- (107) Fueno, H.; Taniguchi, Y. *Chem. Phys. Lett.* **1999**, *312*, 65.
- (108) Herbst, E. *Space Sci. Rev.* **2002**, *96*, 1.
- (109) Lapinski, L.; Vala, M. *Chem. Phys. Lett.* **1999**, *300*, 195.

- (110) Liu, P.; Rodriguez, J. A.; Muckerman, J. T. *J. Phys. Chem. B* **2004**, *108*, 15662.
- (111) Liu, P.; Rodriguez, J. A.; Muckerman, J. T. *J. Phys. Chem. B* **2004**, *108*, 18796.
- (112) Cartier, S. F.; May, B. D.; Castleman, A. W. *J. Chem. Phys.* **1994**, *100*, 5384.
- (113) Cartier, S. F.; May, B. D.; Castleman, A. W. *J. Am. Chem. Soc.* **1994**, *116*, 5295.
- (114) Leskiw, B. D.; Castleman, A. W. *Comptes Rendus Physique* **2002**, *3*, 251.
- (115) Pilgrim, J. S.; Duncan, M. A. *J. Am. Chem. Soc.* **1993**, *115*, 9724.
- (116) Tono, K.; Terasaki, A.; Ohta, T.; Kondow, T. *Chem. Phys. Lett.* **2002**, *351*, 135.
- (117) Knappenberger, K. L.; Jones, C. E.; Sobhy, M. A.; Iordanov, I.; Sofo, J.; Castleman, A. W. *J. Phys. Chem. A* **2006**, *110*, 12814.
- (118) Knappenberger, K. L.; Clayborne, P. A.; Reveles, J. U.; Sobhy, M. A.; Jones, C. E.; Gupta, U. U.; Khanna, S. N.; Iordanov, I.; Sofo, J.; Castleman, A. W. *Acs Nano* **2007**, *1*, 319.
- (119) Wang, L. S.; Li, X. *J. Chem. Phys.* **2000**, *112*, 3602.
- (120) Zhai, H. J.; Liu, S. R.; Li, X.; Wang, L. S. *J. Chem. Phys.* **2001**, *115*, 5170.
- (121) Fan, J. W.; Lou, L.; Wang, L. S. *J. Chem. Phys.* **1995**, *102*, 2701.
- (122) Wang, X. B.; Ding, C. F.; Wang, L. S. *J. Phys. Chem. A* **1997**, *101*, 7699.
- (123) Kohno, M.; Suzuki, S.; Shiromaru, H.; Kobayashi, K.; Nagase, S.; Achiba, Y.; Kietzmann, H.; Kessler, B.; Gantefoer, G.; Eberhardt, W. *J. Electron. Spectrosc. Relat. Phenom.* **2000**, *112*, 163.
- (124) Bates, S. A.; Rittby, C. M. L.; Graham, W. R. M. *J. Chem. Phys.* **2008**, *128*, 234301.
- (125) Cataldo, F. *J. Raman Spectrosc.* **2008**, *39*, 169.
- (126) Sakurai, H.; Castleman, A. W. *J. Phys. Chem. A* **1998**, *102*, 10486.
- (127) Wang, L. S.; Li, S.; Wu, H. B. *J. Phys. Chem.* **1996**, *100*, 19211.
- (128) Szczepanski, J.; Wang, Y.; Vala, M. *J. Phys. Chem. A* **2008**, *112*, 4778.
- (129) Vogel, A. I. *Practical Organic Chemistry*, 3rd ed.; Longmans: London, 1967.
- (130) Bahr, G.; Burba, P. In *Methoden der Organischen Chemie*; Houben-Weyl Thieme-Verlag: Stuttgart, Germany, 1970; Vol. 13, Part I; pp 767.

- (131) Andrae, D.; Haussermann, U.; Dolg, M.; Stoll, H.; Preuss, H. *Theor. Chim. Acta* **1990**, *77*, 123.
- (132) Chan, W. T.; Fournier, R. *Chem. Phys. Lett.* **1999**, *315*, 257.
- (133) Hamilton, I. P. *Chem. Phys. Lett.* **2004**, *390*, 517.
- (134) Kranze, R. H.; Graham, W. R. M. *J. Chem. Phys.* **1993**, *98*, 71.
- (135) Liang, B. Y.; Andrews, L. *J. Phys. Chem. A* **2000**, *104*, 9156.
- (136) Jiang, L.; Xu, Q. *J. Phys. Chem. A* **2005**, *109*, 1026.
- (137) Zhai, H. J.; Kiran, B.; Dai, B.; Li, J.; Wang, L. S. *J. Am. Chem. Soc.* **2005**, *127*, 12098.
- (138) Fielicke, A.; von Helden, G.; Meijer, G.; Pedersen, D. B.; Simard, B.; Rayner, D. M. *J. Am. Chem. Soc.* **2005**, *127*, 8416.
- (139) Fielicke, A.; von Helden, G.; Meijer, G.; Simard, B.; Rayner, D. M. *J. Phys. Chem. B* **2005**, *109*, 23935.
- (140) Velasquez, J.; Njegic, B.; Gordon, M. S.; Duncan, M. A. *J. Phys. Chem. A* **2008**, *112*, 1907.
- (141) Kong, Q.; Zeng, A.; Chen, M.; Xu, Q.; Zhou, M. *J. Phys. Chem. A* **2004**, *108*, 1531.
- (142) Wang, X.; Andrews, L. *J. Phys. Chem. A* **2002**, *106*, 3744.
- (143) Schroder, D.; Brown, R.; Schwerdtfeger, P.; Wang, X. B.; Yang, X.; Wang, L. S.; Schwarz, H. *Angew. Chem. Int. Ed.* **2003**, *42*, 311.
- (144) Jiang, L.; Kohyama, M.; Haruta, M.; Xu, Q. *J. Phys. Chem. A* **2008**, *112*, 13495.
- (145) Barysz, M.; Pyykko, P. *Chem. Phys. Lett.* **1998**, *285*, 398.
- (146) Pyykko, P.; Patzschke, M.; Suurpere, J. *Chem. Phys. Lett.* **2003**, *381*, 45.
- (147) Puzzarini, C.; Peterson, K. A. *Chem. Phys.* **2005**, *311*, 177.
- (148) Ticknor, B. W.; Bandyopadhyay, B.; Duncan, M. A. *J. Phys. Chem. A* **2008**, *112*, 12355.
- (149) Wang, Y.; Szczepanski, J.; Vala, M. *J. Phys. Chem. A* **2008**, *112*, 11088.
- (150) Hay, P. J.; Wadt, W. R. *J. Chem. Phys.* **1985**, *82*, 270.
- (151) Wadt, W. R.; Hay, P. J. *J. Chem. Phys.* **1985**, *82*, 284.

(152) Hay, P. J.; Wadt, W. R. *J. Chem. Phys.* **1985**, 82, 299.

BIOGRAPHICAL SKETCH

Yun Wang was born in Shanghai, China, in July 1981. She grew up in Shanghai and graduated from Shixi High School in June 1999. Yun continued her education at Fudan University, majoring in chemistry, and received her Bachelor of Science degree in June 2003.

In August 2004, Yun enrolled in the Department of Chemistry at the University of Florida to pursue a Doctor of Philosophy degree in physical chemistry. From then on, she worked in Dr. Martin Vala's research group, and dedicated herself to vibrational spectroscopy of astrophysical species.